

Trabajo Fin de Grado Grado en Ingeniería Aeroespacial

Analysis of perturbation effects in precise prediction of Low Earth Orbits

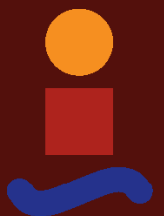
Autor: Antonio Malaver Jambrina

Tutores: Rafael Vázquez Valenzuela

José Manuel Montilla García

**Dpto. Ingeniería Aeroespacial y Mecánica de Fluidos
Escuela Técnica Superior de Ingeniería
Universidad de Sevilla**

Sevilla, 2022



Trabajo Fin de Grado
Grado en Ingeniería Aeroespacial

Analysis of perturbation effects in precise prediction of Low Earth Orbits

Autor:

Antonio Malaver Jambrina

Tutores:

Rafael Vázquez Valenzuela

Profesor Titular

José Manuel Montilla García

Dpto. Ingeniería Aeroespacial y Mecánica de Fluidos
Escuela Técnica Superior de Ingeniería
Universidad de Sevilla

Sevilla, 2022

Trabajo Fin de Grado: Analysis of perturbation effects in precise prediction of Low Earth Orbits

Autor: Antonio Malaver Jambrina
Tutores: Rafael Vázquez Valenzuela
José Manuel Montilla García

El tribunal nombrado para juzgar el trabajo arriba indicado, compuesto por los siguientes profesores:

Presidente:

Vocal/es:

Secretario:

acuerdan otorgarle la calificación de:

El Secretario del Tribunal

Fecha:

Agradecimientos

La educación es el arma más poderosa que podemos usar para cambiar el mundo. Todos los días podemos aprender algo acerca del maravilloso mundo que nos rodea, en el cual he tenido la suerte de compartir mi vida con personas maravillosas a las cuales les quiero dar las gracias por todo lo que han hecho y hacen por mí día tras día.

Debo comenzar dándole las gracias a mis tutores, Rafael y José Manuel, por haber confiado desde el primer momento en mí y haberme dado esta gran oportunidad. Gracias por todas sus enseñanzas, por tenderme siempre la mano, por su ayuda durante el desarrollo de este proyecto y por recibirme siempre con una sonrisa.

A todos los profesores de esta maravillosa escuela, ya que entre todos han hecho de mí una mejor persona.

A mis compañeros y amigos de carrera. Juntos hemos conseguido sacar una mejor versión los unos de los otros, siempre animándonos a superar los obstáculos y empujándonos a mejorar cada día.

A mis amigos de toda la vida: Aida, Alberto, Alejandro, Álvaro, Amelia, Andrés, Ayelen, Jose María, Cristina, Gabriel, Juan Miguel y Santiago. Esos amigos que no fallan y que están ahí pase lo que pase. Gracias por todos los momentos vividos y por los que nos quedan por vivir. No sabeis lo importantes que sois para mí cada uno de vosotros.

A Irene, por todo el cariño y amor que me ha regalado durante estos años. Por la ayuda brindada en este sendero que hemos recorrido juntos y por todo lo que me has enseñado.

A mis primos y tíos, y en especial a mi Nina. Gracias por esforzarte cada día, por luchar mañana tras mañana para superar cualquier cosa que se pusiera en tu camino y por hacernos mejores personas.

Acordarme también de mis abuelas, Dolores y Manoli, que han podido ver como su nieto cumplía su sueño. Teneros a mi lado es un regalo que jamás podré apreciar lo suficiente.

A mi hermana Irene, por ser la alegría de mis días. Vas a llegar muy lejos, muchísimo más de lo que yo jamás podría soñar. Te quiero con toda mi alma.

Y finalmente, a mis padres, Antonio y Laura. Ellos son el principal motivo por el cual he llegado hasta donde estoy hoy. Solo unos pocos tenemos la suerte de tener unos padres como vosotros. Gracias por desviviros por vuestra familia y por anteponer los intereses de vuestros hijos a cualquier cosa. Jamás podré agradecerlos lo suficiente lo que habeis hecho por mí. Sois mi buque insignia y mis mañanitas del rey David.

Antonio Malaver Jambrina

Sevilla, 2022

Resumen global

Título: Análisis de los efectos de las perturbaciones en predicciones precisas en órbitas terrestres bajas.

Resumen: Tras analizar el problema de los dos cuerpos y revisar en profundidad las distintas perturbaciones a las que están sometidos los satélites, se explica la herramienta Orekit. Esta permite el cálculo de la órbita de los satélites afectados bajo diferentes tipos de perturbaciones.

Mediante Orekit se realiza un extenso análisis abordando las fuerzas más importantes que pueden afectar a satélites en LEO y GEO, para posteriormente pasar a analizar datos reales de satélites proporcionados por la agencia espacial europea en formato OEM.

Con estos datos se diseña un propagador que permita predecir con alta precisión la posición y velocidad de los satélites Sentinel-1A/B y Sentinel-2A/B y finalmente se extraen las conclusiones y se proponen futuras mejoras.

Palabras clave: Orekit, Predicción precisa de órbitas, Perturbaciones, Sentinel-1, Sentinel-2, Orbit Ephemeris Message OEM, Propagador.

Conclusiones: La combinación del modelo atmosférico Harris-Priester y las mareas mejora para propagaciones con duración menor de 24 horas y mayores de 39 horas las predicciones hechas por el modelo atmosférico más preciso NRLMSISE-00 sin considerar mareas. La combinación de los modelos más precisos para diferentes tipos de perturbaciones no siempre da como resultado el propagador más preciso, por lo que es necesario analizar qué tipo de modelos casan mejor entre sí para predecir la órbita de los satélites que se están analizando.

Abstract

The objective of this project is to develop an accurate, efficient propagator for Low Earth Orbit satellites designed and launched by the European Space Agency. Predicting where an object will be after several hours since the last time we measured its position is crucial in order to prevent accidents with other satellites during the time lapse we can not track the satellite's position and direction of movement. This need resulted in this project, in which the analysis of different kind of perturbations is made in order to decide which ones we should take into account and which ones are disposables.

Perturbations can be understood as the forces that disturb the classical Keplerian orbit of orbiting objects. The four main forces that must be taken into account are the non-spherical body's gravity, the third-body perturbations, the solar-radiation pressure and the atmospheric drag, being the last one the most important in LEO. Other kind of perturbations, such as tides or the precession of Earth's axis, are discussed throughout this project.

To perform the computations to predict the position and velocity of the satellites under study, the tool Orekit is used. This low-level space dynamic library written in Java can be integrated into Matlab, and offers a wide scope when studying space dynamics. This tool is the base of this project, and it is used to analyse the effect that different kind of perturbations have in LEO and GEO satellites. Since it was released as an open source in 2008, its popularity grew exponentially due to the precision that this tool allows. In this project its library is presented, as well as the different uses that this tool can have.

The data of the satellites is provided by ESA in the form of Orbit Ephemeris Messages, which are used to specify the position and velocity of a single object at one or multiple epochs. The OEMs format is presented in this project, along with several examples of different versions of the OEMs.

In order to design a precise propagator, a comparison between several perturbation models offered by Orekit's library is carried out. These models are compared with one another to decide which one behaves better when propagating the orbit of the satellites studied.

The propagator designed to propagate the orbits with high precision is presented, along with the results obtained for the Sentinel-1 and Sentinel-2 classes.

Keywords: Orekit, Precise orbit prediction, Perturbations, Sentinel-1, Sentinel-2, Orbit Ephemeris Message OEM, Propagator.

Contents

<i>Resumen global</i>	III
<i>Abstract</i>	V
1 Introduction	1
1.1 Motivation	1
1.1.1 The urge to predict the future	1
1.1.2 Sentinel project	2
Sentinel-1 [12]	2
Sentinel-2 [13]	3
1.2 Objectives of this project	4
1.3 Structure	4
2 Introduction to Orbital Mechanics	7
2.1 The two-body problem	7
2.1.1 Motion equation	7
2.1.2 Orbital elements	10
2.2 Perturbations	11
2.2.1 Non-spherical body's gravity	12
2.2.2 Atmospheric drag	14
2.2.3 Third-Body perturbations	16
2.2.4 Solar-Radiation pressure	17
2.2.5 Other effects	18
3 Introduction to Orekit	21
3.1 About Orekit	21
3.2 Orekit features	21
3.2.1 Time	21
3.2.2 Frames	22
3.2.3 Forces	26
3.2.4 Attitudes	27
3.2.5 Orbits	27
3.2.6 Two-Line Elements	28
3.2.7 Bodies	28
3.2.8 Propagation	28
3.3 Introductory examples	31
3.3.1 Geostationary satellite affected by the Sun and the Moon	31

3.3.2	Low Earth Orbit satellite affected by the Sun and the Moon	34
3.3.3	GEO satellite affected by J_2 perturbation	39
3.3.4	Low Earth Orbit satellite affected by J_2 perturbation	41
3.3.5	Low Earth Orbit satellite affected by atmospheric drag	46
3.3.6	GEO satellite affected by solar radiation pressure	51
3.3.7	LEO satellite affected by solar radiation pressure	53
4	Precise analysis and characterisation of real satellites in Low Earth Orbits	57
4.1	Orbit ephemeris message (OEM)	57
4.1.1	OEM Header	58
	OEM Metadata	58
4.1.2	OEM Data: Ephemeris data lines	59
4.1.3	OEM Data: Covariance matrix lines	59
4.1.4	OEM Examples	59
4.2	Perturbations model verification and validation	62
4.2.1	Optimisation process	63
4.2.2	Non-spherical body's gravity	64
4.2.3	Third-Body perturbations	65
4.2.4	Atmospheric drag	66
4.2.5	Solar-Radiation pressure	68
4.2.6	Tides	68
4.2.7	Final propagation model	71
4.3	Precise prediction of LEO satellites	71
4.3.1	Sentinel-1	71
	Sentinel-1A	72
	Sentinel-1B	73
4.3.2	Sentinel-2	74
	Sentinel-2A	74
	Sentinel-2B	75
4.3.3	Results discussion	75
5	Conclusions and future work	77
5.1	Conclusions	77
5.2	Future work	77
	<i>List of Figures</i>	79
	<i>List of Tables</i>	81
	<i>Bibliography</i>	83

1 Introduction

1.1 Motivation

1.1.1 The urge to predict the future

Humankind has always sought ways to predict the future, both near and far. The desire to know what will happen in a day, a month, a year or a century is innate to human beings. Will Bitcoin make me rich next month? When will the next pandemic occur? What external factors will influence my industries? Where will I be in thirty years?

The desire to know the future is rooted in the human desire for control. Knowing what is going to happen allows us to act accordingly, to be prepared. The uncertainty of what will be is what scares most people. Throughout history we have devised many tools to try to predict the future and one of the most widespread today is the horoscope. This astrological diagram represents the position of the Sun, Moon, planets, astrological aspects and sensible angles at the time of an event, such as the time of a person's birth. Many newspapers and magazines have prediction columns, and the number of websites that "predict your future" based on the position of the planets when you were born has grown exponentially. It turns out that there are no scientific studies that have proven the accuracy of horoscopes, and the methods used to make interpretations are pseudo scientific. In the modern scientific framework there is no known interaction that could be responsible for the transmission of the supposed influence between a person and the position of the stars in the sky at the time of birth. In all tests conducted, maintaining strict methods of inclusion of a control group and proper blinding between experimenters and subjects, horoscopes have shown no effect beyond pure chance. Furthermore, some psychological tests have shown that it is possible to construct personality descriptions and predictions generic enough to simultaneously satisfy most members of a large audience, known as the Barnum effect [10].

It seems impossible to predict whether you will get married in two years' time based on your birthday, but it is possible to predict the future of a satellite, for example. Since the 16th century, thanks to Kepler, we know that objects move in space in conical orbits. However, these orbits are not perfect. Due to the effect of external forces, perfect conical orbits degenerate into different kinds of shapes. Looking into the future is, in a sense, creating a model that accurately predicts what will happen. Imagine you have a recipe book that tells you what kind of dishes you will get if you combine certain kinds of ingredients. A perturbation model is our recipe book. It is able to predict the position and velocity of a satellite at any desired time just by knowing the initial conditions surrounding the satellite and the forces affecting it. And this is the goal of this project, to design a propagator that can accurately predict the position of the satellites under study.

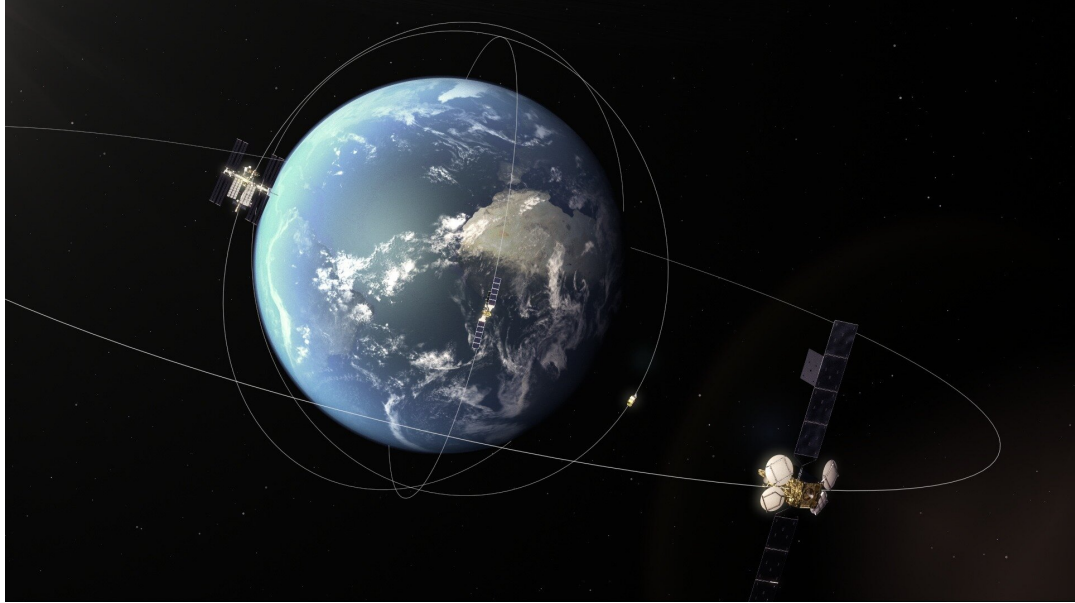


Figure 1.1 Geocentric satellites.

1.1.2 Sentinel project

Recently, the European Space Agency ESA developed a series of next-generation observation missions, which was called the Sentinel programme. The main object of these satellites is to replace the older Earth observation missions which have retired, such as the ERS and the Envisat missions. Each of the Sentinel missions focuses on a different aspect of Earth observation: atmospheric, land and oceanic monitoring.

Sentinel-1 [12]

The Sentinel-1 mission is the European Radar Observatory for the Copernicus joint initiative of the European Commission (EC) and the European Space Agency (ESA). Copernicus is a European initiative for the implementation of information services dealing with environment and security. It is based on observation data received from Earth Observation satellites and ground-based information.

The Sentinel-1 mission includes C-band imaging operating in four exclusive imaging modes with different resolution (down to 5 m) and coverage (up to 400 km). It provides dual polarisation capability, very short revisit times and rapid product delivery. For each observation, precise measurements of spacecraft position and attitude are available.

Synthetic Aperture Radar (SAR) has the advantage of operating at wavelengths not impeded by cloud cover or a lack of illumination and can acquire data over a site during day or night time under all weather conditions. Sentinel-1, with its C-SAR instrument, can offer reliable, repeated wide area monitoring.

The mission is composed of a constellation of two satellites, Sentinel-1A and Sentinel-1B, sharing the same orbital plane.

Sentinel-1 is designed to work in a pre-programmed, conflict-free operation mode, imaging all global landmasses, coastal zones and shipping routes at high resolution and covering the global ocean with vignettes. This ensures the reliability of service required by operational services and a consistent long term data archive built for applications based on long time series.



Figure 1.2 Sentinel-1 [12].

Sentinel-2 [13]

Sentinel-2 is a European wide-swath, high-resolution, multi-spectral imaging mission. The full mission specification of the twin satellites flying in the same orbit but phased at 180° , is designed to give a high revisit frequency of 5 days at the Equator.

Sentinel-2 carries an optical instrument payload that samples 13 spectral bands: four bands at 10 m, six bands at 20 m and three bands at 60 m spatial resolution. The orbital swath width is 290 km.

The Copernicus Sentinel-2 mission comprises a constellation of two polar-orbiting satellites placed in the same sun-synchronous orbit, phased at 180° to each other. It aims at monitoring variability in land surface conditions, and its wide swath width (290 km) and high revisit time (10 days at the equator with one satellite, and 5 days with 2 satellites under cloud-free conditions which results in 2-3 days at mid-latitudes) will support monitoring of Earth's surface changes.

The twin satellites of Sentinel-2 provides continuity of SPOT and LANDSAT-type image data, contribute to ongoing multi spectral observations and benefit Copernicus services and applications such as land management, agriculture and forestry, disaster control, humanitarian relief operations, risk mapping and security concerns.

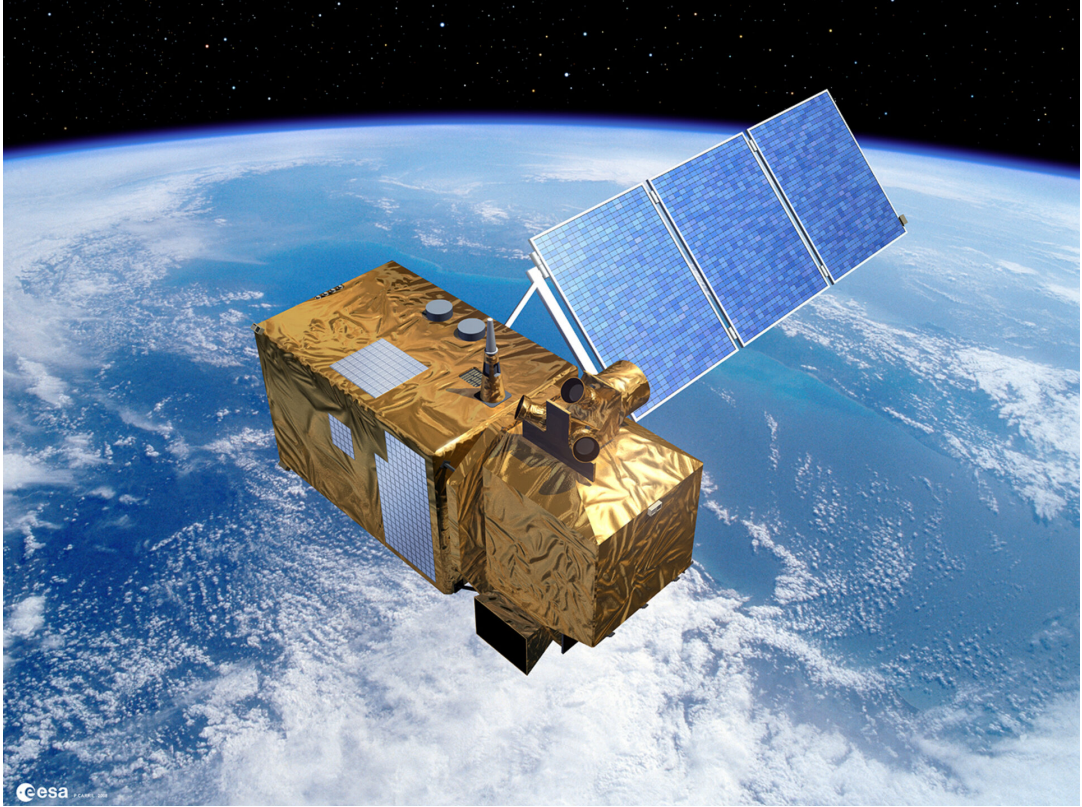


Figure 1.3 Sentinel-2 [13].

1.2 Objectives of this project

The main objective of this project is to present, develop and analyse a method to predict with high accuracy the position and velocity of the satellites under study given their initial orbit. In short, to predict the future. Likewise, it was done with the aim of improving the results obtained in [18]. The satellite orbit information is provided by ESA in the format of Orbit Ephemeris Messages (OEMs), and we use this information to compare the prediction made by the propagator and the real data. This project consists of using Orekit to analyse the best propagator design for our satellites. This tool, developed in Java, can be implemented in MATLAB to perform the necessary calculations.

For this purpose, an extensive analysis of different types of perturbations is presented, comparing the effects they have on the orbit of different satellites such as LEO and GEO. In addition, different types of perturbation models are studied in order to select the ones that best fit our satellites.

1.3 Structure

The structure of this project is defined as follows:

Chapter 2: An introduction to orbital mechanics is given, analysing the two-body problem and the perturbations that make the orbits differ from this simplified model. In addition, the magnitude of the four main perturbations is analysed in depth to clarify their importance in the analysis of geocentric orbits.

Chapter 3: The tool used to perform the calculations, Orekit, is presented. A brief review of its libraries is made and an extensive analysis of the different perturbations described in chapter 2 for LEO and GEO satellites is carried out.

Chapter 4: The format of the orbit ephemeris messages is described. A validation and verification of the designed perturbation model is also performed, concluding with the results obtained for the Sentinel-1 and Sentinel-2 satellites.

Chapter 5: Conclusions are drawn from the project and future improvements are proposed.

2 Introduction to Orbital Mechanics

In this chapter, the physical and mathematical concepts related to orbital mechanics and the theory of perturbations are presented.

2.1 The two-body problem

The two-body problem serves as an introduction to the real motion of heavenly bodies, affected by the gravitational forces exerted by all massive bodies in the universe, solar radiation pressure, electromagnetic force, atmospheric drag, etc. These forces are ignored in the analysis of the two-body problem.

2.1.1 Motion equation

First of all, two hypotheses are proposed to study the movement of two massive bodies in space attracted by the gravitational force:

- The system is isolated from the rest of the universe. The gravitational force is the only force that affects the two bodies.
- The mass of the two bodies can be considered punctual and located at their respective mass centres.

The last hypothesis can be substituted with Newton's shell theorem [5], which is equivalent:
A spherically symmetric body affects external objects gravitationally as though all of its mass were concentrated at a point at its centre.

The gravitational force wielded on each mass is given by Newton's gravitational law:

$$F = \frac{G \cdot m_1 \cdot m_2}{r^2}, \quad (2.1)$$

where G is the gravitational constant, m_1 and m_2 are the masses of the two bodies and r is the distance between the bodies.

The gravitational force represented in Figure 2.1 in vector form is:

$$\vec{F}_1 = \frac{G \cdot m_1 \cdot m_2}{r^2} \cdot \frac{\vec{r}}{r}, \quad (2.2)$$

$$\vec{F}_2 = -\frac{G \cdot m_1 \cdot m_2}{r^2} \cdot \frac{\vec{r}}{r}, \quad (2.3)$$

where $\vec{r} = \vec{R}_2 - \vec{R}_1$ and $\frac{\vec{r}}{r}$ is the unit vector. It is worth pointing out that \vec{R}_1 and \vec{R}_2 are defined with respect to an inertial frame.

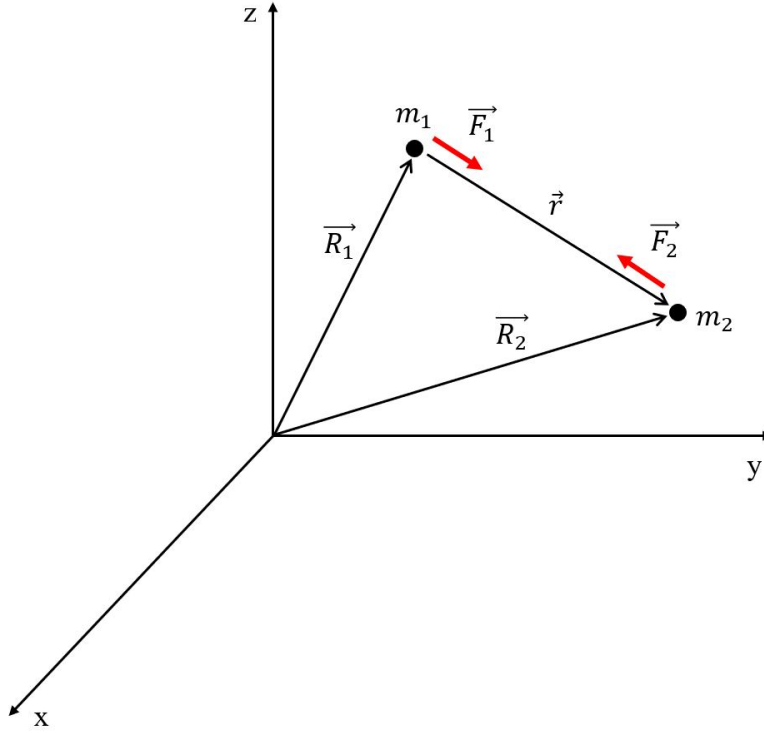


Figure 2.1 Gravitational force between two isolated masses.

Introducing Eq. (2.2) and Eq. (2.3) into Newton's second law, we get

$$\begin{aligned}\ddot{\vec{R}}_1 &= \frac{G \cdot m_2}{r^2} \cdot \frac{\vec{r}}{r}, \\ \ddot{\vec{R}}_2 &= -\frac{G \cdot m_1}{r^2} \cdot \frac{\vec{r}}{r}.\end{aligned}\tag{2.4}$$

The equations in system (2.4) involve twelve unknowns and describe the movement of the two bodies in the inertial frame. To solve the problem, let us define the position of the centre of mass of the two-body system \vec{R}_{CM} :

$$\vec{R}_{CM} = \frac{m_1 \cdot \vec{R}_1 + m_2 \cdot \vec{R}_2}{m_1 + m_2}.\tag{2.5}$$

Differentiating Eq. (2.5) two times with respect to time shows that the mass centre of the system describes an uniform rectilinear motion:

$$\ddot{\vec{R}}_{CM} = \vec{0} \rightarrow \vec{R}_{CM} = \vec{V}_{CM}(0) \cdot t + \vec{R}_{CM}(0).\tag{2.6}$$

Accordingly, moving the origin of the reference frame to the mass centre results in a new inertial reference frame (Figure 2.2), where the position of the two bodies is given by

$$\vec{r}_1 = \vec{R}_1 - \vec{R}_{CM} = \frac{m_2}{m_1 + m_2}(\vec{R}_1 - \vec{R}_2) = -\frac{m_2}{m_1 + m_2}\vec{r},\tag{2.7}$$

$$\vec{r}_2 = \vec{R}_2 - \vec{R}_{CM} = \frac{m_1}{m_1 + m_2}(\vec{R}_2 - \vec{R}_1) = \frac{m_1}{m_1 + m_2}\vec{r}.\tag{2.8}$$

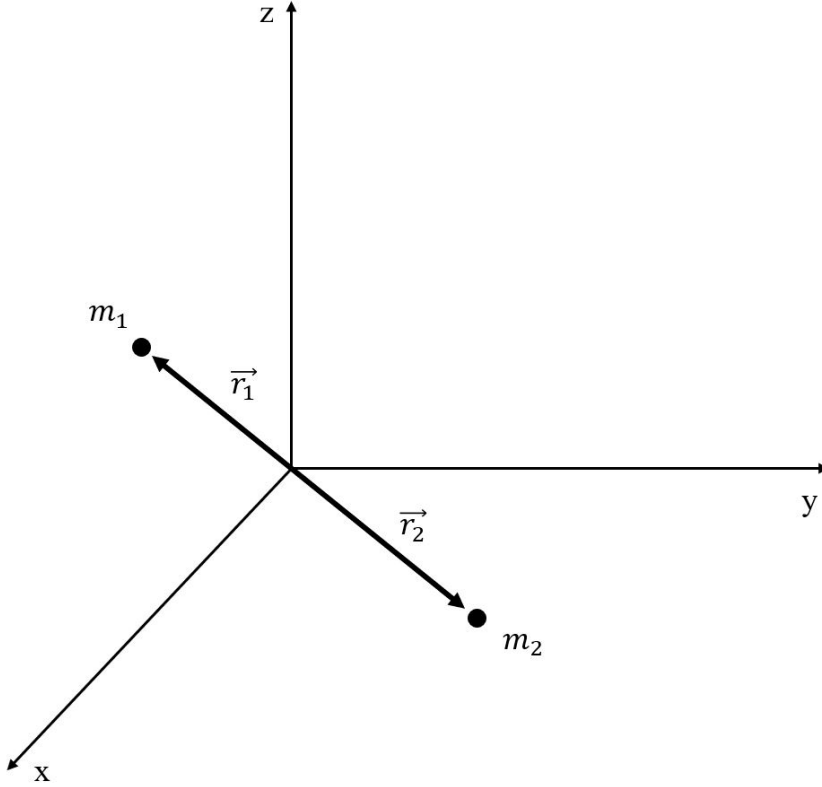


Figure 2.2 Mass-centre reference frame.

Finally, differentiating \vec{r} two times with respect to time results in

$$\ddot{\vec{r}} = \ddot{\vec{R}}_2 - \ddot{\vec{R}}_1 = -G(m_1 + m_2) \frac{\vec{r}}{r^3} = -\mu \frac{\vec{r}}{r^3}, \quad (2.9)$$

where $\mu = G(m_1 + m_2)$ is the standard gravitational parameter of the two masses combined. Note that if $m_1 \gg m_2$, the two-body problem can be approximated by the one-body problem, being $\mu \simeq \mu_1 = Gm_1$, $\vec{r}_1 \simeq \vec{0}$ and $\vec{r}_2 \simeq \vec{r}$, resulting in the following:

$$\ddot{\vec{r}} \simeq -\mu \frac{\vec{r}}{r^3}. \quad (2.10)$$

Performing the appropriate operations [9], the equation that describes the movement of a body around another more massive object and, hence, the solution to Eq. (2.10), is

$$r(\theta) = \frac{p}{1 + e \cos(\theta)}, \quad (2.11)$$

where:

- e is the eccentricity, which is the module of Laplace's vector or eccentricity vector \vec{e} , that points towards the conic periapsis, the point of minimal distance between the two bodies. The different cases of conics are determined by this parameter:
 - If $e = 0$, the conic is a circumference.
 - If $e \in (0, 1)$, the conic is an ellipse.
 - If $e = 1$, the conic is a parabola.
 - If $e > 1$, the conic is a hyperbola.

- $p = \frac{h^2}{\mu} \geq 0$ is the conic parameter, with $h = |\vec{h}|$ being the specific angular momentum. The situation $p = 0$ corresponds to degenerate conics.
- θ is the true anomaly, defined as the counterclockwise angle between \vec{r} and \vec{e} .

2.1.2 Orbital elements

To define an orbit in the 3 dimensional space we need 6 parameters called *orbital elements*, a plane of reference, which depends on the reference frame used, and a reference point. In orbits around planets, the plane of reference is the equator of the planet and in heliocentric orbits the reference plane is the ecliptic. The intersection between the plane of reference and the orbit plane determines the line of nodes, which is crossed by the orbit at two points: the ascending node Ω and the descending node Υ . Finally, the reference point used in celestial coordinate systems is the first point of Aries Υ , which is the direction from Earth to the Sun during the vernal equinox. The Keplerian orbital elements are as follows:

- $a = \frac{p}{1-e^2}$ is the semi-major axis of the conic. In the parabolic case ($e = 1$), p is used as long as a is not defined ($a \rightarrow \infty$).
- e is the eccentricity.
- θ is the true anomaly.
- Ω is the longitude of the ascending node Ω , the counterclockwise angle formed between the first point of Aries Υ and the ascending node Ω .
- ω is the argument of the periapsis, the angle in the direction of motion of the orbiting object between the node line from the ascending node Ω and the periapsis.
- i is the inclination, which is the counterclockwise angle between the reference plane and the orbital plane.

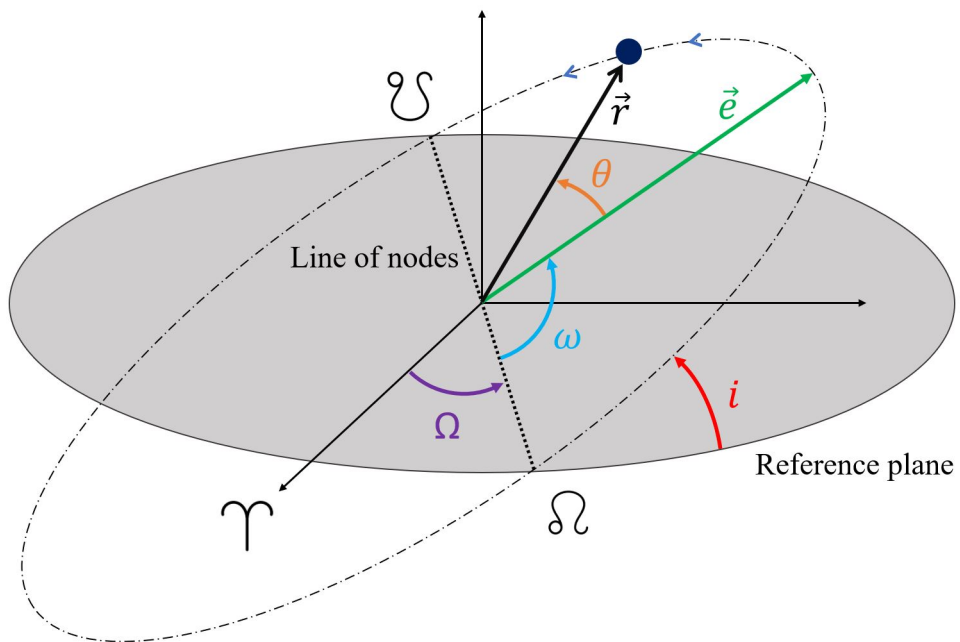


Figure 2.3 Keplerian orbital elements.

2.2 Perturbations

As mentioned, the two-body model is not realistic. With the hypotheses made in Section 2.1, we supposed an isolated system, yet there are other forces such as air drag, solar drag, other gravitational forces, etc. We also assumed punctual masses, but the Sun, planets and space vehicles are not perfect spheres. These discrepancies can be considered using perturbations that take into account the forces discarded in the two-body problem. These perturbations produce secular variations, constantly increasing or decreasing the value of an orbital element, and/or periodic variations, making them oscillate around a mean value. Their effects make the bodies describe non-Keplerian orbits.

The most important perturbations are classified into four main groups:

- **Atmospheric drag:** The force of the atmosphere acts in the opposite direction of the body's trajectory.
- **Non-spherical body's gravity:** On account of the non-spherical shape of the central body (Earth, the Sun, or the body considered), the point-mass model is inaccurate.
- **Third-Body perturbations:** The Sun, the Moon, and the other planets of the solar system exert a gravitational force that we did not consider in the two-body problem.
- **Solar-Radiation pressure:** The incidence of the solar light produces a force due to the pressure applied on the body.

Table 2.1 Forms of perturbations wielded on each orbital element. P stands for periodic and S for secular [25].

	Non-spherical body's gravity		Third body	Atmospheric drag	Solar radiation
	Zonal	Sect/Tes			
a	P	P	P	P+S	P
e	P	P	P	P+S	P
i	P	P	P	P+S	P
Ω	P+S	P	P+S	P	P+S
ω	P+S	P	P+S	P	P+S
θ	P+S	P	P+S	P	P+S

To handle these perturbations, two main models are employed:

- **General perturbations model:** This model studies the temporal evolution of the orbital elements. The non-Keplerian orbit is obtained by solving $\ddot{\vec{\alpha}} = \vec{F}(\vec{\alpha}, \vec{\gamma}_p)$, where $\vec{\alpha} = [a, e, i, \omega, \Omega, \theta]$ is the vector of orbital elements, $\vec{\gamma}_p$ is the perturbations' vector and \vec{F} are the equations that, along with $\ddot{\vec{\alpha}}$, constitute the system of equations that describe the trajectory of the orbiting object, which is called the planetary equations.
- **Special perturbations model:** The movement equations are directly used, avoiding the usage of orbital elements. There are two different approaches for this model:
 - **Encke's method:** Consists in a direct resolution of the movement equations, including as many bodies and forces as required. This method is the most used nowadays.
 - **Cowell's method:** In this method, a correction $\delta\vec{r}$ is solved over a reference solution of the two-body problem (2.10). If the correction grows, it is necessary to recompute the reference solution. Much less used nowadays.

In order to study the perturbations, the equation motion deduced in Eq. (2.10) can be modified to add as many perturbations as we desire in order to apply Encke's method. This is:

$$\ddot{\vec{r}} = \vec{\gamma}_K + \sum_{i=1}^N \vec{\gamma}_{P_i}, \quad (2.12)$$

where $\vec{\gamma}_K = -\mu \frac{\vec{r}}{r^3}$ is the acceleration due to the Keplerian force and $\vec{\gamma}_{P_i}$ are the accelerations due to each perturbations considered in the problem. This allows us to compare the magnitude of the different perturbations with respect to the Keplerian acceleration and discard the non-relevant ones.

$$\zeta(\vec{\gamma}_P, \vec{\gamma}_K) = \frac{|\vec{\gamma}_P|}{|\vec{\gamma}_K|}. \quad (2.13)$$

Therefore, we can interpret the second term in Eq. (2.12) as the accelerations deviations with respect to the original two-body problem. It is worth pointing out that from now on we refer to ζ as both the comparison of acceleration and the comparison of forces, as the mass of the satellite banishes in the equation.

In the following sections we compare the magnitude of the Keplerian acceleration and the perturbation acceleration of the four main perturbations mentioned exerted on Low Earth Orbit LEO ($< 7400 \text{ km}$) and geostationary GEO ($\simeq 42000 \text{ km}$) satellites.

2.2.1 Non-spherical body's gravity

As long as Earth, the Moon, and the rest of the bodies do not have a perfect spherical shape, the mass distribution depends on latitude (ϕ) and longitude (λ). Therefore, it is not uniform as we supposed during the two-body problem analysis.

The advantage of this perturbation is that it is due to gravity, a conservative field. Therefore, we can characterise it in terms of a potential function. Using spherical coordinates to define this potential function ($U = U(r, \phi, \lambda)$), the Laplace equation results in the following:

$$\frac{1}{r^2} \frac{\partial}{\partial r} \left(r^2 \frac{\partial U}{\partial r} \right) + \frac{1}{r^2 \cos(\phi)} \frac{\partial}{\partial \phi} \left(\cos(\phi) \frac{\partial U}{\partial \phi} \right) + \frac{1}{r^2 \cos^2(\phi)} \frac{\partial^2 U}{\partial \lambda^2} = 0. \quad (2.14)$$

The solution for Eq. (2.14) that characterises the non-spherical body's gravity, deduced in [22], is given by:

$$U(r, \phi, \lambda) = \frac{\mu_{\oplus}}{r} \left[1 - \frac{R_{\oplus}}{r} \sum_{n=2}^{\infty} \sum_{m=0}^n J_{nm} \cdot p_{nm}(\sin(\phi)) \cos(m(\lambda - \lambda_{nm})) \right], \quad (2.15)$$

where the first term represents the potential of a sphere and the series represent the deviation with respect to the spherical model, J_{nm} and λ_{nm} are the coefficients associated to the nm^{th} harmonic and $p_{nm}(x)$ are the Legendre polynomials [25] of degree n and order m .

The trigonometric argument of the Legendre polynomials in Eq. (2.15) constitutes surface spherical harmonics, for they are periodic on the surface of a unit sphere. These spherical harmonics can be classified in three groups:

- **Zonal Harmonics:** They are defined by zeroth order ($m = 0$). This implies that the dependence of the potential on longitude (λ) vanishes and the field is symmetrical about the polar axis, appearing $n + 1$ horizontal zones dividing Earth. J_2 is, by far, the strongest perturbation due to Earth's shape.
- **Sectorial Harmonics:** They occur when the degree is equal to the order of the harmonic ($n = m$). When this happens, the polynomials are zero at the poles and Earth is divided into $2n$ meridians sectors.

- **Tesseral Harmonics:** For cases in which $n \neq m \neq 0$, the tesseral harmonics attempt to model specific regions of Earth that depart from a perfect sphere.

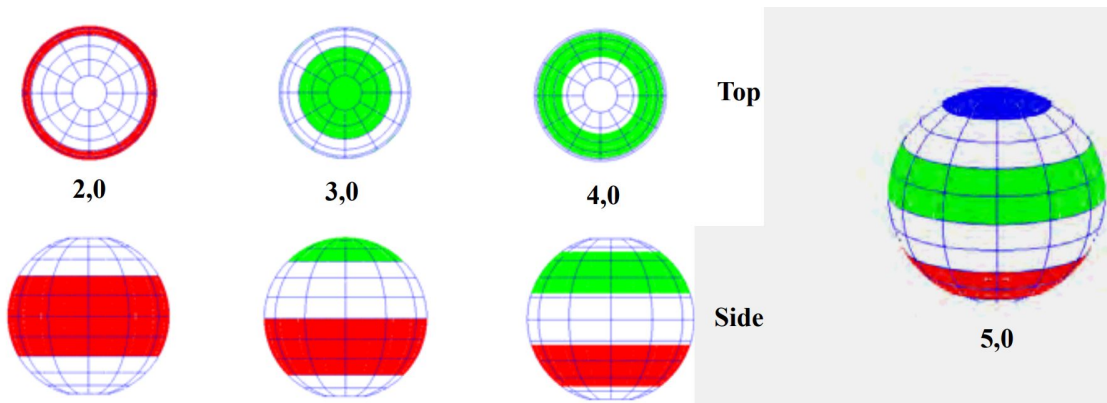


Figure 2.4 Zonal Harmonics. The shading indicates regions of additional mass and the numbers link regions between the views [22].

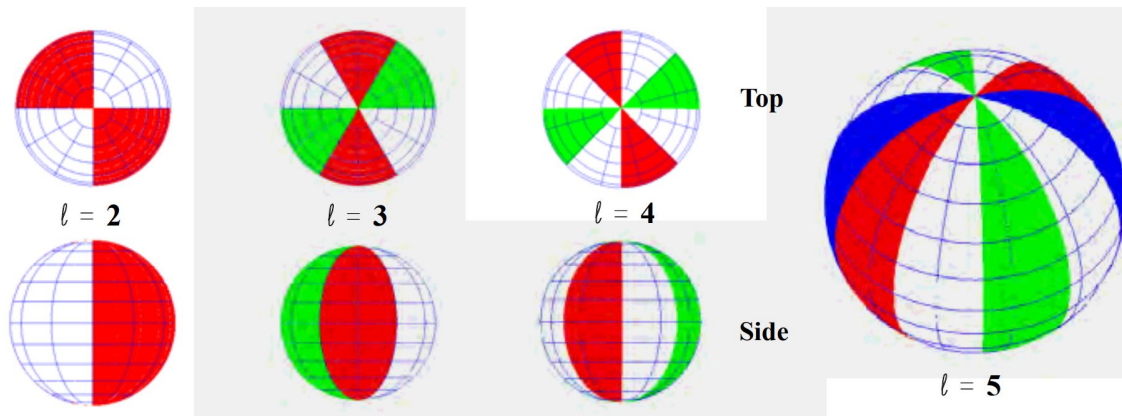


Figure 2.5 Sectorial Harmonics. They take into account the extra mass distribution in longitudinal regions [22].

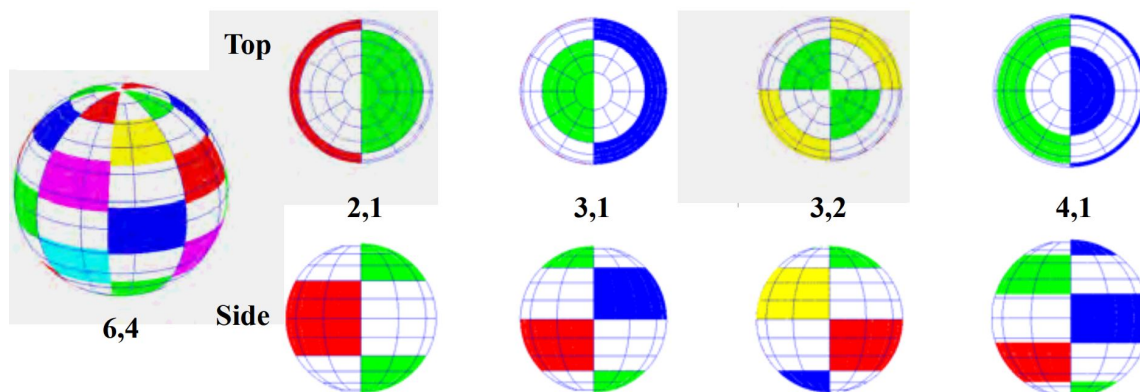


Figure 2.6 Tesseral Harmonics, which are dependent on latitude and longitude [22].

The precision of non-spherical body's gravity depends on how many harmonics are taken into study, increasing along with the computation complexity and time required to evaluate this force.

In order to perform the comparison between the Keplerian force and the perturbation force that arises from the non-spherical mass distribution of Earth, we use $\vec{\gamma} = \nabla U$.

Redefining Eq. (2.15) as

$$U(r, \phi, \lambda) = \frac{\mu_{\oplus}}{r} - \mu_{\oplus} \frac{R_{\oplus}}{r^2} \sum_{n=2}^{\infty} \sum_{m=0}^n J_{nm} \cdot p_{nm}(\sin(\phi)) \cos(m(\lambda - \lambda_{nm})) = U_K^{\oplus} + U_P^{harm} \quad (2.16)$$

we have that:

$$\vec{\gamma} = \vec{\gamma}_K^{\oplus} + \vec{\gamma}_P^{harm}. \quad (2.17)$$

Notice that $\vec{\gamma}_P^{harm}$ includes all the accelerations due to non-spherical body perturbations, which can be reviewed in [22]. On the other hand, $\vec{\gamma}_K^{\oplus} = -\mu_{\oplus} \frac{\vec{r}}{r^3}$ represents the acceleration due to the Keplerian force.

The most important non-spherical perturbation is the one due to the zonal harmonic J_2 , as we mentioned before. Its magnitude, compared with the Keplerian force, is $\zeta(\vec{\gamma}_K^{\oplus}, \vec{\gamma}_P^{J_2}) = 10^{-3}$ for LEO and $\zeta(\vec{\gamma}_K^{\oplus}, \vec{\gamma}_P^{J_2}) = 10^{-6}$ for GEO. It is, by far, the strongest perturbation affecting LEO objects and it has the same magnitude as the Sun and the Moon third-body perturbations in GEO altitudes. The next two strongest harmonics, J_{22} and J_3 , are 1000 times weaker than J_2 .

2.2.2 Atmospheric drag

Atmospheric drag strongly influences the motion of a satellite near Earth. During the last revolutions of the satellite's life, drag effects can be even greater than those from Earth's oblateness.

The acceleration due to drag is given by:

$$\vec{\gamma}_P^{drag} = -\frac{1}{2} \frac{C_D S}{m} \rho v_{rel}^2 \frac{\vec{v}_{rel}}{|\vec{v}_{rel}|}, \quad (2.18)$$

being C_D the drag coefficient, S the surface of the object, m its mass, ρ the density of the air at the specific altitude of the satellite and v_{rel} the relative velocity of the object with respect to the air.

The most difficult perturbation to model is, by far, the atmospheric drag. It is due to the difficulty to determine the density of the air at the altitude the satellite is in each period of time. Several models can be used to characterise density: from *static models*, where we assume that all the atmospheric parameters remain constant, to *time-varying models*, as we consider more and more real-world effects, such as diurnal variations, 27-days solar-rotation cycle, 11-year cycle of Sun spots, rotating atmosphere, winds, electromagnetic field, magnetic-storms variations, etc [22].

As we consider more and more real-world effects, more and more problems appear, as density, which varies enormously depending on the day, latitude and longitude, depends on varying parameters such as sunlight, winds, tides, etc. This summarises the complexity of accurately modelling the atmosphere and, thus, the atmospheric drag.

Nevertheless, there are many atmospheric models that allow the user to study this perturbation with higher or lower precision depending on the model used. In this project we present five of the most commonly used:

- **Exponential Model**

This static model is the simplest of the five models described in this project, as it assumes

that the density decays exponentially with respect to altitude and a spherical symmetry of particles. Thus, the density is given by:

$$\rho(h) = \rho_0 \exp\left(-\frac{h-h_0}{H}\right), \quad (2.19)$$

where ρ_0 is the density of reference (typically at sea level), h is the altitude, h_0 is the altitude of reference (typically sea level) and H is the scale height.

- **International Standard Atmosphere (ISA)**

In this model, which is static, it is assumed that density decays as a power function of temperature, which varies linearly with respect to altitude. The parameters depend on the layer of the atmosphere from which we want to evaluate the density. This is:

$$\rho(h) = \rho_0 \left(1 + \frac{\alpha(h_0)(h-h_0)}{T_0}\right)^{-\left(\frac{g}{R_g \alpha(h_0)} + 1\right)} \quad (2.20)$$

where h_0 is the altitude of reference depending on the layer of the atmosphere, $\alpha(h_0)$ is the thermal gradient of the air at h_0 , T_0 is the temperature of reference at h_0 , ρ_0 is the density of reference at h_0 , $R_g = 287.05 \text{ J/(kgK)}$ is the air constant and $g = 9.80665 \text{ m/s}^2$ is the gravity of Earth, which is assumed to remain constant in this model.

- **Harris-Priester**

This model is static, but takes into account several tables to measure the density variations that we may observe during the solar cycle. From these tables, this model interpolates the densities values to determine at a specific time and determines the physical properties of the upper atmosphere by averaging several of the predominant variations mentioned before. This model is widely recommended for comparing propagation algorithms, as it provides accurate results and is computationally efficient. This model is presented in detail in [17].

- **NRLMSISE-00**

The Naval Research Laboratory Mass Spectrometer and Incoherent Scatter Radar Exosphere (NRLMSISE-00) [21], which is extremely popular for all applications, computes the neutral atmosphere empirical model from the surface to lower exosphere (0 to 1000 km) and provides the exospheric temperature above satellite's altitude, local temperature at satellite's altitude, density at satellite's altitude and partial densities at satellite's altitude for He, H, N, O, Ar, N₂, O₂ and anomalous oxygen. This model needs geographical and time information to compute general values, but also needs space weather data, such as mean and daily solar flux and geomagnetic indices.

- **Jacchia-Bowman 2008**

Jacchia's models are widely used in military operations and some analyses for astrodynamics. In 2008, Bowman et al. [6] published an empirical model based on Jacchia's diffusion equations that computes the solar indices used for the solar irradiation from on-orbit sensor data. This model is the most recent of the five exposed in this section and, as a result, the use of new global exospheric temperature equations based on EUV and FUV solar indices significantly improves density modeling, especially at solar minimum times. In addition, in the authors' words, "density standard deviation errors during non-storm periods have been reduced by over 5% from Jacchia 70 and NRLMSIS models", the previous versions of Jacchia-Bowman and NRLMSISE-00.

To compare the Keplerian force with the drag in LEO, we consider some typical values for the terms appearing in Eq. (2.18) for a satellite with solar panels. Let $C_D = 1.5$, $S = 7 \text{ m}^2$, $m = 1800 \text{ kg}$,

$\rho = 10^{-13} \text{ kg/m}^3$ and $v_{rel} = 7.55 \text{ km/s}$. We have assumed an altitude of 600 km , calm atmosphere and circular orbit. With this, the comparison of the forces is $\zeta(\vec{\gamma}_K^\oplus, \vec{\gamma}_P^{drag}) = 10^{-6}$. Nevertheless, it is the most important perturbation in LEO because it makes the orbit decay by slowing the satellite.

2.2.3 Third-Body perturbations

In the two-body problem we isolated the system and supposed there was just two bodies. However, in the solar system there are thousands of object which perturb the orbit of the satellite. Depending on the mass and proximity of these objects to the system under study, the force caused is greater or lesser.

Suppose an orbiting object around Earth, affected by the gravitational force of Earth and the Moon.

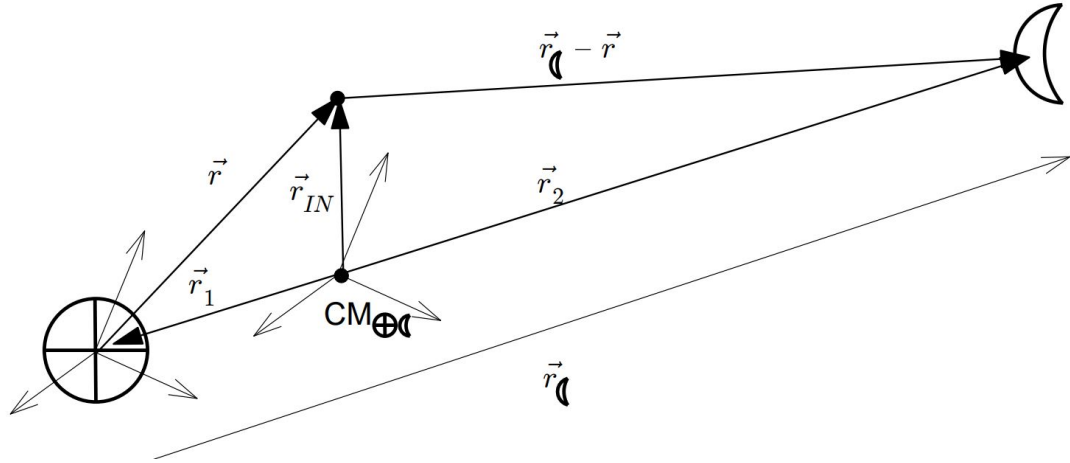


Figure 2.7 Object orbiting Earth affected by the Moon [25].

In this problem, the motion equation written in the inertial reference system centred in $CM_{\oplus\zeta}$ is:

$$\ddot{\vec{r}}_{IN} = -\mu_{\oplus} \frac{\vec{r}}{r^3} + \mu_{\zeta} \frac{\vec{r}_{\zeta} - \vec{r}}{|\vec{r}_{\zeta} - \vec{r}|^3}, \quad (2.21)$$

where $\vec{r}_{\zeta} = \vec{r}_2 - \vec{r}_1$. We also have that \vec{r}_1 and \vec{r}_2 satisfy

$$m_{\oplus} \vec{r}_1 + m_{\zeta} \vec{r}_2 = \vec{0} \quad (2.22)$$

and that the motion equation of the Moon is

$$\ddot{\vec{r}}_{\zeta} = -\frac{G(m_{\oplus} + m_{\zeta}) \vec{r}_{\zeta}}{r_{\zeta}^3}. \quad (2.23)$$

Combining Eq. (2.22) and Eq. (2.23), we get

$$\ddot{\vec{r}}_1 = \frac{\mu_{\zeta} \vec{r}_{\zeta}}{r_{\zeta}^3}. \quad (2.24)$$

Finally, as $\vec{r}_{IN} = \vec{r} + \vec{r}_1$, the following result emerges:

$$\ddot{\vec{r}} = -\mu_{\oplus} \frac{\vec{r}}{r^3} + \mu_{\zeta} \frac{\vec{r}_{\zeta} - \vec{r}}{|\vec{r}_{\zeta} - \vec{r}|^3} - \frac{\mu_{\zeta} \vec{r}_{\zeta}}{r_{\zeta}^3} = \vec{\gamma}_K + \vec{\gamma}_P, \quad (2.25)$$

where $\vec{\gamma}_K = -\mu_{\oplus} \frac{\vec{r}}{r^3}$ is the Keplerian acceleration and $\vec{\gamma}_P = \mu_{\zeta} \frac{\vec{r}_{\zeta} - \vec{r}}{|\vec{r}_{\zeta} - \vec{r}|^3} - \frac{\mu_{\zeta} \vec{r}_{\zeta}}{r_{\zeta}^3}$ is the acceleration due to the third body.

Linearising $\vec{\gamma}_P$, we get that the perturbation acceleration can be estimated as:

$$\vec{\gamma}_P \simeq \frac{\mu_{\zeta}}{r_{\zeta}^3} \left[3\vec{r}_{\zeta} \frac{\vec{r}_{\zeta} \cdot \vec{r}}{r_{\zeta}^2} - \vec{r} \right] \sim \mu_{\zeta} \frac{r}{r_{\zeta}^3}. \quad (2.26)$$

Note that in this analysis we used a system formed by Earth and the Moon, but these accelerations and equations can be generalised for any system by substituting in $\vec{\gamma}_K$ the gravitational parameter of the main body and in $\vec{\gamma}_P$ the gravitational parameter of the perturbing body and its reference vector. Hence, we can compare the third-body perturbation with the Keplerian acceleration using Eq. (2.13). This results in:

$$\zeta(\vec{\gamma}_P, \vec{\gamma}_K) = \frac{|\vec{\gamma}_P|}{|\vec{\gamma}_K|} \sim \frac{\mu_P}{\mu_S} \left(\frac{r}{r_P} \right)^3, \quad (2.27)$$

where μ_S is the standard gravitational parameter of the main body of the system (the main body being the one around the object of study orbits), μ_P is the standard gravitational parameter of the perturbing third-body, r is the distance from the main body to the orbiting object and r_P is the distance between the main body and the third-body. This equation provides an estimation of the magnitude of the third-body perturbation acceleration and allows us to decide which solar system objects take into account.

Observing Eq. (2.27) we deduce that only objects with enough mass or close to Earth produce the greatest third-body perturbations. To verify these conclusions, the following table presents the comparison between the forces exerted by Earth, the Moon and the solar system main objects to LEO and GEO satellites:

Table 2.2 Comparison between the forces exerted by the Moon and the main solar system objects and the force Earth produces on LEO and GEO satellites.

Satellite	Sun	Moon	Mercury	Venus	Mars	Jupiter	Saturn	Uranus	Neptune	Pluto
LEO	10^{-8}	10^{-7}	10^{-13}	10^{-11}	10^{-15}	10^{-13}	10^{-14}	10^{-16}	10^{-17}	10^{-21}
GEO	10^{-5}	10^{-5}	10^{-11}	10^{-8}	10^{-12}	10^{-10}	10^{-12}	10^{-14}	10^{-15}	10^{-18}

Based on these results, we can conclude that the most important third-body perturbations are the ones due to the Sun and the Moon, which is what we expected in geocentric orbits. The combination of these perturbations is usually called Luni-Solar perturbation. The addition of other planets' perturbations is not relevant, as their forces are 3 or more orders of magnitude below the ones exerted by the Sun and the Moon.

2.2.4 Solar-Radiation pressure

The incidence of sunlight on the surface of any body produces a mechanical effect called solar-radiation pressure (SRP). It is, like drag, a non conservative perturbation. However, it becomes more pronounced at higher altitudes.

As well as modelling drag was tremendously difficult due to the constant variations in the atmosphere, the difficulty in modelling SRP lies on modelling accurately solar cycles and variations. Solar storms produce an increase in this effect. To characterise this force we also need the apparent size of the satellite that faces the Sun in each moment, since the area exposed to the Sun depends on the attitude of the satellite. This means that the pressure distribution is directly based upon the satellite's shape, composition and orientation with respect to the Sun. Apart from this considerations,

the Sun position and the amount of sunlight affecting the satellite are crucial in determining this perturbation effect.

The acceleration due to SRP can be estimated as follows [22]:

$$\vec{\gamma}_P^{SRP} \simeq -\frac{I(1+\varepsilon)S_{SRP}\cos(\varphi_{\odot})}{mc}\vec{e}_{\odot}, \quad (2.28)$$

where I is the solar radiation flux, S_{SRP} is the exposed surface of the satellite, ε is the reflectivity coefficient (1 if the body is completely reflective, 0 if it is a black-body and -1 if it is transparent), m is the mass of the satellite, c is the light speed, φ_{\odot} is the angle of incidence of the sunlight and \vec{e}_{\odot} is a unit vector that points towards the Sun from the satellite.

In addition to Eq. (2.28), a similar magnitude acceleration due to reflection occurs in every single surface exposed to sunlight and we must take into account the albedo of Earth too, the solar radiation reflected from Earth back onto the satellite. The amount of sunlight reflected due to the albedo is about 30%.

We compare $\vec{\gamma}_K$ with $\vec{\gamma}_P^{SRP}$ using typical values for LEO and GEO. Considering $I = 1367 \text{ W/m}^2$, $S_{SRP} = 3 \text{ m}^2$, $\varepsilon = 0.2$, $\varphi_{\odot} = 0^\circ$, $c = 299792458 \text{ m/s}$, $m_{LEO} = 2100 \text{ kg}$ and $m_{GEO} = 900 \text{ kg}$, we get $\zeta_{LEO}(\vec{\gamma}_K^{\oplus}, \vec{\gamma}_P^{SRP}) = 10^{-7}$ and $\zeta_{GEO}(\vec{\gamma}_K^{\oplus}, \vec{\gamma}_P^{SRP}) = 10^{-5}$.

2.2.5 Other effects

We modelled and studied the four main perturbations affecting geocentric satellites. However, many other effects affect them. Here we present the main ones:

- **Tides:** Solid-Earth tides or Ocean tides have only recently been studied thanks to the advances in computation and observation processes. These gravitational perturbations are caused by an external body. In the case of Earth, the Moon and the Sun affect Earth oblateness periodically. It is usual to model the tidal potential produced on Earth as a harmonic expression, similar as the one described in Eq. (2.15).
- **Precession of Earth's axis:** This is the change in orientation of the rotation axis of Earth due to the Sun gravitational attraction, the inclination of the ecliptic and Earth's aspherical shape. It has a period of 26000 years approximately.
- **Nutation of Earth's axis:** It is a swaying motion in the axis of rotation of the Earth, caused by the Moon gravitational attraction. Its period is around 18.6 years and it slightly affects the inclination of the ecliptic.
- **Apparent Polar Wander:** This phenomenon is the perceived movement of the Earth's paleo-magnetic poles relative to a continent while regarding the continent being studied as a fixed in position. It produces a displacement of the pole of metres. It is caused by the movements in Earth's mantle and crust and the redistribution of the water bodies at the surface.
- **Magnetic Field Effects:** The force exerted by Earth's magnetic field on the satellites orbiting around, which is given by Maxwell's equations.
- **South Atlantic Anomaly:** This region of the Van Allen belts extends to Earth surface and is a dip centred over South America and the South Atlantic.

These effects are analysed in detail in [24] and [22]. Note that we did not mention thrust, as we know when the satellites perform a manoeuvre and the amount of velocity they gain due to this manoeuvre.

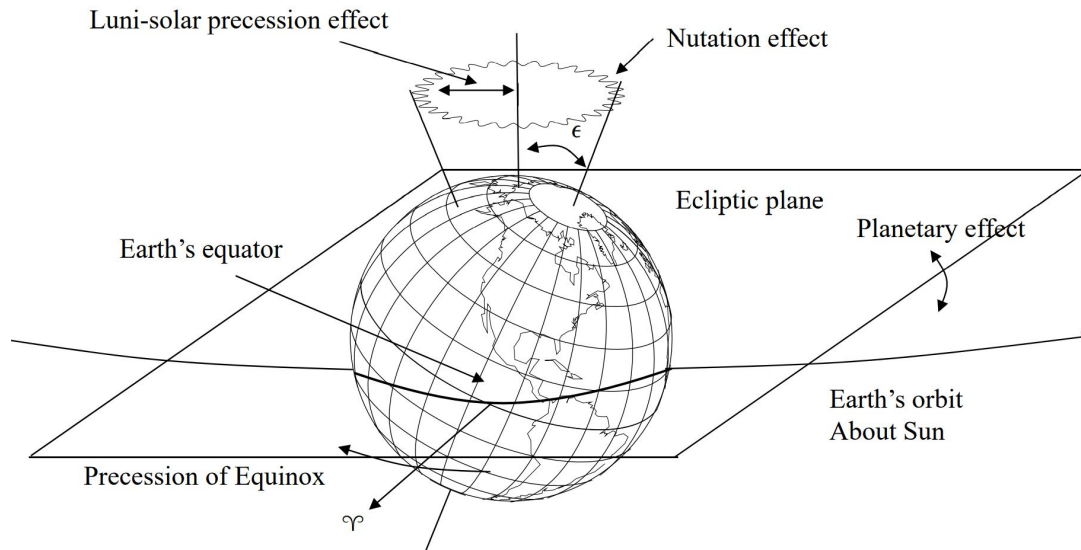


Figure 2.8 Precession and nutation of Earth's axis [22].

In order to obtain a high accuracy model that propagates the orbit of the satellites under study we should take into account as many perturbations as possible. The precession of Earth's axis and the nutation of Earth's axis affect the reference system used to determine the satellites' orbit. These movements produce errors of dozens of metres if they are not considered. Fortunately, Orekit (the library described in Chapter 3 used in this project to propagate the orbits) considers these effects when propagating orbits. On the other hand, the position of the pole and Earth's axis must be taken into account when considering the nonspherical body's gravity. Thus, the apparent polar wander and the precession and nutation of Earth's axis are effects that we need to consider when precisely studying the orbit of geocentric satellites. Conversely, the South Atlantic Anomaly is just a region of radiation that we shall take into account when designing missions in order to avoid the effects of cosmic radiation and does not cause a significant variation. The two effects left (tides and magnetic field effects) are perturbations that we shall consider during the design of the propagator in Section 4.2, but as Orekit has not got any electromagnetic force model, we only study tides.

3 Introduction to Orekit

Orekit [14] is a low-level space dynamics library written in Java. It has gained widespread recognition since it was released under an open source license in 2008. In this chapter, this tool is introduced, since it is used to perform all computational analyses throughout this thesis.

3.1 About Orekit

Orekit is a space flight dynamics library developed since 2002 by CS Group, and since 2008 the tool is freely available as an open source product under the terms of the business-friendly Apache V2.0 licence. This library aims at providing accurate and efficient low-level components in space flight dynamics applications and it is designed to be easily used in very different contexts, from quick studies up to critical operations. It is a pure Java library that depends only on the Java Standard Edition version 8 (or above) and Hipparchus version 2.0 (or above) libraries at run-time. Hipparchus is a library of lightweight, self-contained mathematics and statistics components addressing the most common problems not available in the Java Standard Edition. Orekit is used, among others, by:

- Airbus Defence and Space in Quartz.
- U.S. Naval Research Laboratory.
- Swedish Space Corporation.
- Thales Alenia Space.
- Centre National d'Études Spatiales.
- European Space Agency.

These organisations also contribute or have contributed to the development of Orekit library.

As a library, Orekit provides basic elements (orbits, dates, attitude, frames, etc) and various algorithms to handle them (conversions, propagations, pointing, etc). It features all classical concepts needed for space flight dynamics and it offers an extensive support for each concept. The main driving goals for the development of Orekit are validation, robustness, maintainability and efficiency.

3.2 Orekit features

3.2.1 Time

The *Time* package is an independent package providing classes to handle epochs and time scales, and to compare instants. The principal class is *AbsoluteTime*, which represents an unique instant in

time, so as to be able to locate it with respect to the many different time scales. The Time package provides high accuracy absolute dates, time scales, transparent handling of leap seconds and support for CCSDS time code standards. [3].

There are several time scales that Orekit provides in the *TimeScalesFactory* class:

- **International Atomic Time TAI**: the most accurate and regular time scale that can be used at the surface of Earth.
- **Terrestrial Time TT**: it is the successor of Ephemeris Time TE. By convention, $TT = TAI + 32.184\text{ s}$.
- **Universal Time 1 UT1**: it is a time scale directly linked to the actual rotation of Earth. It is an irregular scale, reflecting Earth's irregular rotation rate.
- **Universal Time Coordinate UTC**: it is the primary time standard by which the world regulates clocks and times. It is mainly related to TAI, but some step adjustments are introduced from time to time to keep into account Earth rotation irregularities and to prevent the legal time from drifting with respect to day and night. The offset between UT1 and UTCScale is found in the Earth Orientation Parameters published by IERS.
- **Greenwich Mean Sidereal Time scale GMST**: it is the hour angle between the meridian of Greenwich and mean equinox of date at 0 h UT1.
- **Geocentric Coordinate Time TCG**: coordinate time at the centre of mass of Earth. This time scale depends linearly on TTScale (and, hence, on TAI).
- **Barycentric Dynamical Time TDB**: time used to compute ephemerides in the solar system. This time is offset with respect to TT by small relativistic corrections due to Earth's motion.
- **Barycentric Coordinate Time TCB**: coordinate time used for computations in the solar system. This time scale depends linearly on TDBScale.
- **Global Positioning System reference scale TGPS**: this scale was equal to UTC at the start of the GPS epoch when UTC was 19 seconds behind TAI, and has stayed parallel to TAI since then. By convention, $TGPS = TAI - 19\text{ s}$.
- **Galileo System reference scale TGS**: this scale is equal to UTC + 13 s at Galileo epoch (1999-08-22T00:00Z). Galileo System Time and GPS time are very close scales. Without errors, they should be identical. The offset between these two scales is the GGTO, which depends on the clocks used to realise the time scales. It is of the order of a few nanoseconds.
- **GLONASS System reference scale GLONASS**: this scale is equal to UTC + 3 h at any time. GLONASS System Time does not include leap seconds just at UTC scale.
- **Quasi-Zenit reference scale QZSS**: it is very close to GPS scale. The same difference with GPS as Galileo.

3.2.2 Frames

The *Frames* package provides classes to handle frames and transforms between them. All frames are organised as a tree with a single root, being the relationship between elements the transform that links one to another. Each frame is defined by a single *TransformProvider* linking it to one specific frame: its parent frame. This defining transform provider may give either fixed or time-dependent transforms. As an example, Earth related frame ITRF depends on time due to precession/nutation, Earth's rotation and pole motion. The predefined root frame is the only one with no parent frames. For each pair of frames, there is one single shortest path from one frame to the other one.

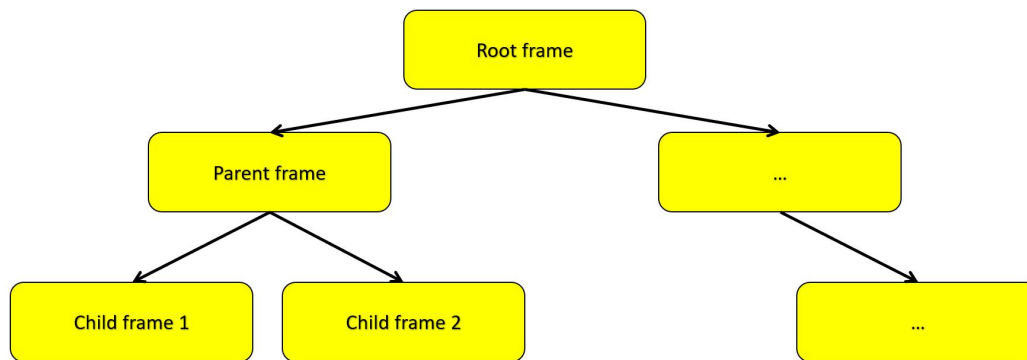


Figure 3.1 Frame transformation tree.

To transform between two frames, the *Transform* class is used. It can convert position, directions and velocities from one frame to another, including velocity composition effects. Transforms are used to define the relationship from a parent to a child frame and to merge all individual transforms encountered while walking the tree from one frame to any other one, however far away they are from each other. The transform between any two frames is computed by merging individual transforms while walking the shortest path between them. The walking/merging operations are handled transparently by the library. Users only need to select the frames, provide the date and ask for the transform, without knowing how the frames are related to each other.

For studies in Earth, Orekit provides predefined reference frames that the user can implement in their studies. For most purposes, the recommended frames are the International Terrestrial Reference Frame (ITRF) for terrestrial frame and Geocentric Celestial Reference Frame (GCRF) for celestial frame. In summary, Orekit implements the following Earth's frames:

- those related to the Non-Rotating Origin: GCRF, CIRF, TIRF and ITRF for all precession and nutation models from IERS 1996, IERS 2003 and IERS 2010.
- those related to the Equinox-based origin: MOD, TOD, GTOD and equinox-based ITRF for all precession and nutation models from IERS 1996, IERS 2003, IERS 2010 and Veis 1950.

One predefined set corresponds to the frames from the IERS conventions (2010). This set defines the GCRF reference frame on the celestial (i.e. inertial) side, the ITRF on the terrestrial side and several intermediate frames between them. Several versions of ITRF have been defined. Orekit supports several of them thanks to Helmert transformations [26].

The two big frames groups defined above are based on IERS definitions [20]:

- Based on Celestial Intermediate Origin CIO:
 - Geocentric Celestial Reference Frame GCRF.
 - Celestial Intermediate Reference Frame CIRF 2000.
 - Terrestrial Intermediate Reference Frame TIRF 2000 (with or without tides).
 - International Terrestrial Reference Frame ITRF 2005 (with or without tides).
- Based on Equinox:
 - Geocentric Celestial Reference Frame GCRF.
 - J2000 EME2000.
 - Mean equator Of Data MOD (with or without EOP correction).
 - True equator Of Data TOD (with or without EOP correction).

- Greenwich True Of Date GTOD (with or without EOP correction).
- Veis 1950.
- equinox-based ITRF.

The transformations between each of the frames defined above are represented in Figure 3.2 and.

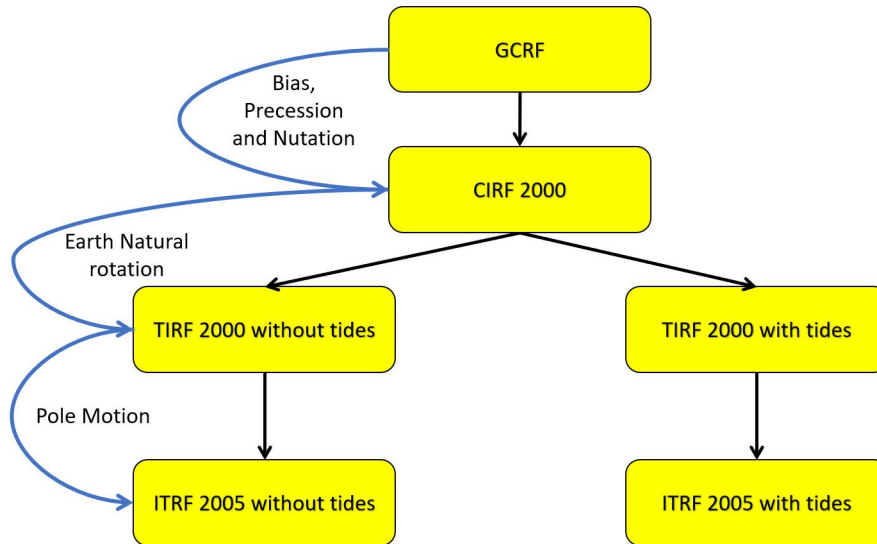


Figure 3.2 CIO-based transformations.

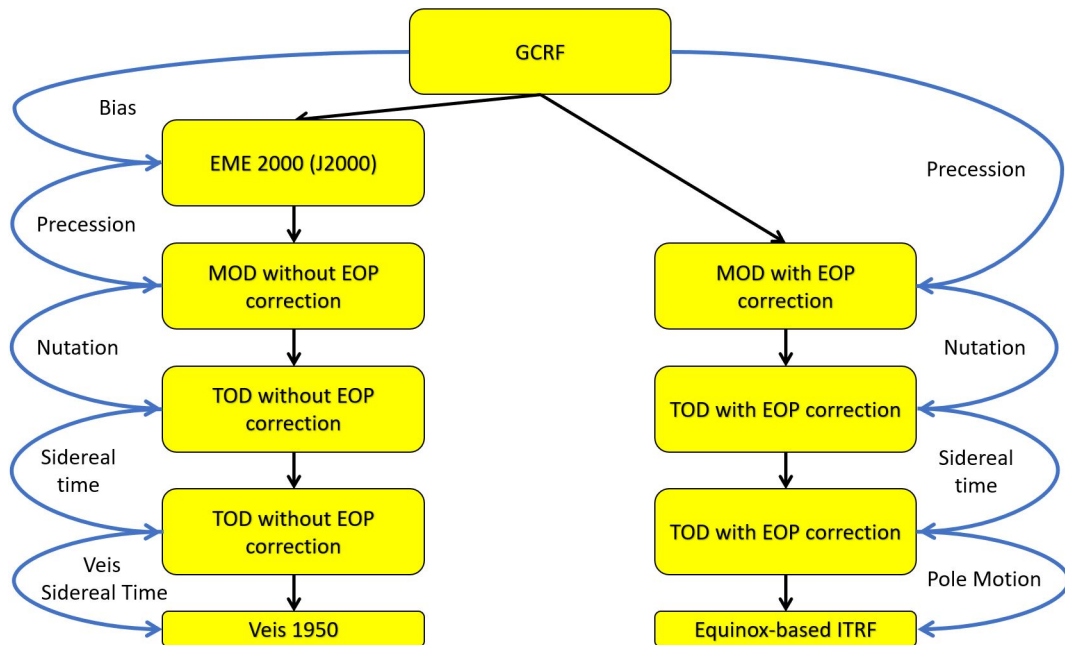


Figure 3.3 Equinox-based transformations.

In the first group, tidal effects are also taken into account on Earth rotation angle and on pole motion. The 71-term model from IERS is used. Since this model is also computing intensive, a caching/interpolation algorithm is also used to avoid a massive effect on performance. The trade-off

selected for Orekit implementation is to use 8 points separated by $3/32$ day (135 minutes) each. The resulting maximal interpolation error is about 3 micro-arcseconds. The penalty to use tidal effects is therefore limited to slightly more than 20%, to be compared with the 550% penalty without this mechanism.

All celestial bodies are linked to their own body-centered inertial frame, just as Earth is linked to EME2000 and GCRF. Since Orekit provides implementations of the main solar system celestial bodies, it also provides body-centered frames for these bodies, one inertially oriented and one body oriented. The orientations of these frames are compliant with IAU poles and prime meridians definitions. The predefined frames are the Sun, the Moon, the eight planets and the Pluto dwarf planet. In addition to these real bodies, two points are supported for convenience as if they were real bodies: the solar system barycenter and the Earth-Moon barycenter; in these cases, the associated frames are aligned with EME2000. One important case is the solar system barycenter, as its associated frame is the ICRF. The frame list is the following:

- Geocentric Celestial Reference Frame GCRF.
- J2000 EME 2000.
- Moon-centered.
- Earth-Moon barycenter.
- Solar system barycenter.
- Object-centered (Sun-centered, Mercury-centered, etc).

The topocentric frame model (Figures 3.4 and 3.5) allows defining the frame associated with any position at the surface of a body shape, which itself is referenced to a frame, typically ITRF for Earth. The frame is defined with the following canonical axes:

- Zenith direction (Z) is defined as the normal to local horizontal plane.
- North direction (Y) is defined in the horizontal plane (normal to zenith direction) and following the local meridian.
- East direction (X) is defined in the horizontal plane, in order to complete the direct triangle (East, North, zenith).

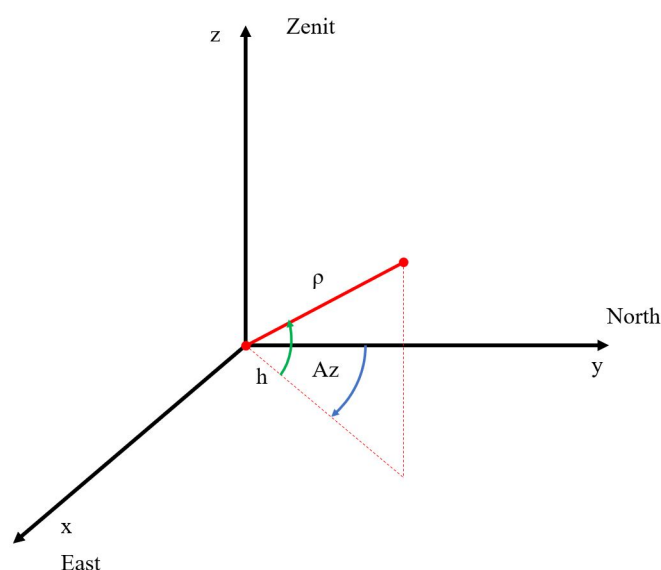


Figure 3.4 Topocentric frame.

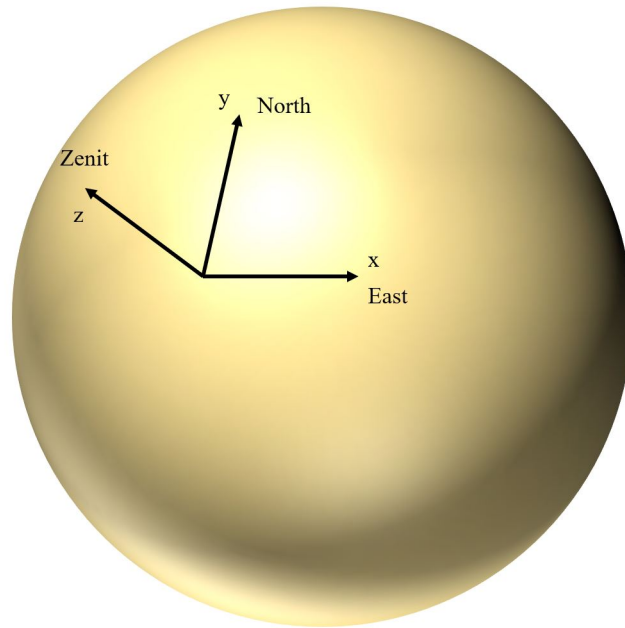


Figure 3.5 Object view of topocentric frame.

3.2.3 Forces

Orekit provides an extensive package to model forces. These forces are defined by the user, in order to implement them automatically by Orekit in the numerical propagator selected.

Objects that implement the force model interface are intended to be added to a numerical propagator before the propagation starts. The propagator calls at each step the force model contribution computation method, to be added to its time derivative equations. The force model instance extracts all the state data it needs (date, position, velocity, frame, attitude, mass) from the *SpacecraftState* parameter. From these state data, it computes the perturbing acceleration. It then adds this acceleration to the second parameter which takes this contribution into account and uses the Gauss equations to evaluate its impact on the global state derivative. Force models that create discontinuous acceleration patterns (typically for manoeuvres start/stop or solar eclipses entry/exit) must provide one or more events detectors to the propagator thanks to their *getEventsDetectors()* method. This method is called once just before propagation starts. The events states are checked by the propagator to ensure accurate propagation and proper events handling.

The force models implemented are as follows:

- Atmospheric drag forces, taking into account the attitude if the shape of the spacecraft is defined.
- Central gravity forces, including time-dependent parts (linear trends and pulsation at several different periods).
- Third body gravity force. Data for all solar system bodies is available, based on JPL DE ephemerides or IMCCE INPOP ephemerides.
- Solar radiation pressure force, taking into account force reduction in penumbra and no force at all during complete eclipse, and taking attitude into account if spacecraft shape is defined.
- Solid tides, with or without solid pole tide.
- Ocean tides, with or without ocean pole tide.
- Post-Newtonian correction due to general relativity.

- Forces induced by manoeuvres. At present, only constant thrust manoeuvres are implemented, with the possibility to define an impulse manoeuvre, thanks to the event detector mechanism.

3.2.4 Attitudes

Some force models, such as the atmospheric drag for manoeuvres, need the spacecraft orientation in an inertial frame. Orekit uses a simple container for Attitude, which includes both the geometric part (i.e. rotation) and the kinematic part (i.e. the instant spin axis). The components held by this container allow to convert vectors from inertial frame to spacecraft frame along with their derivatives. This container is similar in spirit to the various extensions of the abstract Orbit class: it represents a state at a specific instant. In order to represent attitude evolution in time, the *AttitudeProvider* interface is available. At a higher level, attitude laws defined by a ground pointing law are also available. This corresponds to a real situation where satellite attitude law is defined in order to perform a mission, i.e. pointing a specified point/area. All these laws are collected under an abstract class called *GroundPointing*. Finally, there exist attitude laws that wrap a “base” attitude law, and add to this base attitude law a complementary rotation in order to fulfil specific mission constraints.

Nevertheless, in this project the orientation of satellites is not available, so the description of the different attitude providers that Orekit implement is omitted.

3.2.5 Orbits

This package is the basis for all of the other space mechanics tools. It provides an abstract class, Orbit, extended in four different ways corresponding to the different possible representations of orbital parameters. Since version 3.0, Keplerian, circular, equinoctial and Cartesian representations are supported. For orbit evolution computation, this package is not sufficient. There is a need to include notions of dynamics, forces models, propagation algorithms, etc. The entry point for this is the Propagator interface.

Available orbit representations are:

- Classical elliptical Keplerian orbit. This representation is the most well known, being the one used in this project to present the final results of the analyses. They are given by:
 - a: semi-major axis [m].
 - e: eccentricity [~].
 - i: inclination [rad].
 - ω : perigee argument [rad].
 - Ω : right ascension of the ascending node [rad].
 - θ , M or E: true anomaly, mean anomaly or eccentric anomaly [rad].
- Circular orbit, used to represent almost circular orbit, i.e orbit with low eccentricity, characterised by:
 - a: semi-major axis [m].
 - $e_x = e \cdot \cos(\omega)$: X component of the eccentricity vector [~].
 - $e_y = e \cdot \sin(\omega)$: Y component of the eccentricity vector [~].
 - i: inclination [rad].
 - Ω : right ascension of the ascending node [rad].
 - $u_\theta = \omega + \theta$, $u_M = \omega + M$ or $u_E = \omega + E$ [rad].

- Equinoctial orbit. This kind of orbital elements can represent every type of orbit and, as they do not have any singularities, they are used in this project to compute the orbits because of their reliability. They are given by:
 - a : semi-major axis [m].
 - $e_x = e \cdot \cos(\omega + \Omega)$: X component of the eccentricity vector [~].
 - $e_y = e \cdot \sin(\omega + \Omega)$: Y component of the eccentricity vector [~].
 - $h_x = \tan(i/2) \cdot \cos(\Omega)$: X component of the specific relative angular momentum vector [~].
 - $h_y = \tan(i/2) \cdot \sin(\Omega)$: Y component of the specific relative angular momentum vector [~].
 - $\lambda_\theta = \omega + \Omega + \theta$, $\lambda_M = \omega + \Omega + M$ or $\lambda_E = \omega + \Omega + E$: respectively true longitude argument, mean longitude argument or eccentric longitude argument [rad].
- Cartesian orbit, associated to its frame definition.
 - (X, Y, Z) : position vector of the point in the given frame [m].
 - (V_x, V_y, V_z) : velocity vector of the point in the given frame [m/s].

Note that Two-Lines Elements are not considered an orbit representation here. This is because TLE are, in fact, a merge between orbital state and a propagation model. The state is only meaningful with respect to the associated SGP4/SDP4 propagation model, and cannot be used in any other model.

3.2.6 Two-Line Elements

TLE [23] orbits are supplied in two-line element format, then converted into an internal format for easier retrieval and future extrapolation. They can not be directly used as they are average orbital elements and they have to be transformed into traditional elements. All the values provided by a TLE only make sense when translated by the corresponding propagator. Even when no extrapolation in time is needed, state information (position and velocity coordinates) can only be computed through the propagator. Untreated values like inclination, RAAN, mean Motion, etc, can not be used by themselves without loss of precision. The implemented TLE model conforms to new 2006 corrected model.

The definition of each field in TLE is available in [8].

3.2.7 Bodies

The position of celestial bodies is represented by the *CelestialBody* interface. This interface provides the methods needed to either consider the body as an external one for its gravity or lighting influence on spacecraft (typically in perturbing force computations) or as an internal one with its own frame. By default, the *CelestialBodyFactory* retrieves positions and velocities from binary ephemerides files compatible with the JPL DE formats like DE 405, DE 406, DE 423, etc, as well as the IMCCE Inpop ephemerides which share a similar format. This default handling can be overridden by defining a user-specific loader for JPL ephemerides. The shape of celestial bodies is represented by the *BodyShape* interface.

3.2.8 Propagation

Propagation is the prediction of the evolution of a system from an initial state. In Orekit, this initial state is represented by a *SpacecraftState*, which is a simple container for all needed information :

orbit, mass, kinematics, attitude, date, frame, and which can also hold any number user-defined additional data like battery status or operating mode for example.

Depending on the needs of the calling application, all propagators can be used in different modes:

- **Slave mode:** this mode is used when the user wants to completely drive evolution of time with his own loop. The (slave) propagator is passive: it computes this result and returns it to the calling (master) application, without any intermediate feedback. Users often use this mode in loops, each target propagation time representing the next small time step. In that case the events detection is made but the step handler does nothing, actions are managed directly by the calling application.
- **Master mode:** this mode is used when the user needs to have some custom function called at the end of each finalised step during integration. The (master) propagator is active: the integration loop calls the (slave) application callback methods at each finalised step, through the step handler. Users often use this mode with only a single call to propagation with the target propagation time representing the end-end date.
- **Ephemeris generation mode:** this mode is used when the user needs random access to the orbit state at any time between the initial and target times, and in no sequential order. A typical example is the implementation of search and iterative algorithms that may navigate forward and backward inside the propagation range before finding their result.
Be aware that this mode cannot support events that modify spacecraft initial state. It should also be noted that since this mode stores all intermediate results, it may be memory intensive for long integration ranges and high precision short time steps.

The recommended mode by Orekit is the master mode. It is very simple to use and allows the user to get rid of concerns about synchronising force models, file output or discrete events. All these parts are handled separately in different user code parts, and Orekit takes care of all management.

All propagators, including analytical ones, support discrete events handling during propagation, as we mentioned in Section 3.2.3. This feature is activated by registering events detectors as defined by the *EventDetector* interface to the propagator, each *EventDetector* being associated with an *EventHandler* that will be triggered automatically at event occurrence. At each propagation step, the propagator checks the registered events detectors for the occurrence of some event. If an event occurs, then the corresponding action is triggered, which can notify the propagator to resume propagation (possibly with an updated state) or to stop propagation. Users can define their own events, typically by extending the *AbstractDetector* abstract class. There are also several predefined events detectors already available, amongst which *DateDetector*, *ElevationDetector*, *ElevationExtremumDetector*, *AltitudeDetector*, *EclipseDetector*, *FieldOfViewDetector*, *NodeDetector*, etc. We do not describe all of them as we do not use other than the *EclipseDetector*. This event detector is triggered when some body enters or exits the umbra or the penumbra of another occulting body.

Orekit provides several kind of propagators. We focus in three main groups: analytical, semi-analytical and numerical propagators.

- **Analytical propagation**
 - *Keplerian propagation* [9]: based on Keplerian motion. It depends only on μ . This model propagates the orbit assuming there are not perturbations acting, so the orbit is perfectly Keplerian.
 - *Eckstein-Hechler propagation* [11]: this model is suited for near circular orbits ($e < 0.1$, with poor accuracy between 0.005 and 0.1) and inclination neither equatorial (direct or retrograde) nor critical (direct or retrograde). It considers J_2 to J_6 potential zonal coefficients [9], and uses mean parameters to compute the new position.

- *SGP4/SDP4 propagation* [15]: this analytical model is dedicated to Two-Line Elements (TLE) propagation. The SGP4 and SDP4 models were published along with sample code in FORTRAN IV in 1988 with refinements over the original model to handle the larger number of objects in orbit since. The SGP4 model has an error ~ 1 km at epoch and grows at $\sim 1 - 3$ km per day. Deep space model SDP4 uses only “simplified drag” equations.
- *Global Navigation satellite system GNSS*: Orekit implements the propagators for GPS, QZSS, Galileo, GLONASS, Beidou, IRNSS and SBAS.
- *Differential effects adapter*: this model is used to add to an underlying propagator some effects it does not take into account. A typical example is to add small station-keeping manoeuvres to a pre-computed ephemeris or reference orbit which does not take these manoeuvres into account. The additive manoeuvres can take both the direct effect (Keplerian part) and the induced effect due, for example, to J_2 , which changes ascending node rate when a manoeuvre changed inclination or semi-major axis of a Sun-Synchronous satellite.
- **Semi-analytical propagation**: It is an intermediate between analytical and numerical propagation. It retains the best of both worlds, speed from analytical models and accuracy from numerical models. Semi-analytical propagation is implemented using Draper Semi-analytical Satellite Theory (DSST) [7].
- **Numerical propagation**: The numerical propagation allows the user to include as many perturbations as required. The available ones are:
 - central attraction.
 - gravity models including time-dependent like trends and pulsations (automatic reading of ICGEM (new Eigen models), SHM (old Eigen models), EGM and GRGS gravity field files formats, even compressed).
 - atmospheric drag.
 - third body attraction (with data for the Sun, Moon and all solar systems planets).
 - radiation pressure with eclipses.
 - solid tides, with or without solid pole tide.
 - ocean tides, with or without ocean pole tide.
 - Earth’s albedo and infrared.
 - empirical accelerations to account for the unmodeled forces.
 - general relativity (including Lense-Thirring [2] and De Sitter corrections).
 - multiple manoeuvres.
 - state of the art ODE integrators (adaptive stepsize with error control, continuous output, switching functions, G-stop, step normalization, etc).
 - computation of Jacobians with respect to orbital parameters and selected force models parameters.
 - serialisation mechanism to store complete results on persistent storage for later use.
 - propagation in non-inertial frames (e.g. for Lagrange point halo orbits).

3.3 Introductory examples

In this section we apply the concepts described in Section 3.2 to several cases, studying the effect of different kind of perturbations in the orbit of satellites around Earth. The inertial frame used is the J2000 and the initial date considered is 01-01-2021 at 12:00:00 UTC.

3.3.1 Geostationary satellite affected by the Sun and the Moon

A Geostationary satellite's orbit is a circular orbit designed to match Earth's rotation period on its axis (23 hours, 56 minutes and 4 seconds) and to have zero inclination (the orbital plane is the equator plane). The orbit must have a specific semi-major axis, near zero eccentricity and near zero inclination. As described in Section 3.2.5, for an almost circular orbit with almost null inclination the equinoctial elements are used to avoid θ , ω and Ω being not well defined.

The orbit is propagated during an 80-year period. The equinoctial elements are $a = 42164.14 \text{ km}$, $e_x = 7.0711 \cdot 10^{-5}$, $e_y = -7.0711 \cdot 10^{-5}$, $h_x = h_y = 0$ and $\lambda_\theta = 315^\circ$ (λ_θ arbitrarily chosen).

The variation of its Keplerian elements are shown in the following figures, being $a_0 = 42164.14 \text{ km}$, $e_0 = 0.0001$ and $i_0 = 0^\circ$.

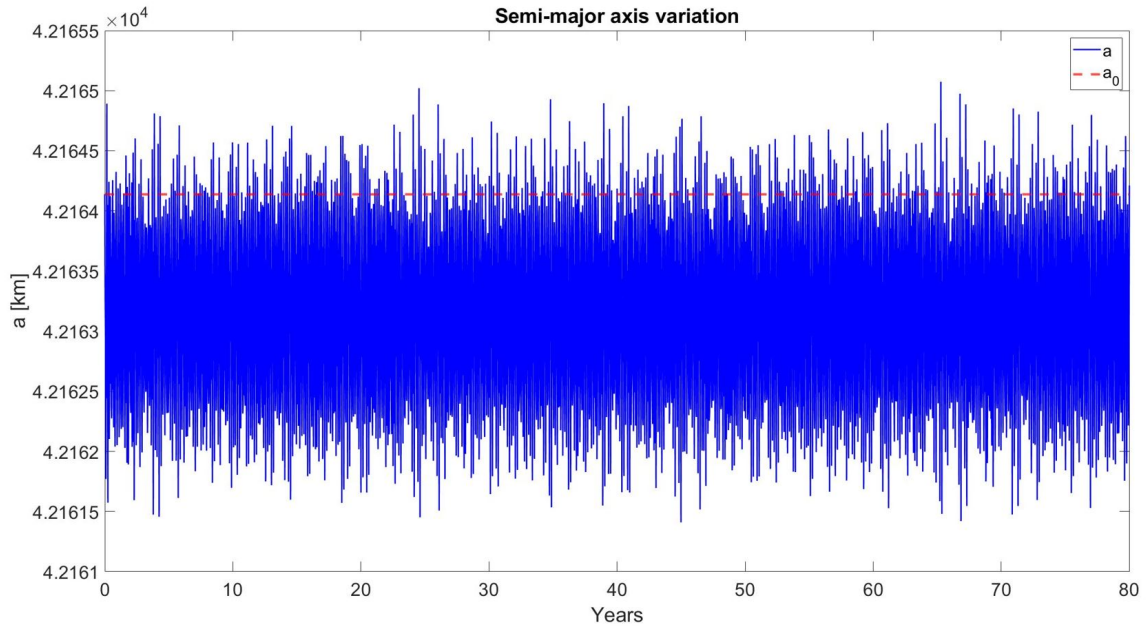


Figure 3.6 Variation of the semi-major axis of a GEO due to Luni-Solar perturbation.

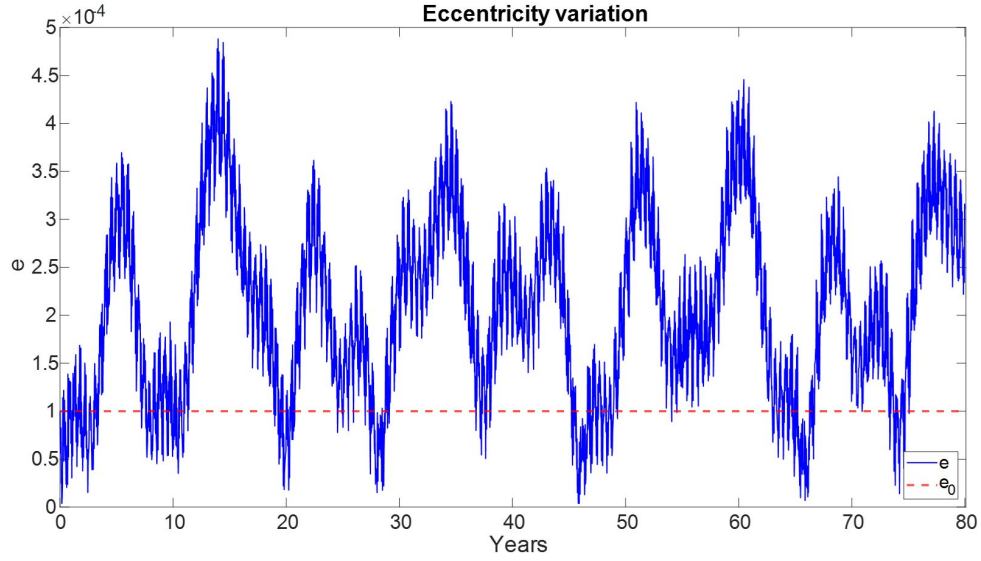


Figure 3.7 Variation of the eccentricity of a GEO due to Luni-Solar perturbation.

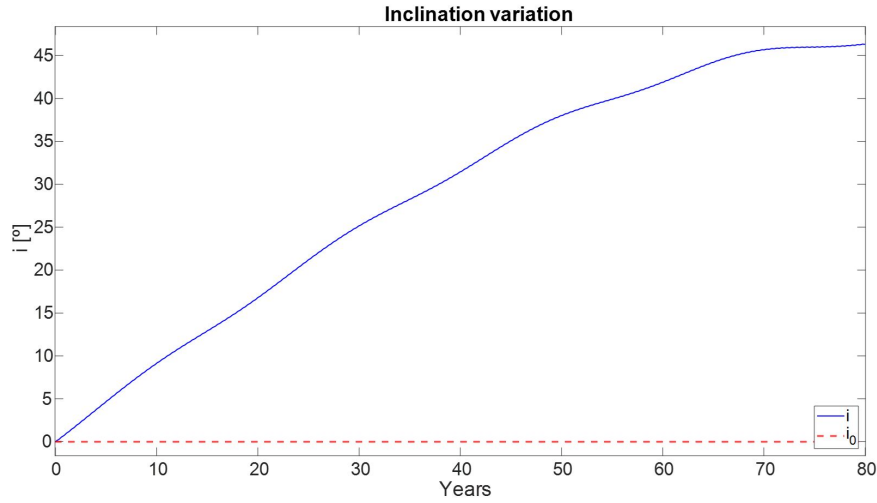


Figure 3.8 Variation of the inclination angle of a GEO due to Luni-Solar perturbation.

Note that, as mentioned in Table 2.1, third body perturbations for a , e and i are periodic. Nevertheless, due to the low magnitude of Luni-Solar perturbation, inclination angle tends to increase during the whole study, reaching at the eightieth year its maximum value. Thus, the period of the inclination in GEO for Luni-Solar perturbation is 320 years. This period is even longer in LEO, due to the reduction of Luni-Solar acceleration with respect to the Keplerian acceleration, as we discussed in 2.2.3. The long period in the variation of the inclination (as well as of the eccentricity) is, as mentioned in [22], due to the 18.6-year rotation of the Moon's orbital plane about the ecliptic, which is the same effect that produces the nutation of Earth's axis. As the time required to perform these computations is extreme (10 hours to compute the 80-year variations of this GEO), in the following examples we show the variations during shorter periods of time.

To see how strong this perturbation is in the short term, we present a shorter analysis (30 days) in the following figures of the same satellite.

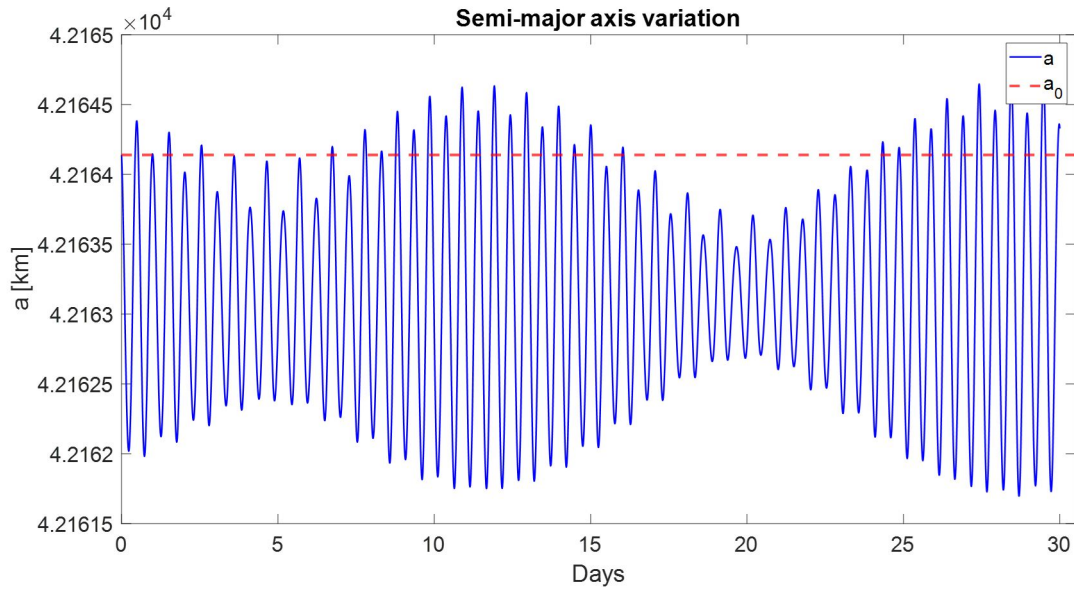


Figure 3.9 Shorter analysis of the variation of the semi-major axis of a GEO due to Luni-Solar perturbation.

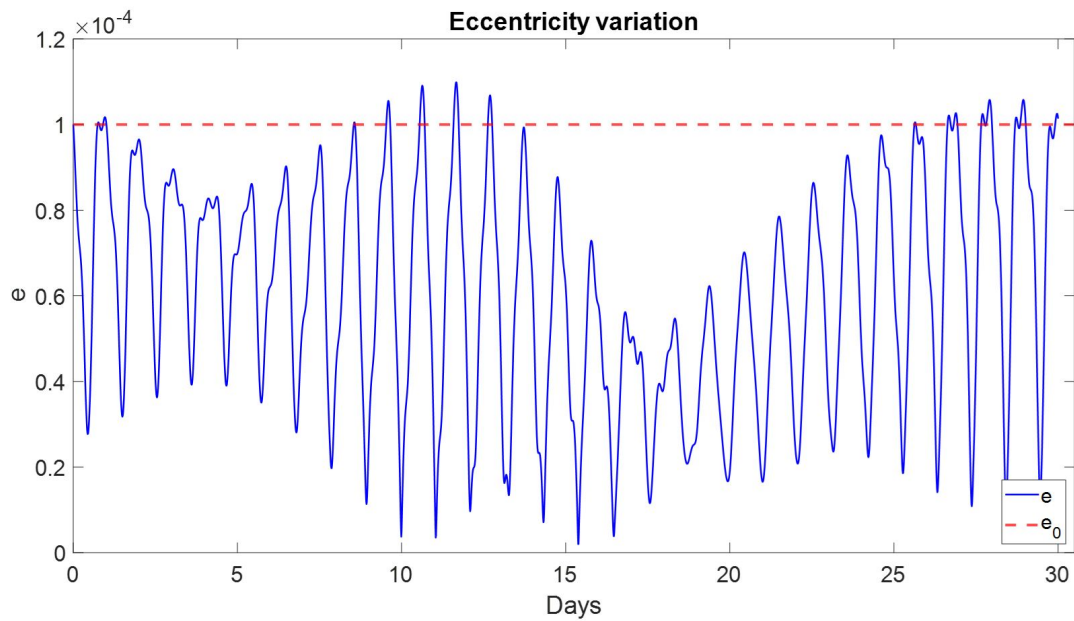


Figure 3.10 Shorter analysis of the variation of the eccentricity of a GEO due to Luni-Solar perturbation.

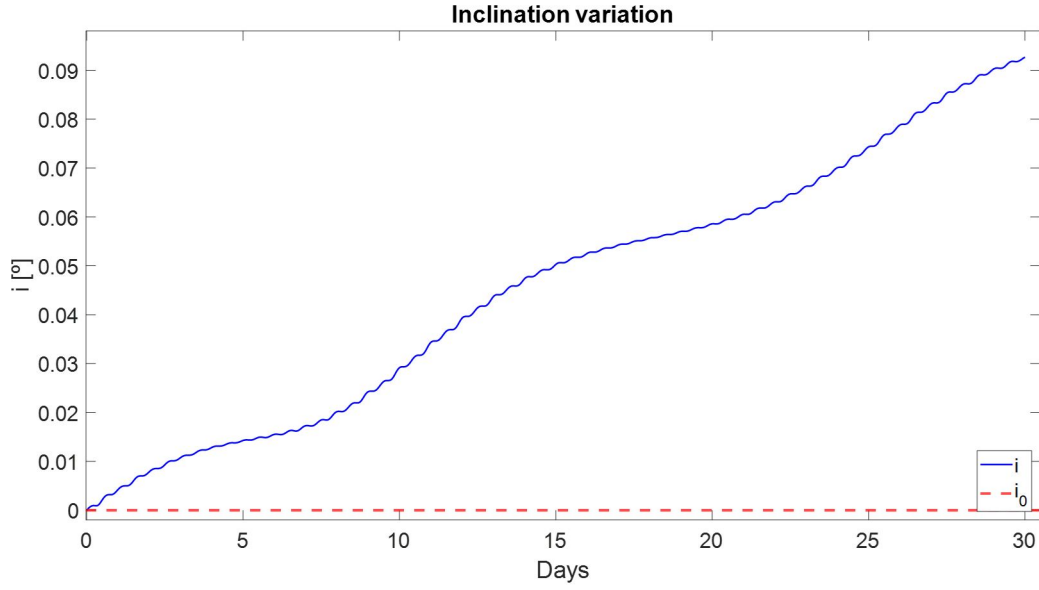


Figure 3.11 Shorter analysis of the variation of the inclination angle of a GEO due to Luni-Solar perturbation.

As we can observe, the Luni-Solar perturbation can deviate a GEO orbit dozens of metres in just a few days. Thus, considering this kind of perturbation is essential to precisely predict where a satellite will be after a few hours or days.

3.3.2 Low Earth Orbit satellite affected by the Sun and the Moon

In this case, a LEO satellite is studied, taking into account the Luni-Solar perturbation in a 30-year period. The Keplerian initial elements of the chosen satellite are $a = 6878.14 \text{ km}$, $e = 0.01$, $i = 20^\circ$, $\omega = 90^\circ$ and $\Omega = 45^\circ$.

The results are presented in the following figures:

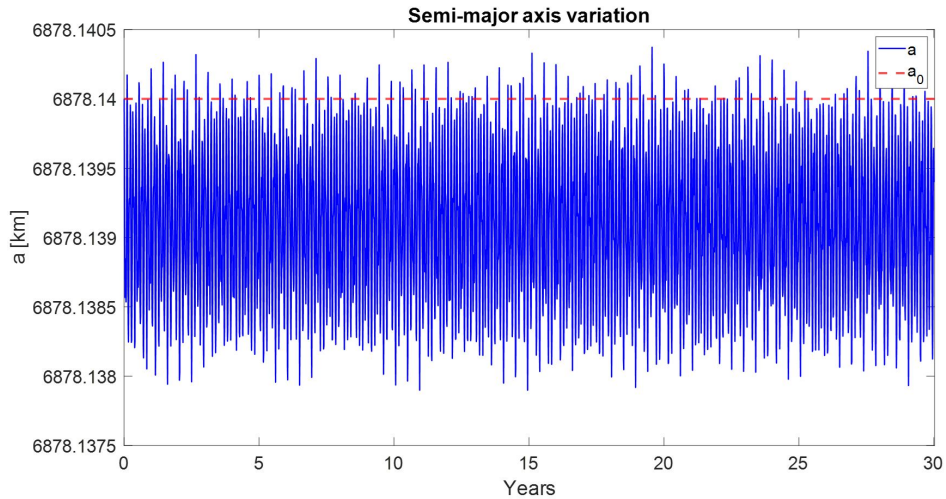


Figure 3.12 Variation of the semi-major axis of a LEO due to Luni-Solar perturbation.

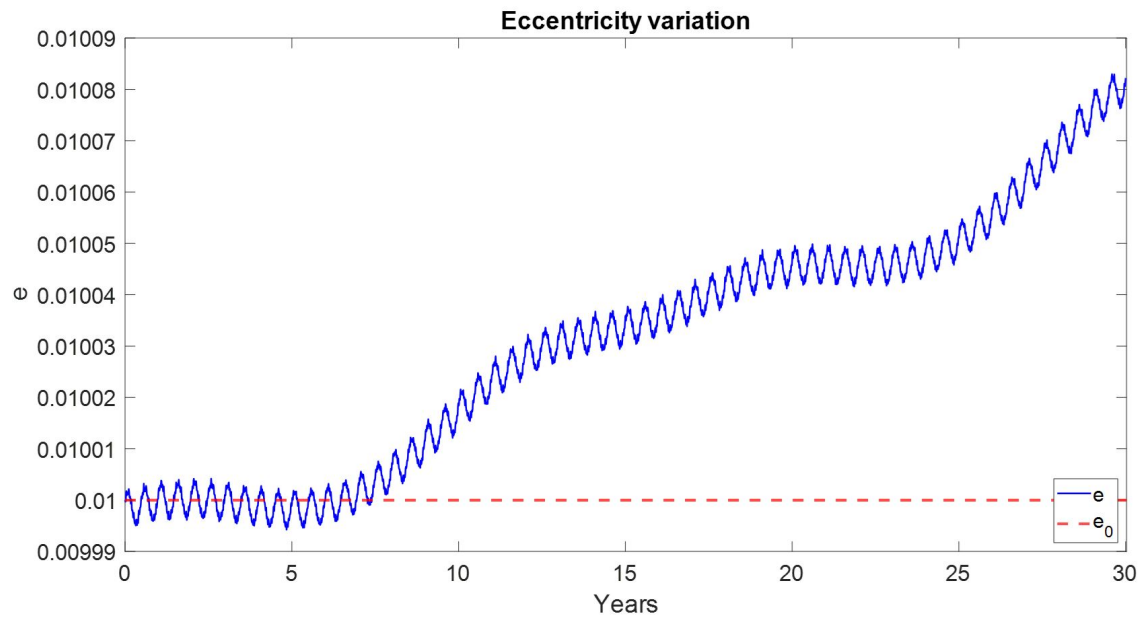


Figure 3.13 Variation of the eccentricity of a LEO due to Luni-Solar perturbation.

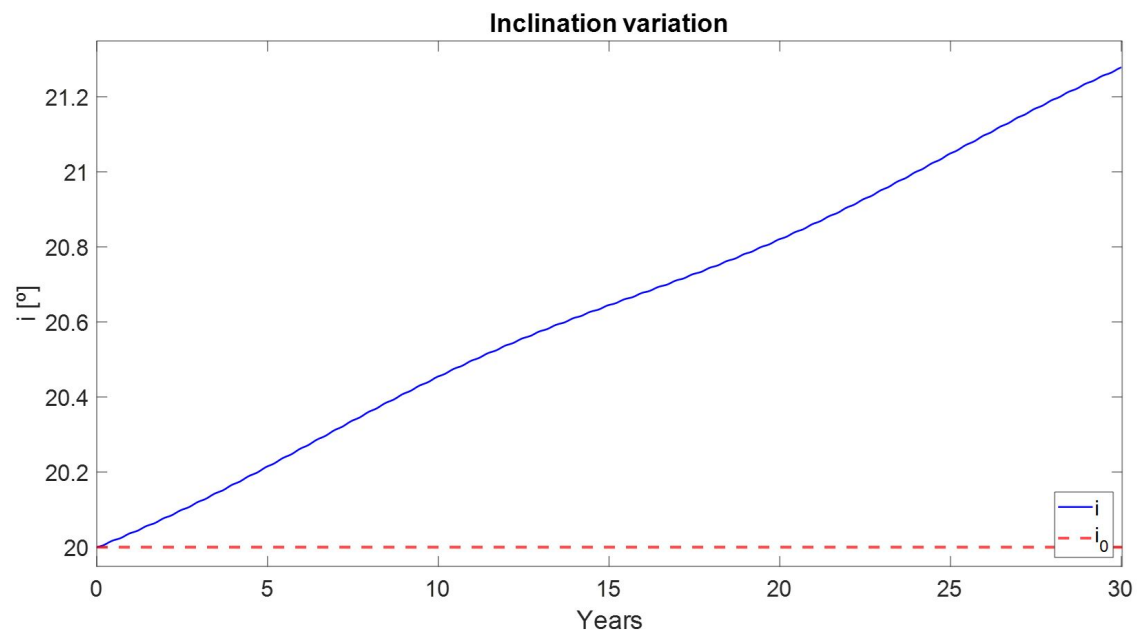


Figure 3.14 Variation of the inclination of a LEO due to Luni-Solar perturbation.

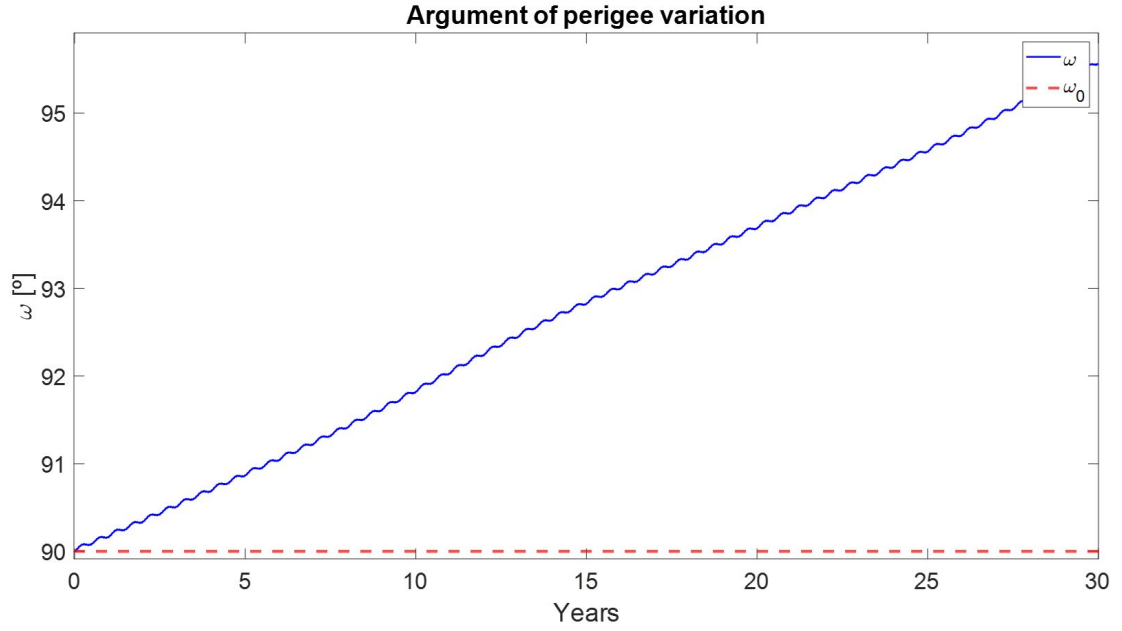


Figure 3.15 Variation of the argument of the perigee of a LEO due to Luni-Solar perturbation.

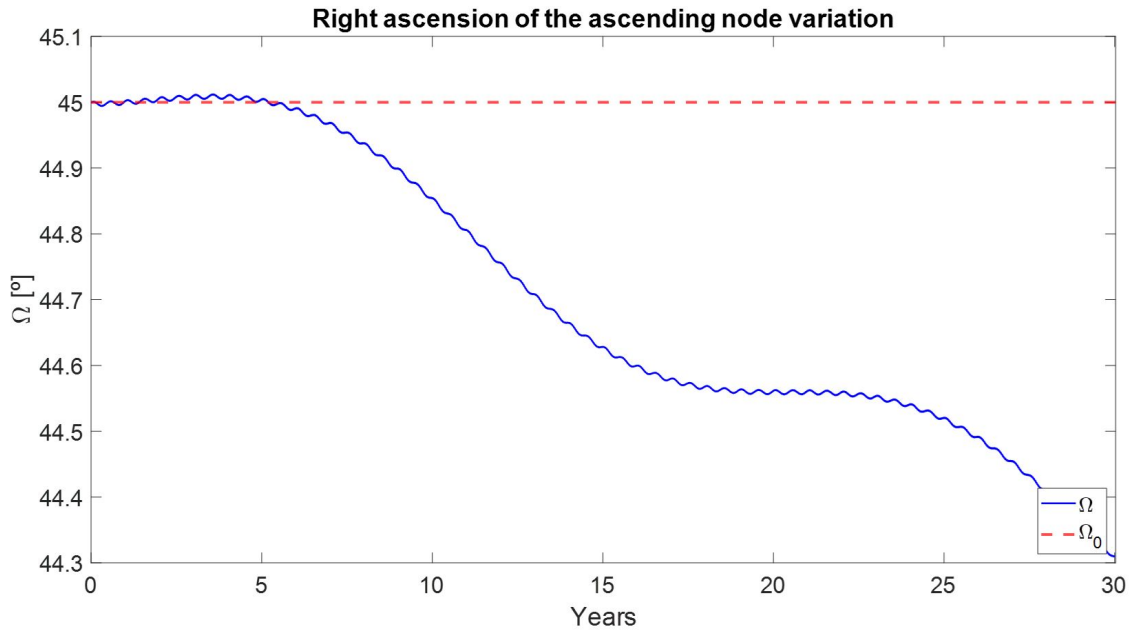


Figure 3.16 Variation of the RAAN of a LEO due to Luni-Solar perturbation.

As predicted in Table 2.1, ω and Ω variations due to third-body perturbations are a combination of secular and periodic variations. On the other hand, we clearly see that eccentricity and inclination tend to increase during the 30-year period as their period is longer than the time simulated. This is, as we mentioned in Section 3.3.1, due to the motions of the Moon's perigee.

It is interesting to compare the deviations of the orbital elements due to the Luni-Solar perturbation when we vary the inclination of the orbit. Therefore, the following figures are presented to compare, in the short term (30 days), how inclination affects.

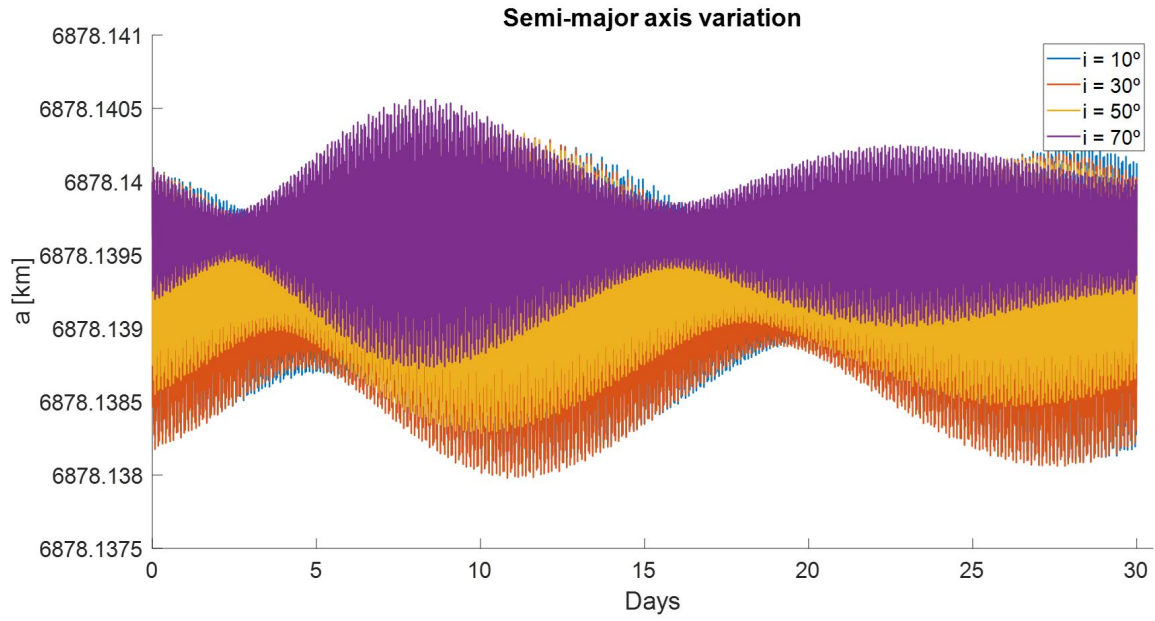


Figure 3.17 Variation of the semi-major axis of a LEO due to Luni-Solar perturbation for different inclinations.

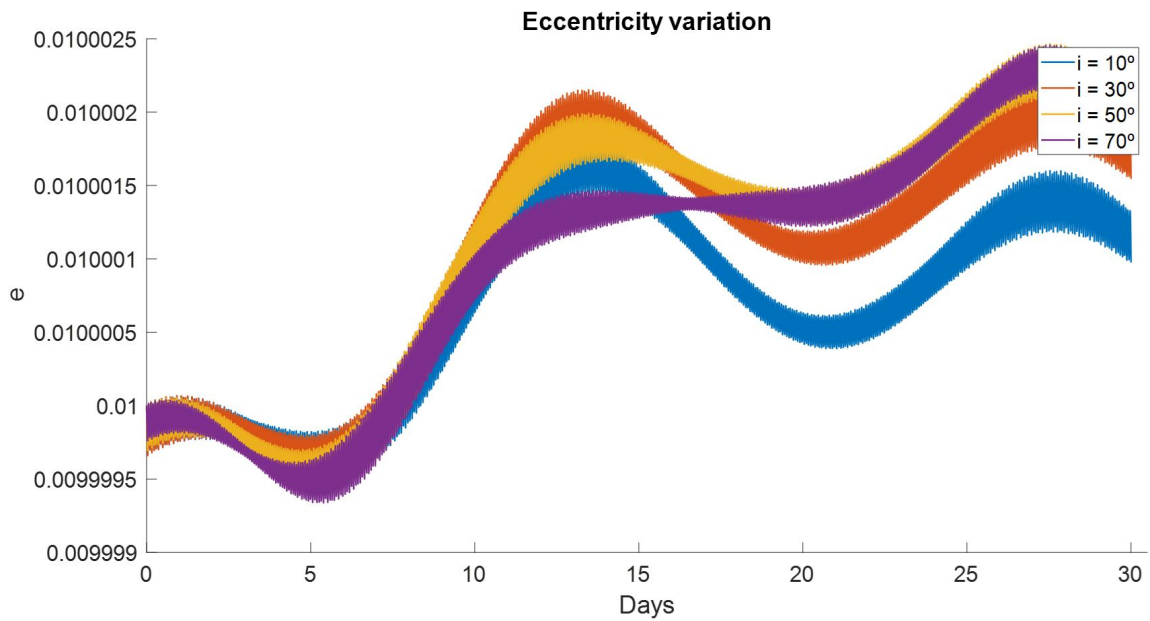


Figure 3.18 Variation of the eccentricity of a LEO due to Luni-Solar perturbation for different inclinations.

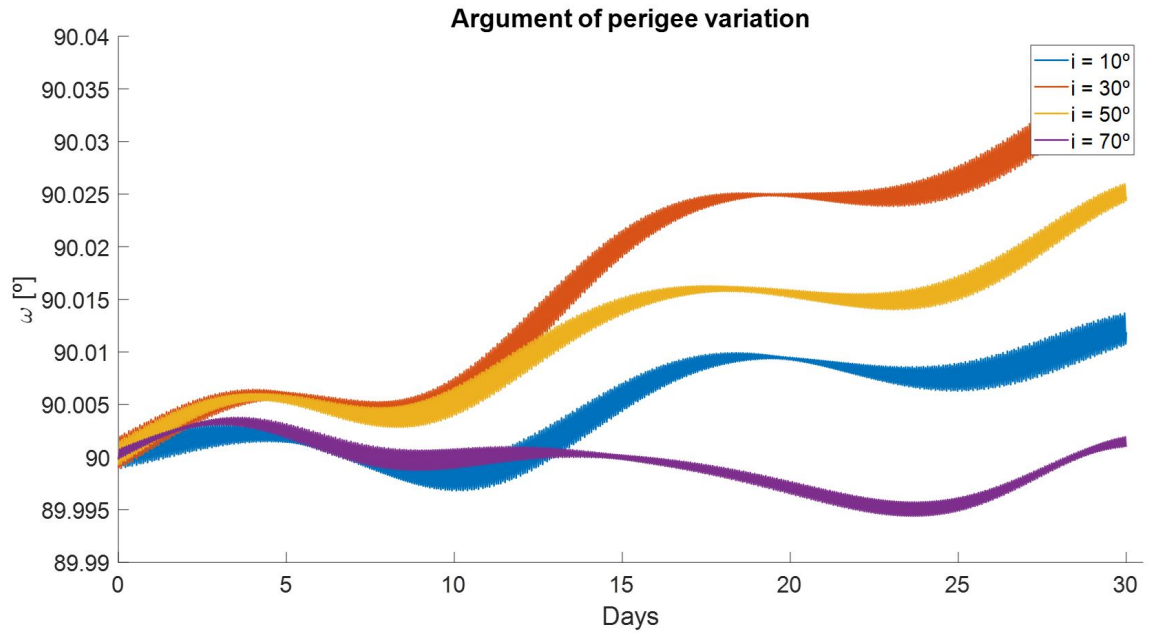


Figure 3.19 Variation of the argument of the perigee of a LEO due to Luni-Solar perturbation for different inclinations.

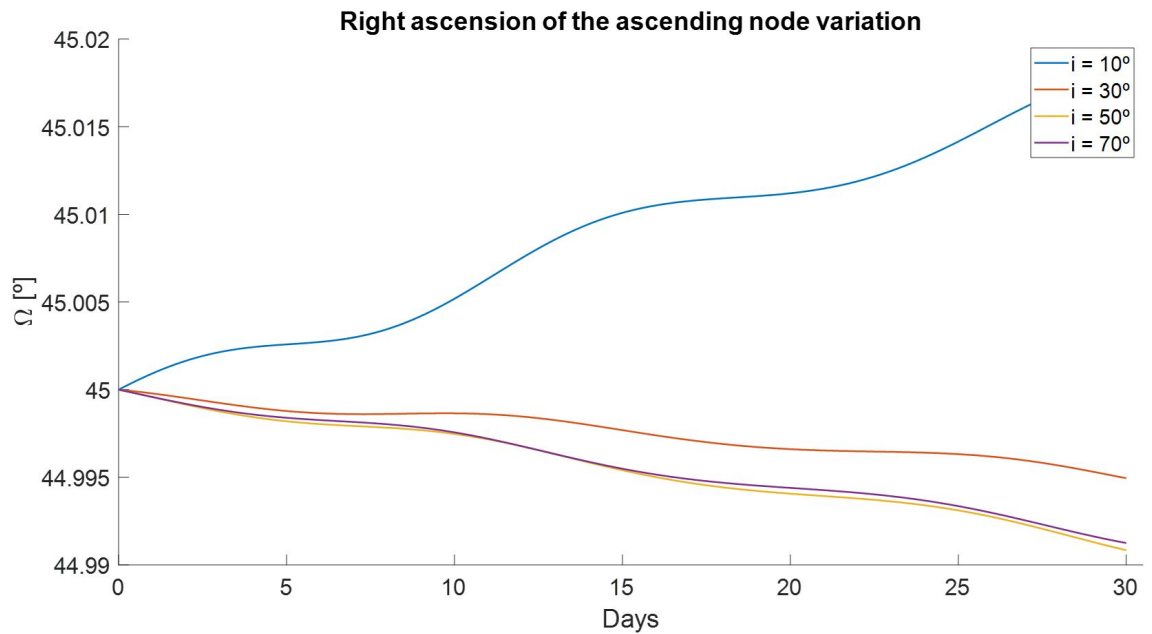


Figure 3.20 Variation of the RAAN of a LEO due to Luni-Solar perturbation for different inclinations.

These results show how influential the inclination of the orbit is in the variations of the orbital elements.

3.3.3 GEO satellite affected by J_2 perturbation

In this section we bring under study J_2 perturbation affecting a GEO in a 30-year period. We will consider the same GEO as in Section 3.3.1. The variations due to J_2 are presented in the figures below.

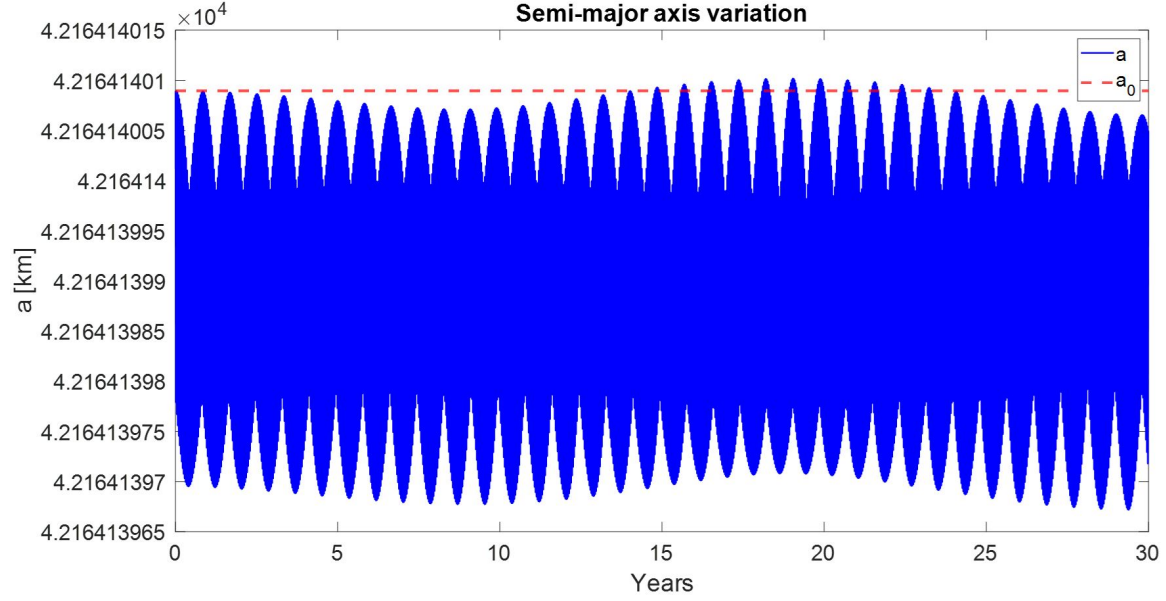


Figure 3.21 Variation of the semi-major axis of a GEO due to J_2 perturbation.

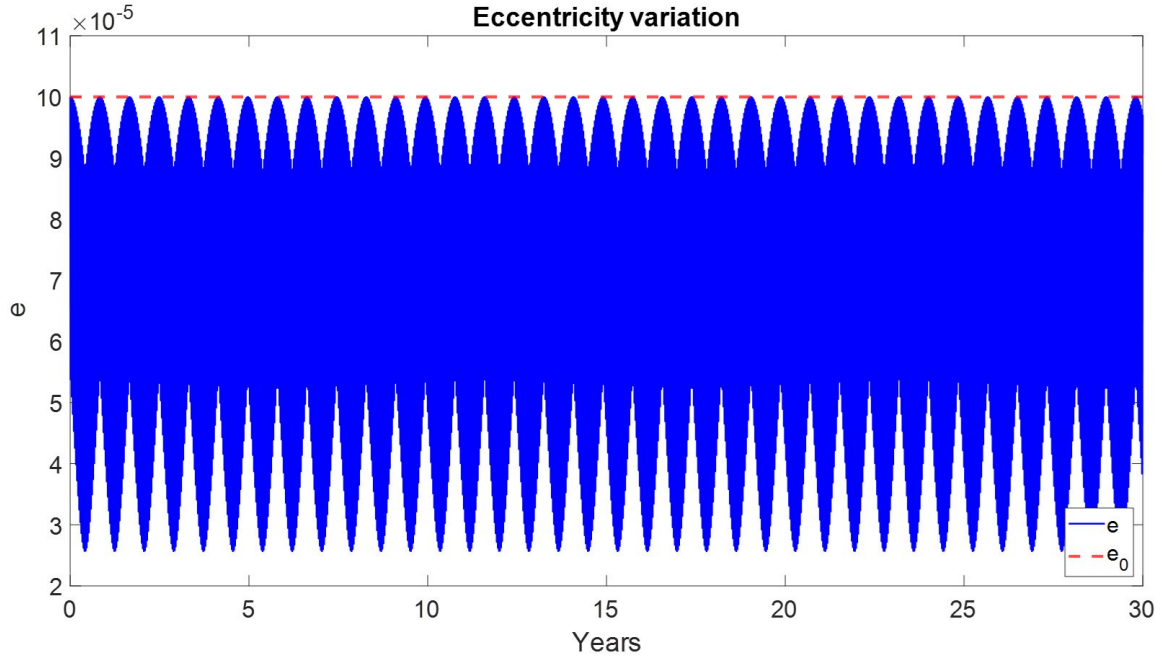


Figure 3.22 Variation of the eccentricity of a GEO due to J_2 perturbation.

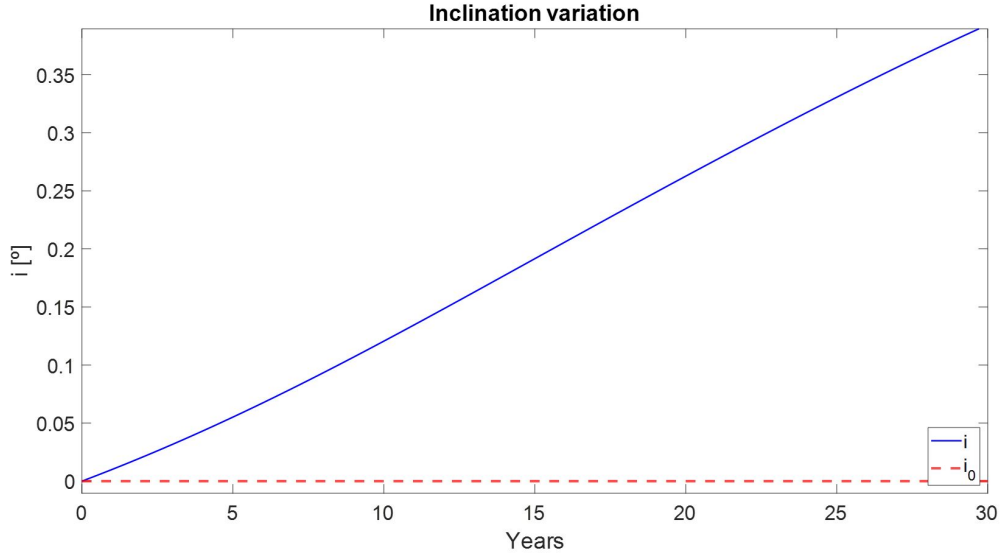


Figure 3.23 Variation of the inclination of a GEO due to J_2 perturbation.

As we expected, the variations of a , e and i are periodic. However, as for the Luni-Solar perturbation, the inclination has a period of more than 30 years. As described in [22], long-periodic effects from zonal harmonics have a fundamental period of $2\pi/\dot{\omega}$, depending $\dot{\omega}$ on the inclination:

$$\dot{\omega} = \frac{3nR_{\oplus}^2 J_2}{4p^2} \{4 - 5\sin^2(i)\}. \quad (3.1)$$

As we did for the Luni-Solar perturbation, we present a shorter analysis of 30 days to see the influence of the J_2 in short propagations.

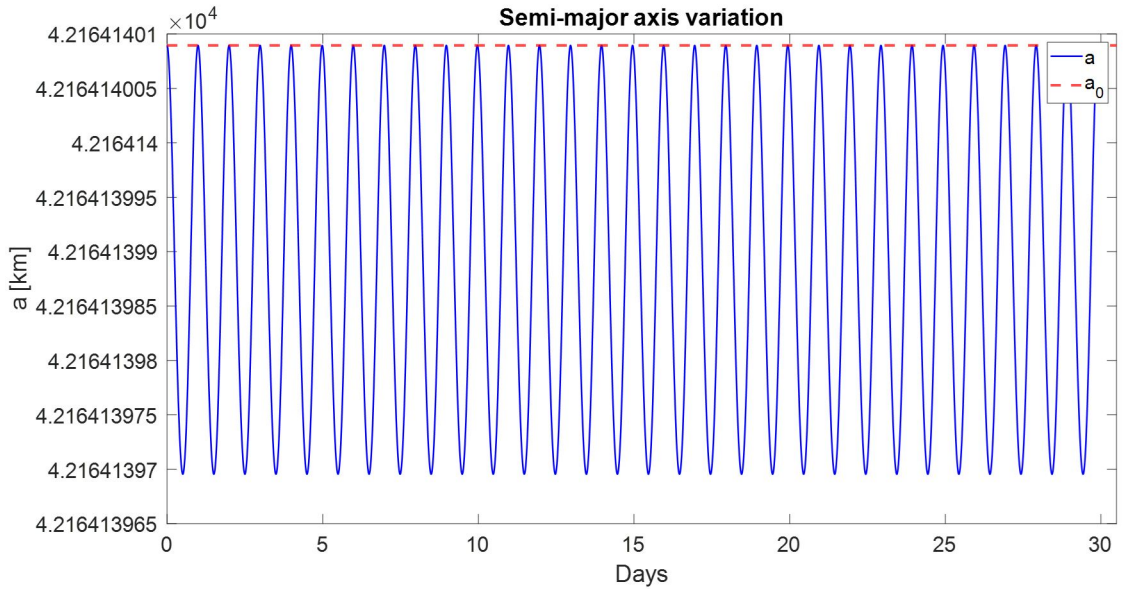


Figure 3.24 Shorter analysis of the variation of the semi-major axis of a GEO due to J_2 perturbation.

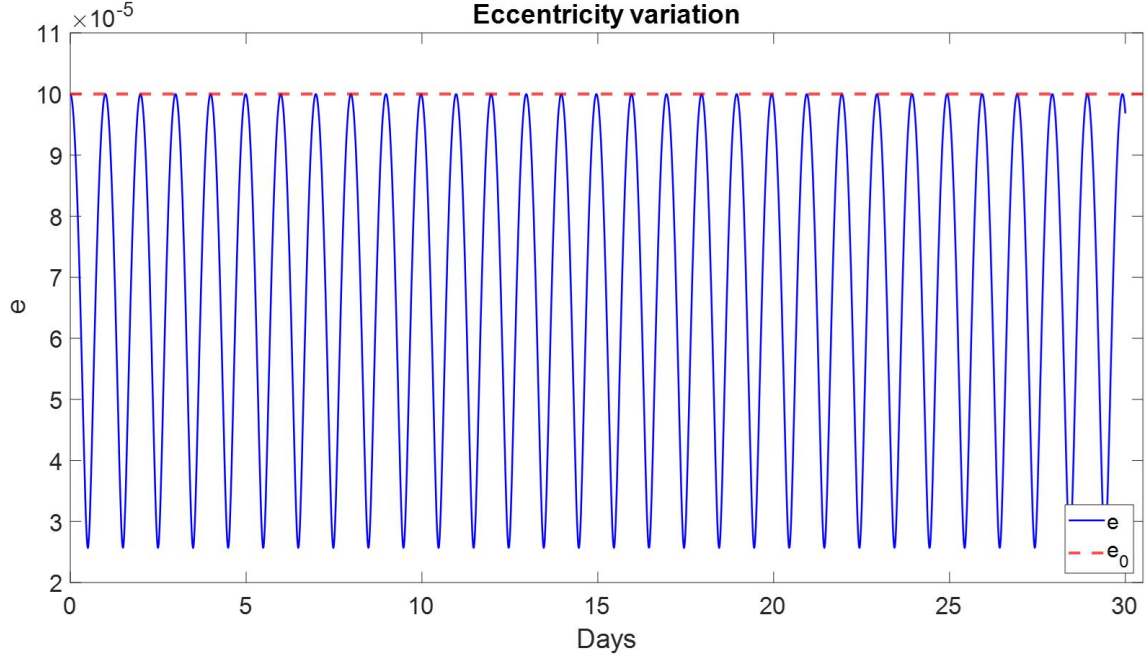


Figure 3.25 Shorter analysis of the variation of the eccentricity of a GEO due to J_2 perturbation.

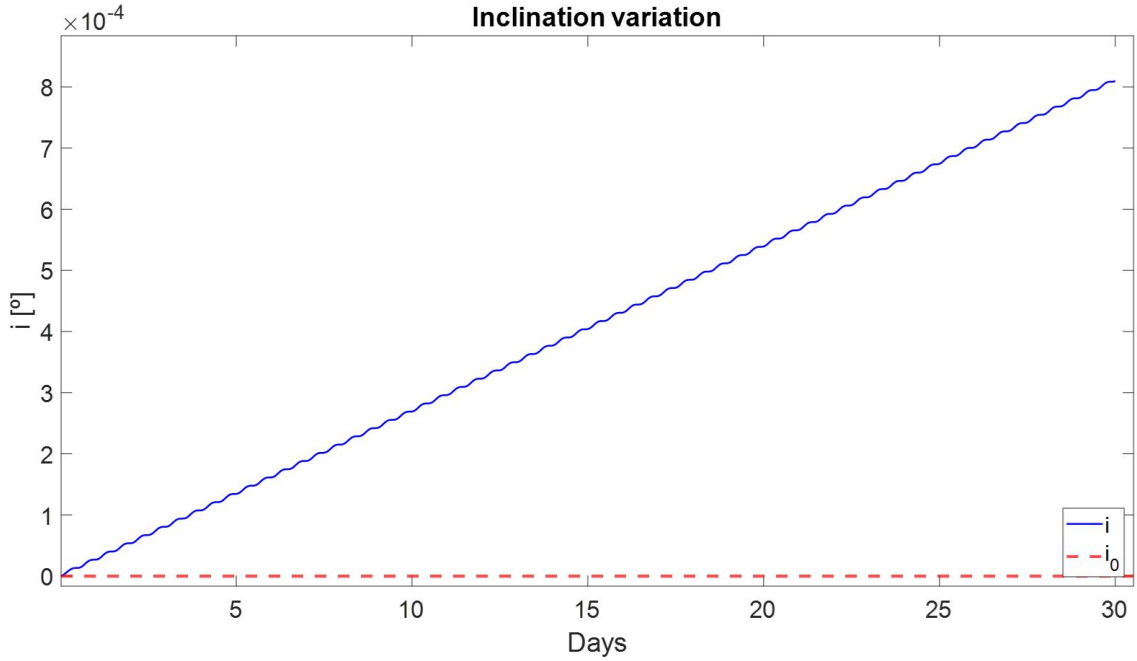


Figure 3.26 Shorter analysis of the variation of the inclination angle of a GEO due to J_2 perturbation.

3.3.4 Low Earth Orbit satellite affected by J_2 perturbation

In this case, a LEO satellite affected by J_2 perturbation is studied in a 30-year period. The Keplerian initial elements of the chosen satellite are $a = 6878.14 \text{ km}$, $e = 0.01$, $i = 20^\circ$, $\omega = 90^\circ$ and $\Omega = 45^\circ$ (the same as the previous LEO studied).

The results are presented in the following figures:

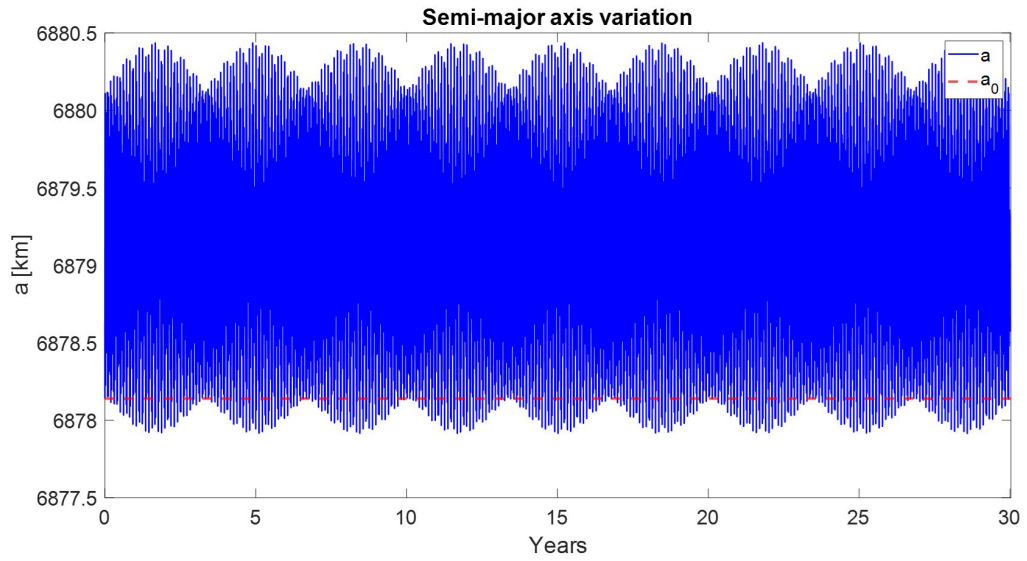


Figure 3.27 Variation of the semi-major axis of a LEO due to J_2 perturbation.

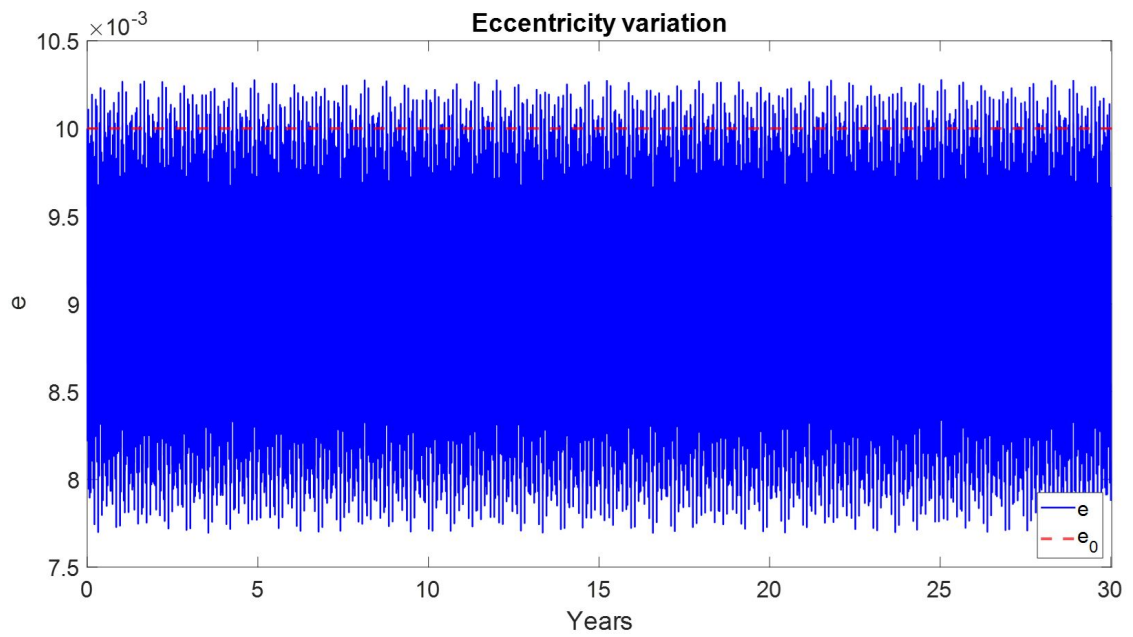


Figure 3.28 Variation of the eccentricity of a LEO due to J_2 perturbation.

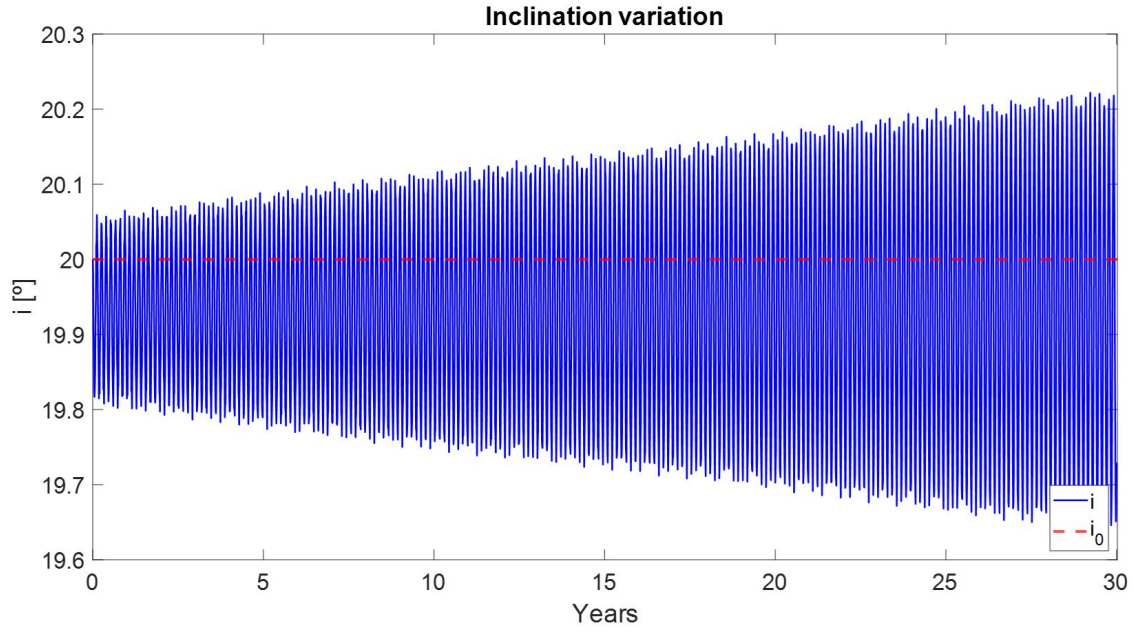


Figure 3.29 Variation of the inclination of a LEO due to J_2 perturbation.

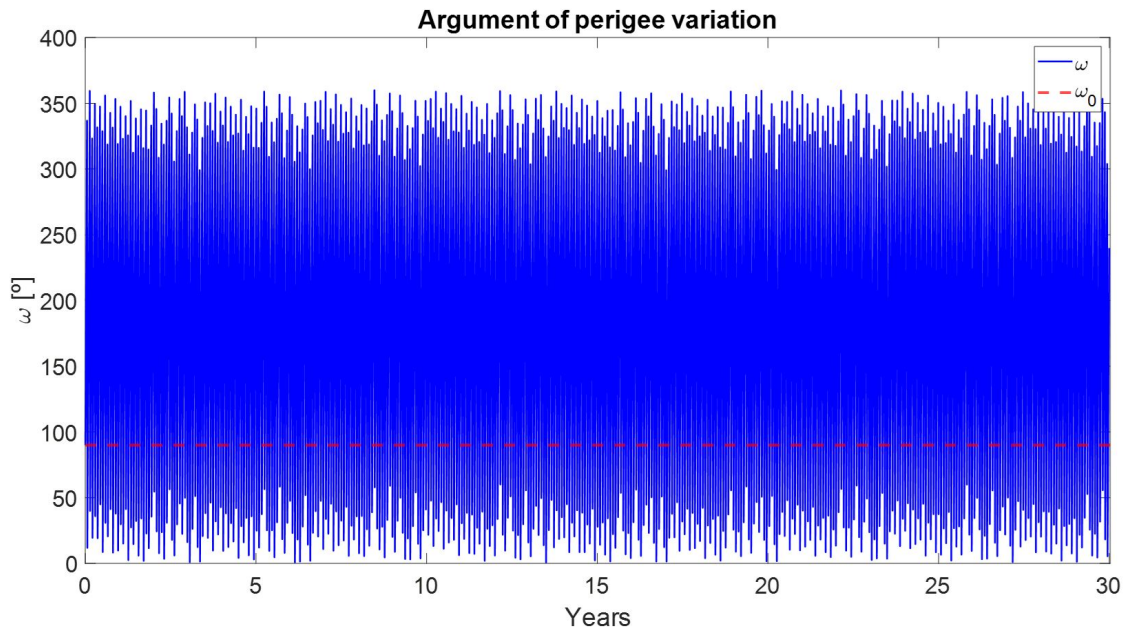


Figure 3.30 Variation of the argument of the perigee of a LEO due to J_2 perturbation.

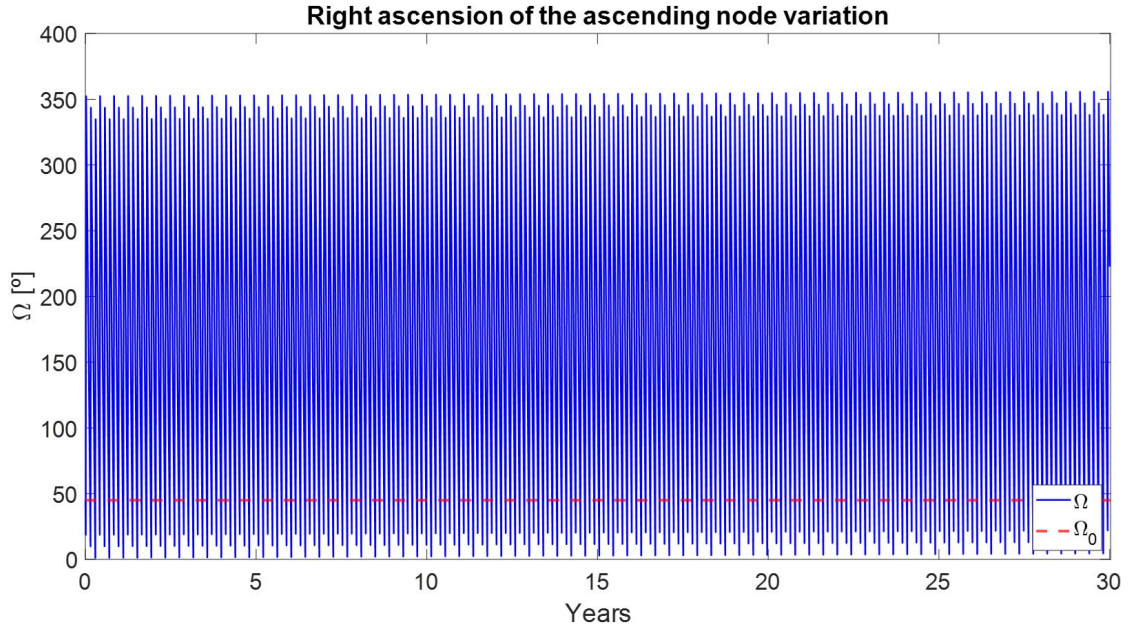


Figure 3.31 Variation of the RAAN of a LEO due to J_2 perturbation.

This case of study shows another kind of period appearing due to the zonal harmonics. The long periodic/short periodic beat period [22] is caused by the interactions of short-periodic and long-periodic variations, creating a high-frequency oscillations with an amplitude that oscillates at the long-periodic frequency. This is the case of the inclination, which tends to increase its amplitude during the hole study as the long-periodic frequency is greater than the 30-year period studied. This effect is shown in Figure 3.32.

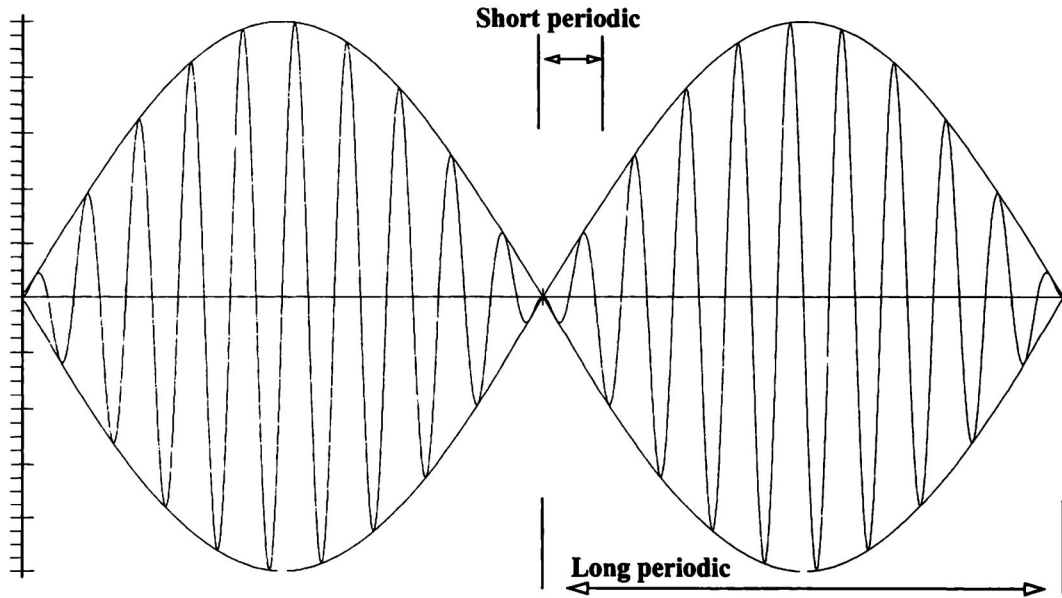


Figure 3.32 Long periodic/short periodic beat period from zonal harmonics [22].

To deepen this analysis we present the same study we did for the Luni-Solar perturbation affecting LEO satellites, This is, varying the inclination of the orbit to see its influence in short-term propagations (30 days).

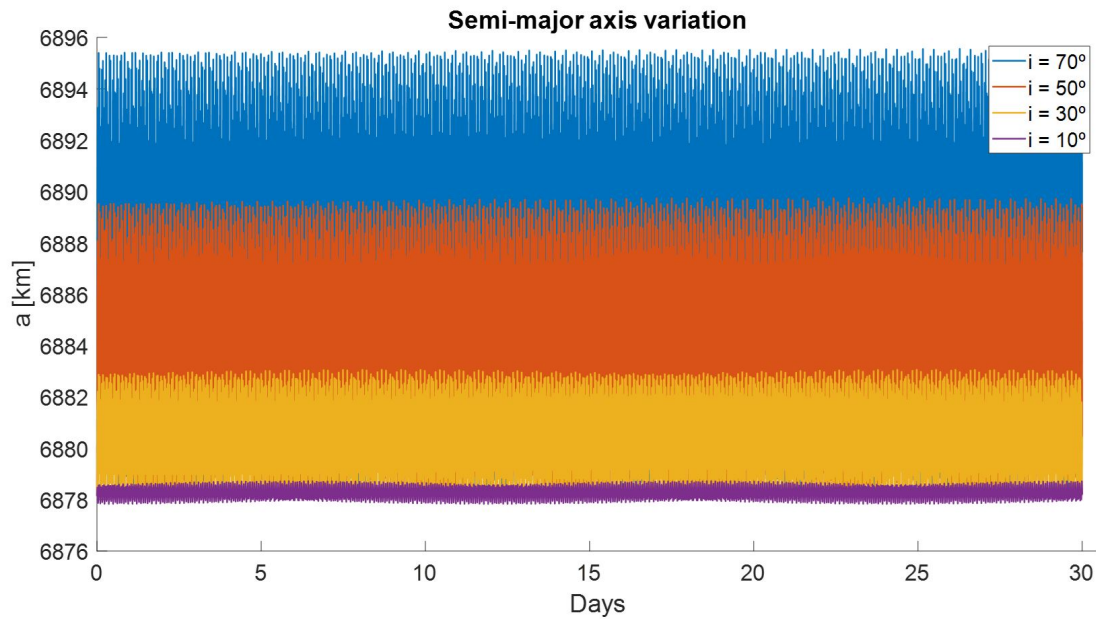


Figure 3.33 Variation of the semi-major axis of a LEO due to J_2 perturbation for different inclinations.

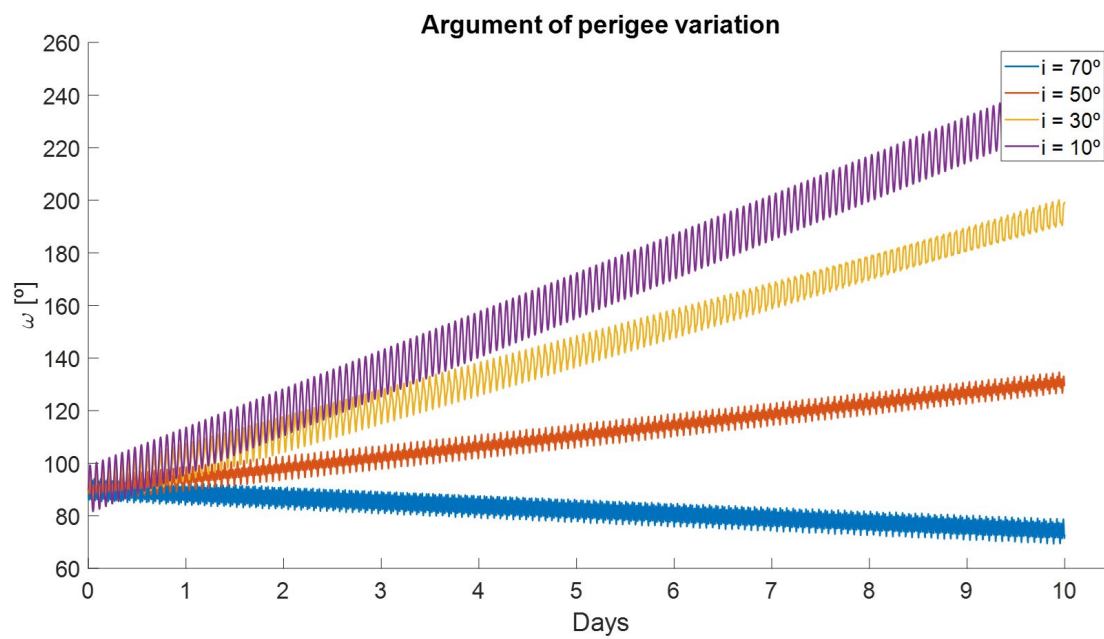


Figure 3.34 Variation of the argument of the perigee of a LEO due to J_2 perturbation for different inclinations.

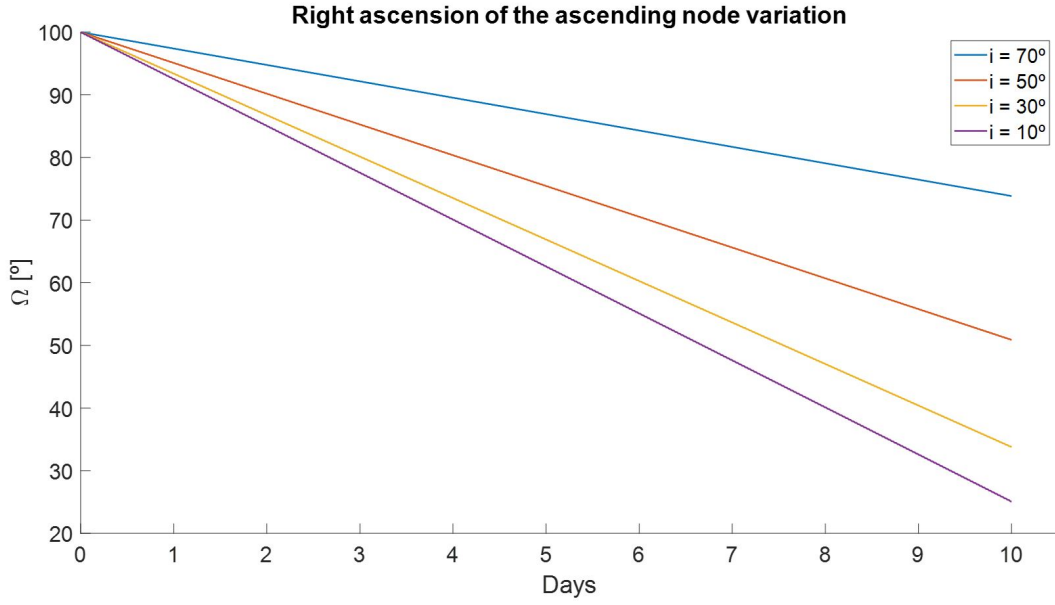


Figure 3.35 Variation of the RAAN of a LEO due to J_2 perturbation for different inclinations.

We see that reducing the inclination of the orbit increase the variation rate of ω and Ω , but reduces the variations in the semi-major axis.

3.3.5 Low Earth Orbit satellite affected by atmospheric drag

A LEO satellite affected by atmospheric drag is taken into consideration in a 30-day period. The initial Keplerian elements of the chosen satellite are $a = 6778.14 \text{ km}$, $e = 0.01$, $i = 20^\circ$, $\omega = 90^\circ$ and $\Omega = 45^\circ$, having reduced 100 km the semi-major axis with respect to previous LEO in order to increase the atmospheric drag effect.

The results are presented in the following figures:

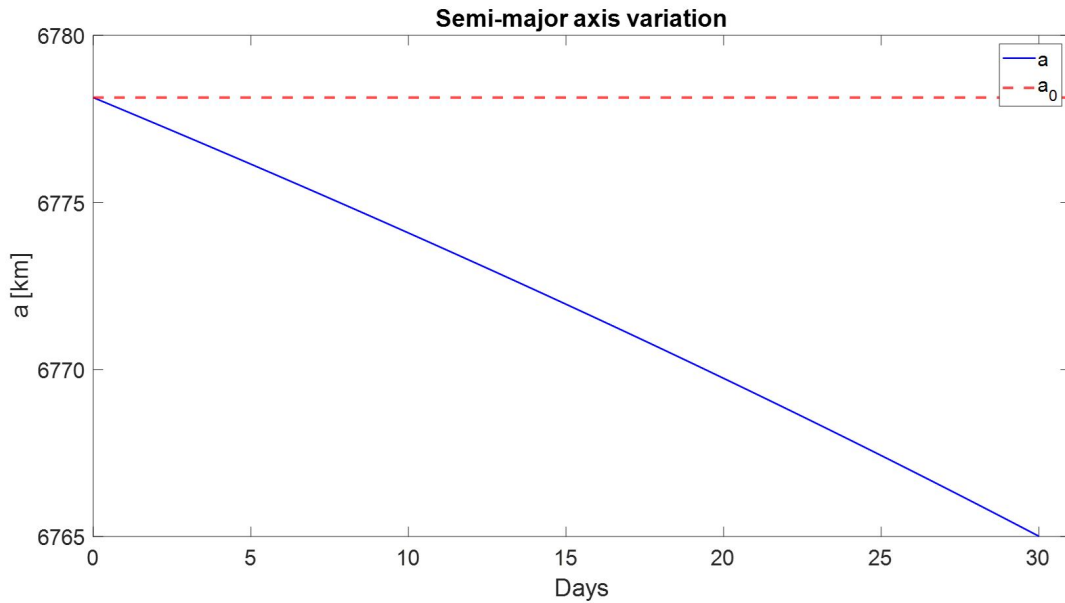


Figure 3.36 Variation of the semi-major axis of a LEO due to atmospheric drag.

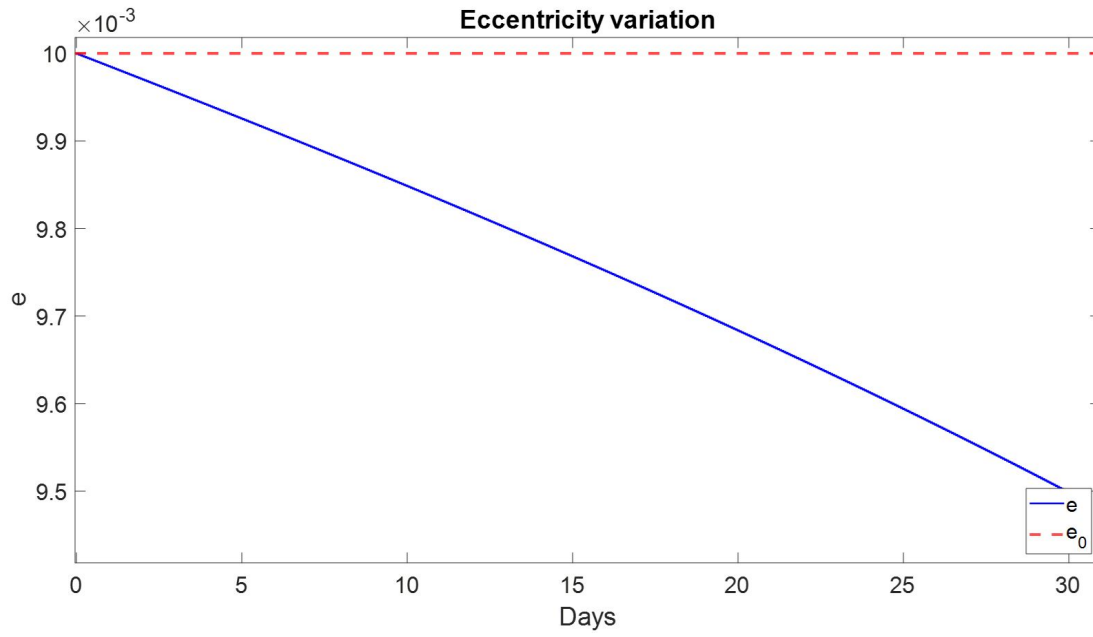


Figure 3.37 Variation of the eccentricity of a LEO due to atmospheric drag.

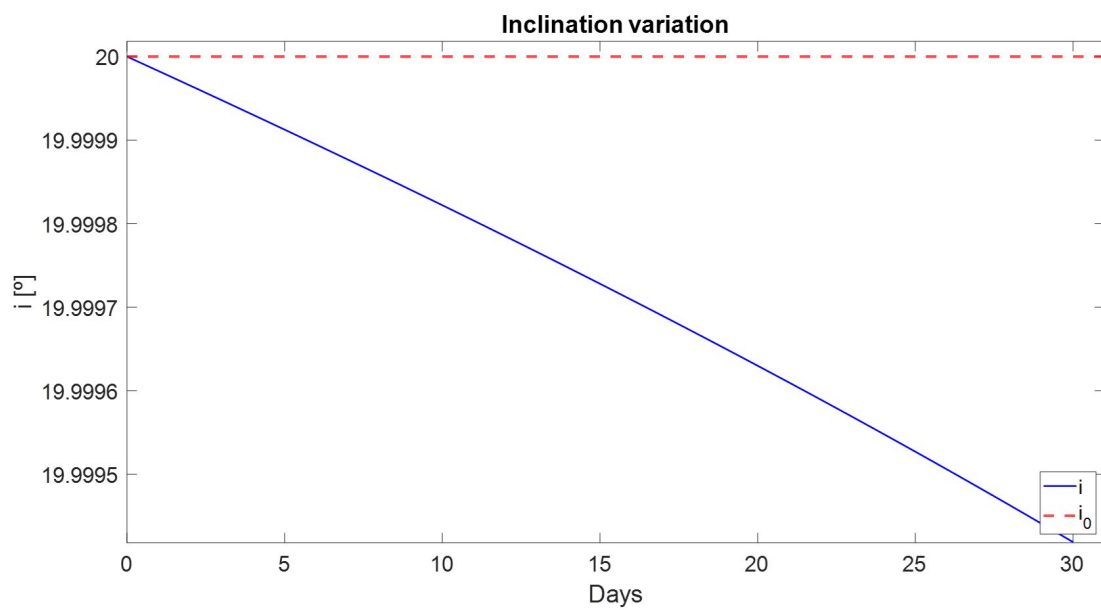


Figure 3.38 Variation of the inclination of a LEO due to atmospheric drag.

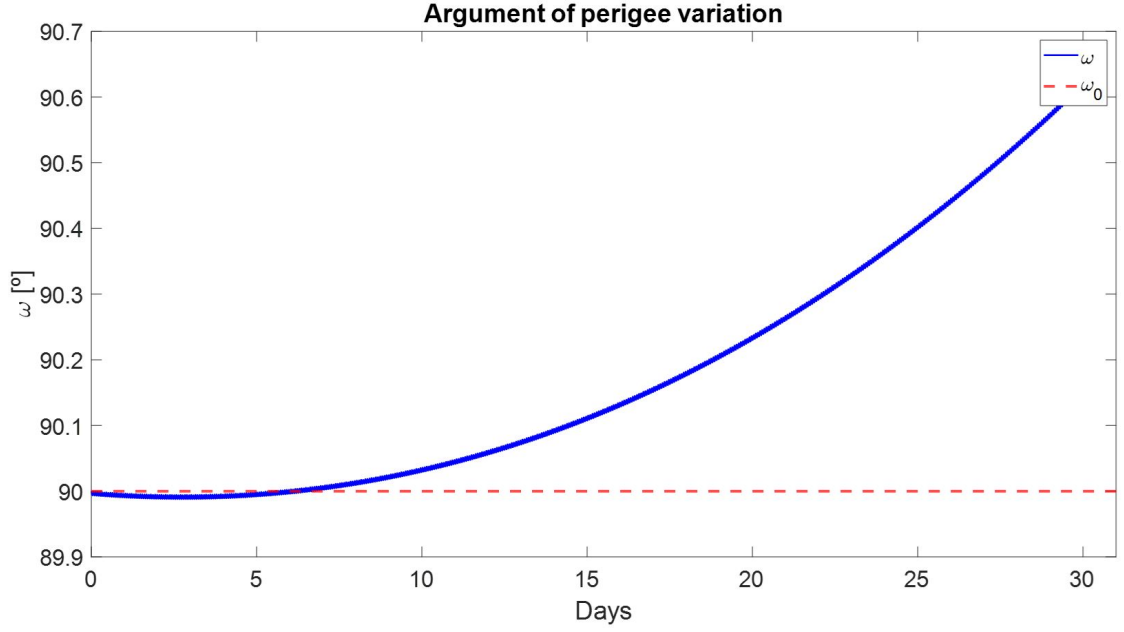


Figure 3.39 Variation of the argument of the perigee of a LEO due to atmospheric drag.

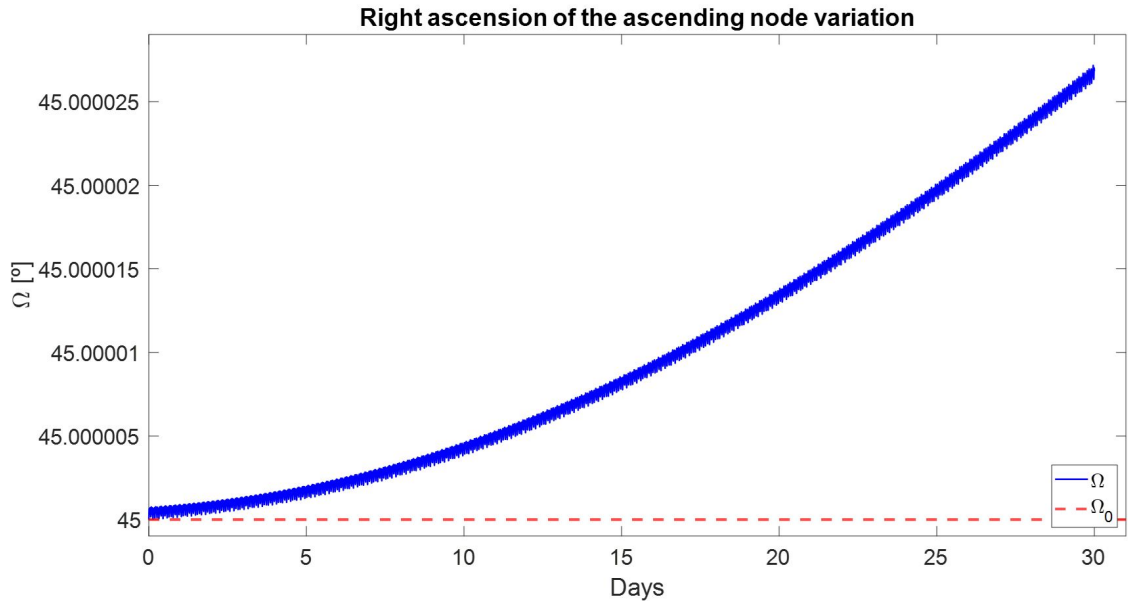


Figure 3.40 Variation of the RAAN of a LEO due to atmospheric drag.

Due to the short simulation time (the satellite collides with Earth's surface), ω and Ω just increase. Nevertheless, as predicted in Table 2.1, their variations due to atmospheric drag are periodic. On the other hand, we clearly see that a , e and i tend to decrease during the whole simulation until the satellite collides with Earth.

It is truly interesting to study how atmospheric drag grows exponentially the closer the satellite is to Earth. The following analysis is presented, showing the variation of the orbital elements of a satellite affected by atmospheric drag for different altitudes during 10 days.

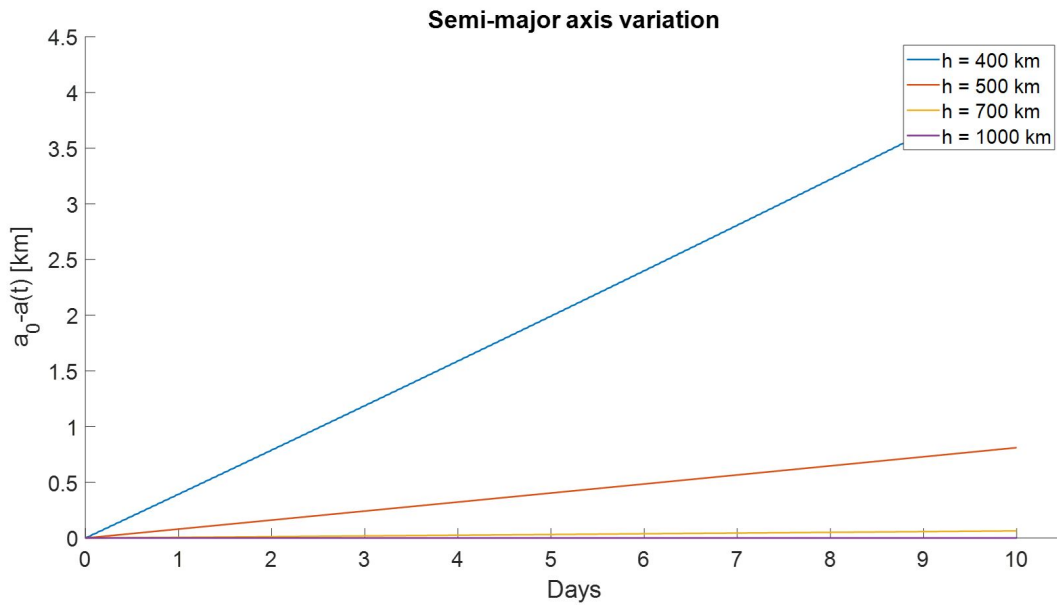


Figure 3.41 Influence of altitude in the variation of the semi-major axis of a LEO due to atmospheric drag.

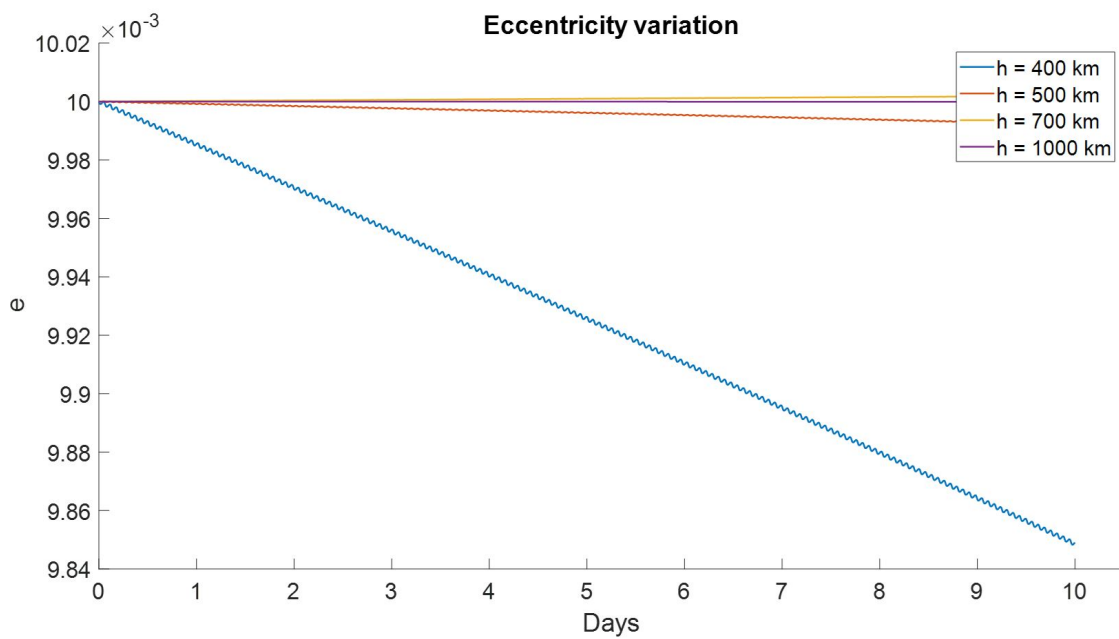


Figure 3.42 Influence of altitude in the variation of the eccentricity of a LEO due to atmospheric drag.

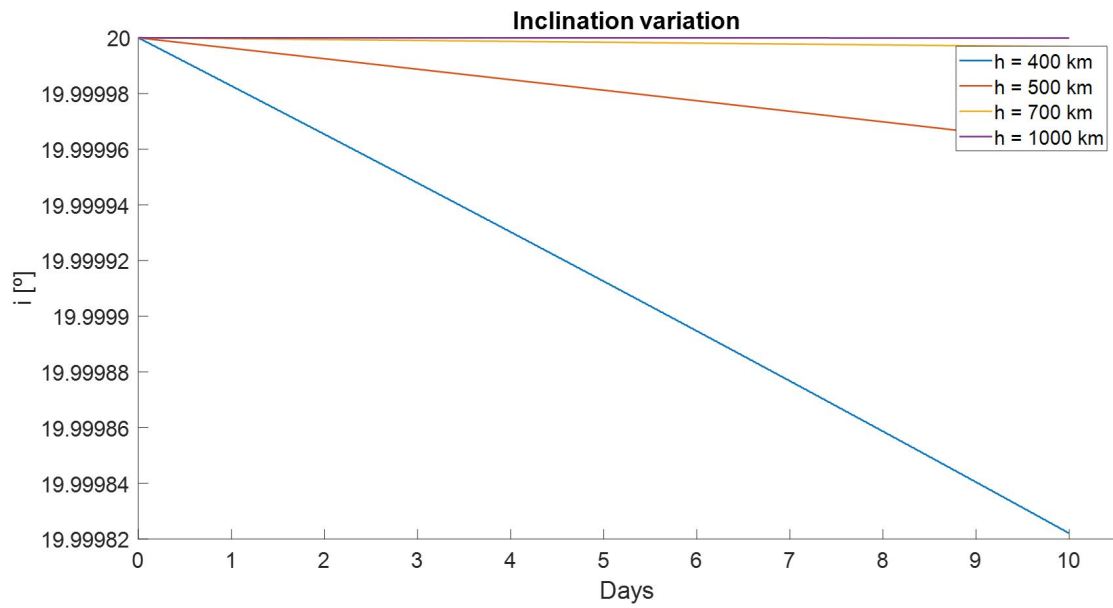


Figure 3.43 Influence of altitude in the variation of the inclination of a LEO due to atmospheric drag.

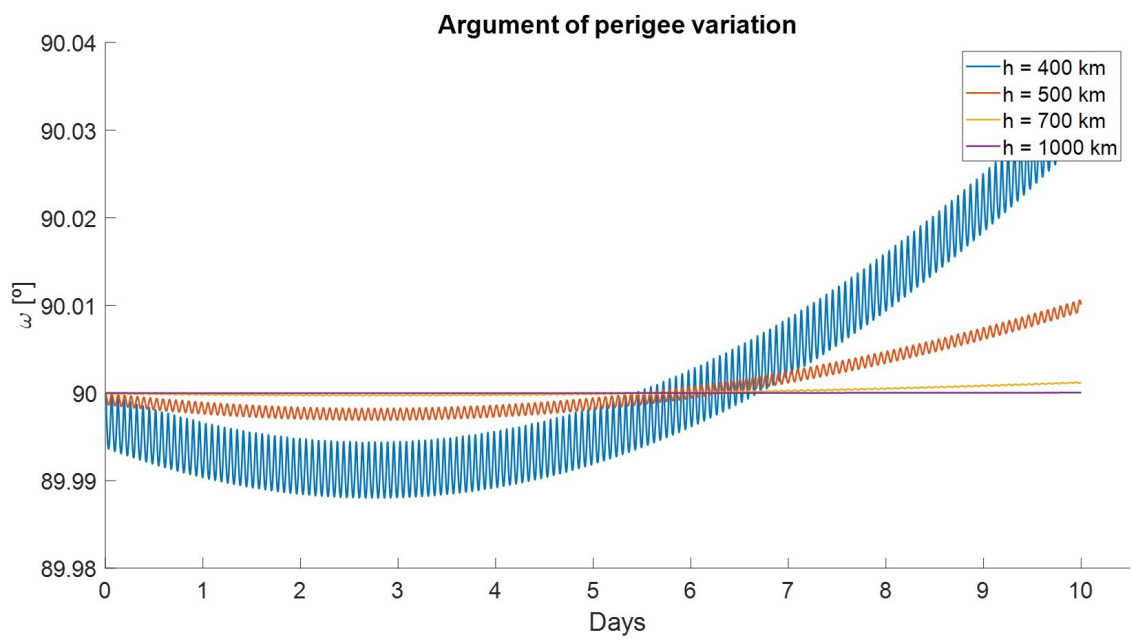


Figure 3.44 Influence of altitude in the variation of the argument of the perigee of a LEO due to atmospheric drag.

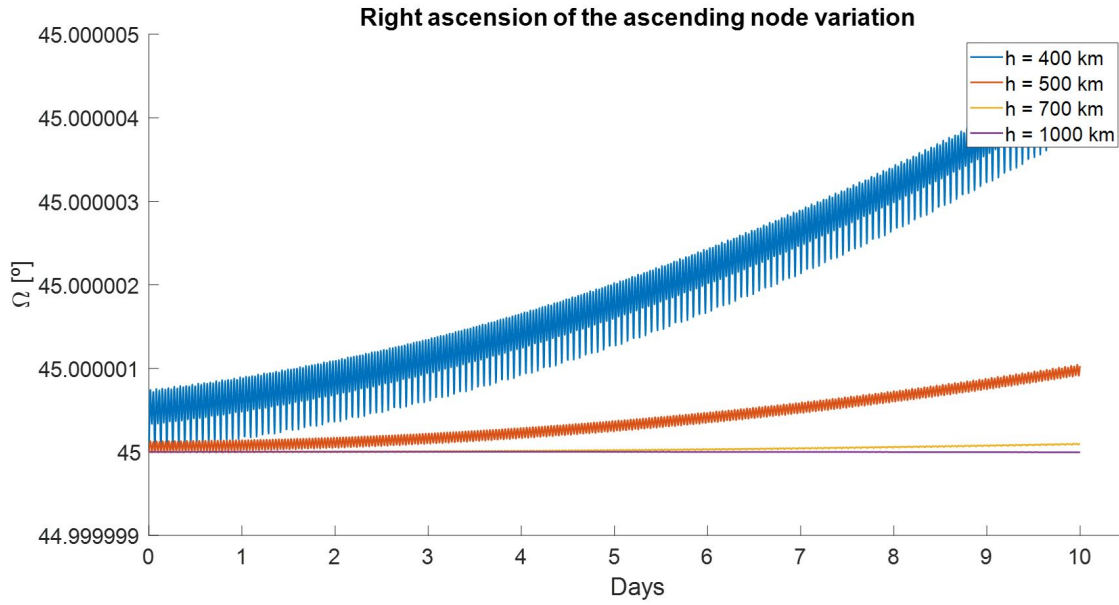


Figure 3.45 Influence of altitude in the variation of the RAAN of a LEO due to atmospheric drag.

As we might expect, the effects due to the atmospheric drag grow as we are closer to Earth.

3.3.6 GEO satellite affected by solar radiation pressure

In this section we bring under study solar-radiation pressure affecting a GEO in a one-year period. We will consider the same GEO as in Section 3.3.1. The variations are presented in the figures below.

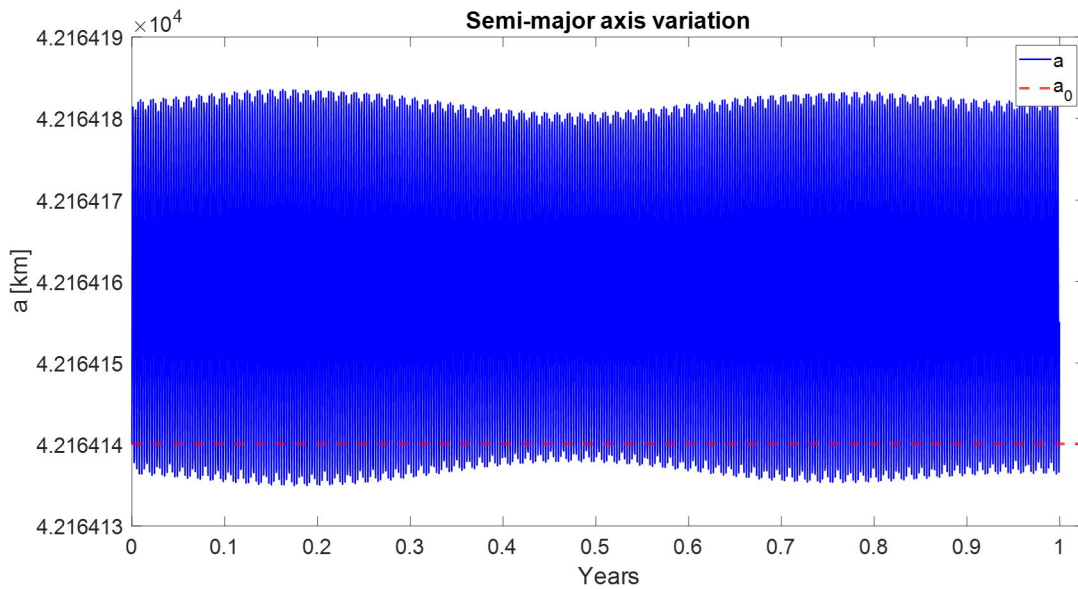


Figure 3.46 Variation of the semi-major axis of a GEO due to solar radiation pressure.

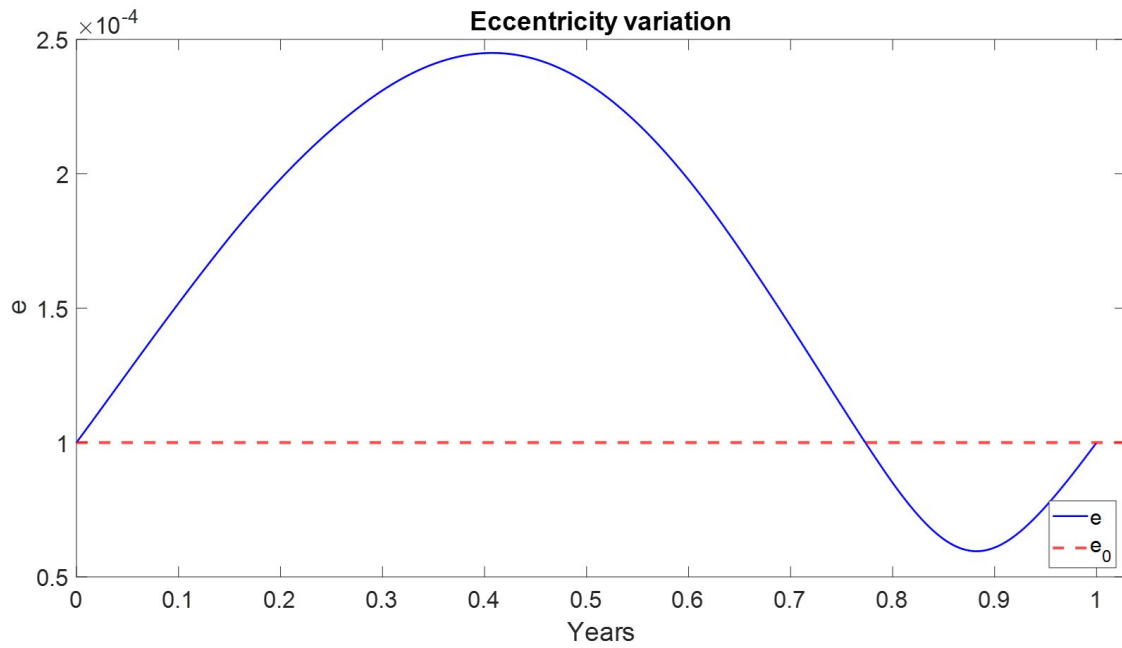


Figure 3.47 Variation of the eccentricity of a GEO due to solar radiation pressure.

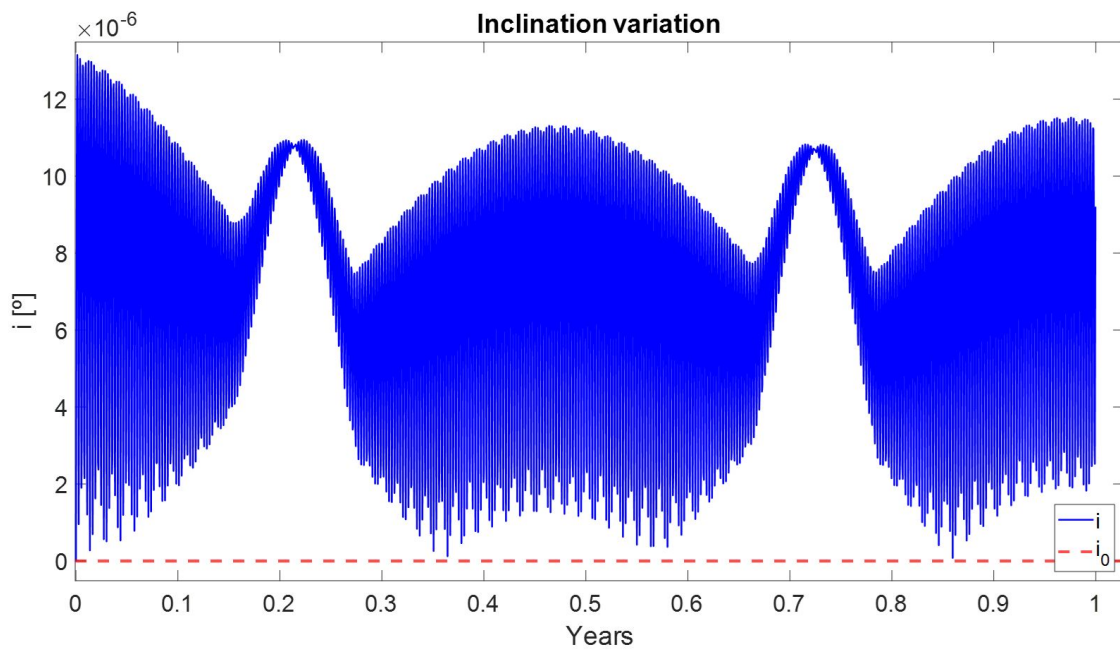


Figure 3.48 Variation of the inclination of a GEO due to solar radiation pressure.

The satellite's orbital elements variations behave as predicted in Table 2.1: periodic in a , e and i , with a period shorter than or equal to the simulation time. This is not the case for all satellites affected by solar radiation pressure. The period of the variations can be as long as a year due to the annual motion of Earth about the Sun, but become more complex if the satellite passes through Earth's shadow [22].

3.3.7 LEO satellite affected by solar radiation pressure

In this section we analyse the effect of solar pressure radiation on a LEO in a one-year period. We will consider the same LEO as in Section 3.3.2. The variations are presented in the figures below.

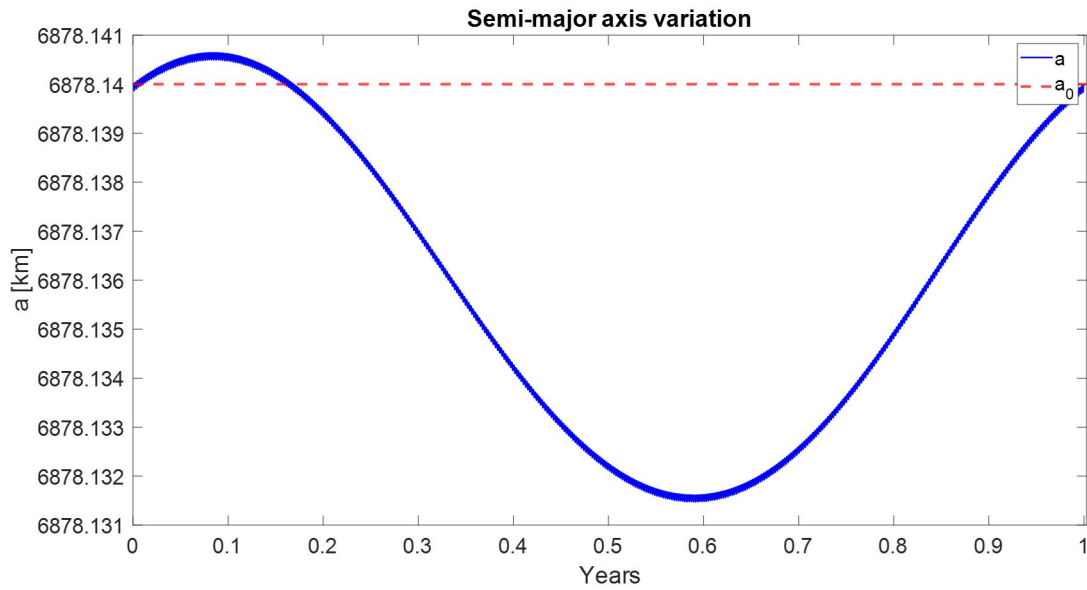


Figure 3.49 Variation of the semi-major axis of a LEO due to solar radiation pressure.

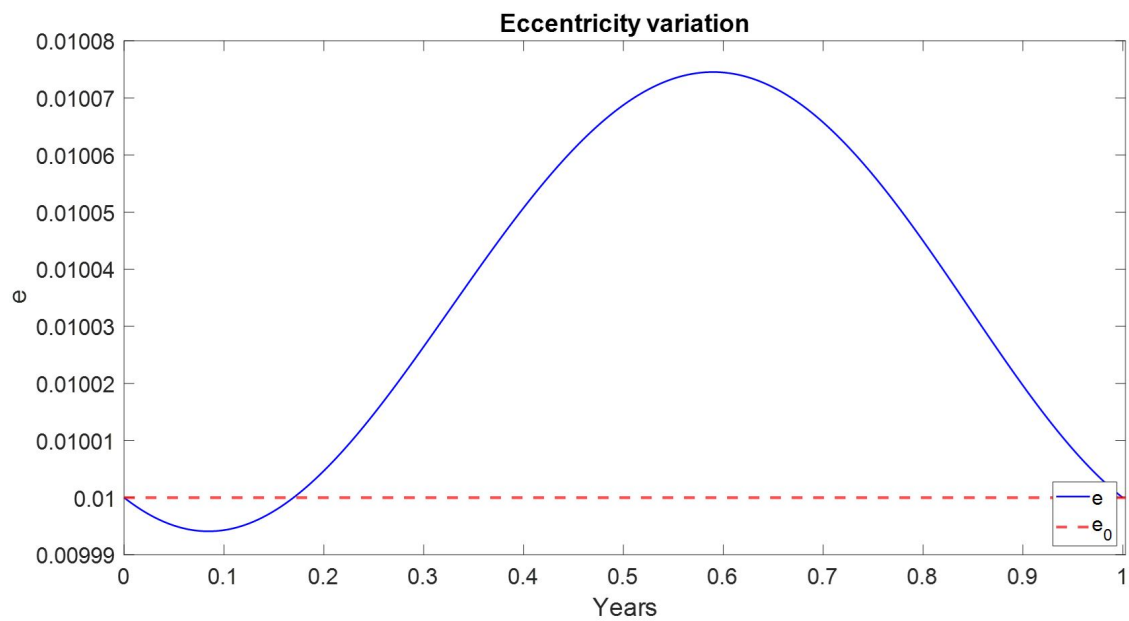


Figure 3.50 Variation of the eccentricity of a LEO due to solar radiation pressure.

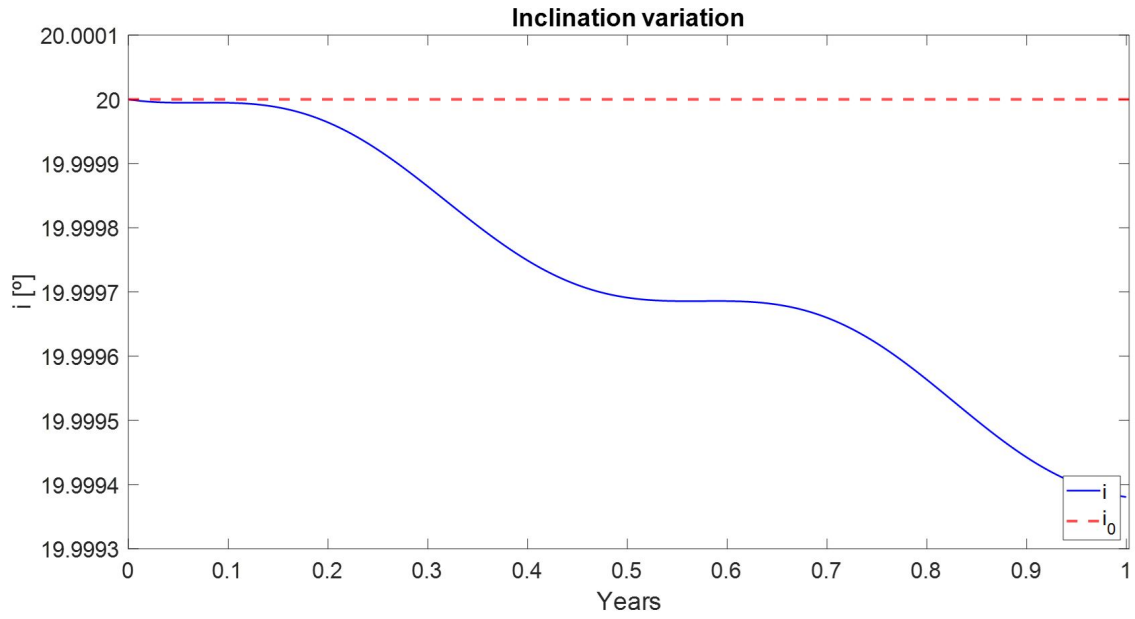


Figure 3.51 Variation of the inclination of a LEO due to solar radiation pressure.

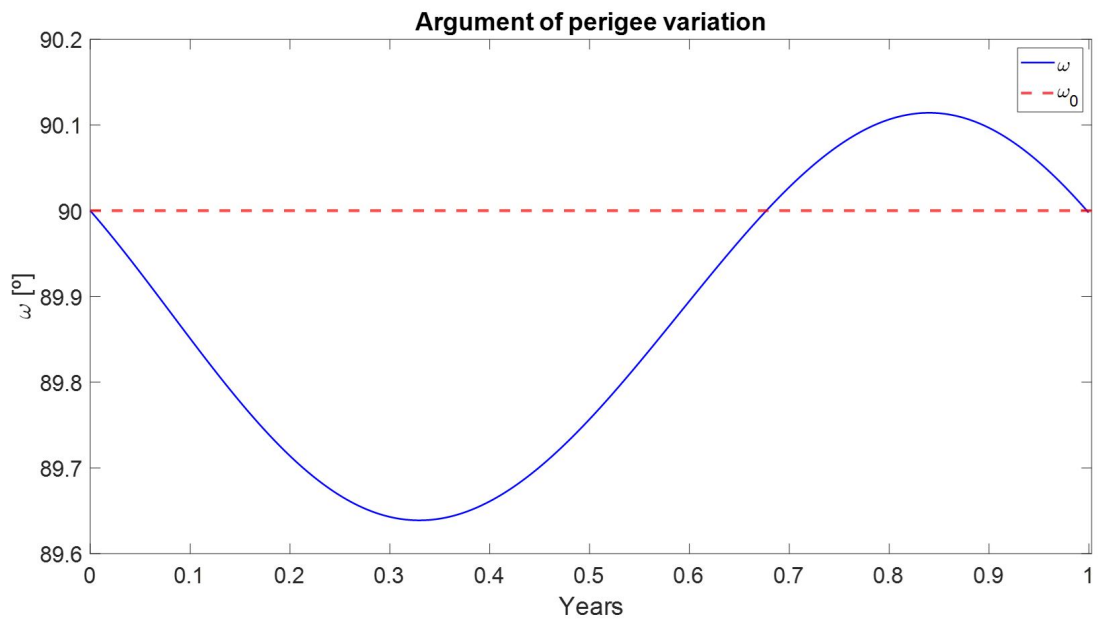


Figure 3.52 Variation of the argument of the perigee of a LEO due to solar radiation pressure.

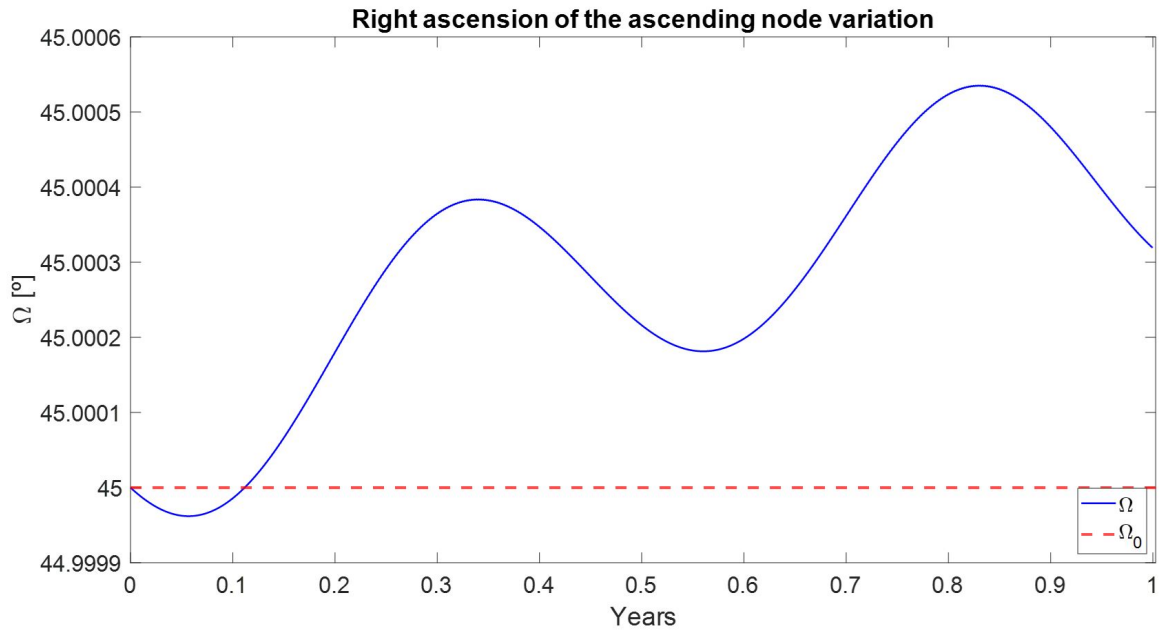


Figure 3.53 Variation of the RAAN of a LEO due to solar radiation pressure.

As we discussed in the previous example, the periods are hard to determine when the satellite passes through Earth's shadow. Therefore, in this case of study the period for i and Ω are longer than a year.

4 Precise analysis and characterisation of real satellites in Low Earth Orbits

As mentioned in the introduction, the main objective of this project is to use the radar data available to design a propagation model that recreates the satellites orbits with the minimum error possible. The radar data is provided by the European Space Agency (ESA) and is private. Consequently, it is not shown in this project in order to preserve its privacy.

4.1 Orbit ephemeris message (OEM)

In this section we describe the data format used by ESA in order to store the satellites' characteristics, such as position, velocity, epoch, etc. This data format is extensively explained in [4], which is used in this project to present OEM's format.

An OEM is used to specify the position and velocity of a single object at one or multiple epochs within a specified time range. They permit exchange of information, which may be used for pre-flight planning for tracking or navigation support, scheduling tracking support, performing orbit comparisons, performing orbit conjunction studies, etc. OEMs are prepared to perform exchanges of data between computers (automated interaction). They also allow for dynamic modelling of any number of gravitational and non-gravitational accelerations and require interpolation to interpret the position and velocity at times different from the tabular epochs. OEMs can also contain a covariance matrix, which is optional, that provides an estimation of the uncertainty of the orbit solution used to generate states in the ephemeris.

The OEM shall be a plain text file consisting of orbit data for a single object. It shall be easily readable by both humans and computers. The OEM file-naming scheme should be agreed on a case-by-case basis between the participants, typically using an Interface Control Document (ICD). The method for exchanging OEMs should be decided on a case-by-case basis by the participants and documented in an ICD.

The OEM shall be represented as a combination of the following:

- a header.
- metadata (data about the data).
- ephemeris data.
- optional covariance matrix data.
- optional explanatory information.

Table 4.1 OEM Layout.

Required sections	Header Metadata Ephemeris Data (Appropriate comments should also be included)
Allowable repetitions of sections	Covariance Matrix (optional) Metadata Ephemeris Data Covariance Matrix (optional) Metadata Ephemeris Data Covariance Matrix (optional) Metadata Ephemeris Data : (Appropriate comments should also be included)

4.1.1 OEM Header

The header of each OEM assignments are shown in Table 4.2, which specifies:

- the keyword to be used. There are four possible keywords: CCSDS_OEM_VERS, COMMENT, CREATION_DATE and ORIGINATOR.
- a short description of the item.
- examples of allowed values.
- whether the item is obligatory or optional.

Table 4.2 OEM Header.

Keyword	Description	Examples	Obligatory
CCSDS_OEM_VERS	Format version in the form of 'x.y'. 'y' is incremented for corrections and minor changes, and 'x' is incremented for major changes.	2.0	Yes
COMMENT	Comments	COMMENT	No
CREATION_DATE	File creation date and time in UTC.	2020-09-04T12:47:03 2004-123T03:15:21	Yes
ORIGINATOR	Creating agency or operator. The country of origin should also be provided.	CNES, GSFC, GSOC INMARSAT/UK	Yes

OEM Metadata

In OEM format, a single metadata group shall precede ephemeris data block and before each metadata group the string META_START shall appear on a separate line. After each metadata group, the string META_STOP shall appear on a separate line. The available metadata is shown in Table 4.3.

Table 4.3 OEM Metadata.

Keyword	Description	Examples	Required
META_START	Keyword used to delineate the start of a metadata block.	n/a	Yes
COMMENT	Comments	COMMENT	No
OBJECT_NAME	Name of the object. It is recommended to use names from SPACEWARN Bulletin [19].	STS 106 Sentinel-1A	Yes
OBJECT_ID	Object identifier. Recommended values have the format YYYY-NNNP{PP}. YYYY = Year of launch. NNN = Serial number of launch. P{PP} = At least one letter of the part brought into space.	2000-052A 2014-016A 2000-053A 1996-008A 1996-068A 1994-041A	Yes
CENTER_NAME	Origin of reference frame, which may be a natural solar system body.	EARTH, MOON, SUN EARTH BARYCENTER	Yes
REF_FRAME	Name of the reference frame in which the ephemeris are given.	ITRF-93, EME2000 ITRF2000, TDR	Yes
REF_FRAME_EPOCH	Epoch of reference frame.	2001-11-06T11:13:21:04	No
TIME_SYSTEM	Time system used for metadata, ephemeris data and covariance data.	UTC, TAI, TT GPS, TDB, TCB	Yes
START_TIME	Start of total time span covered in ephemeris and covariance data following this metadata block.	1996-277T07:22:54 1990-01-01T17:02:32 2001-04-03T04:00:00	Yes
STOP_TIME	End of total time span covered in ephemeris and covariance data preceding this metadata block.	2022-001T11:22:04 1999-06-10T10:22:00 2004-07-21T12:30:00	Yes
INTERPOLATION	Recommended interpolation method.	Hermite, Linear, Lagrange	No
INTERPOLATION_DEGREE	Recommended interpolation degree.	5, 1, 2	No
META	Keyword used to delineate the end of a metadata block.	n/a	Yes

It is worth noting that there could also be two extra keywords in the OEM metadata: USEABLE_TIME_START and USEABLE_TIME_STOP. These variables determine the time span that the users shall use if interpolation is required.

4.1.2 OEM Data: Ephemeris data lines

Each set of ephemeris data must be provided on a single line. The ephemeris shall include: Epoch, X, Y, Z, X_DOT, Y_DOT, Z_DOT, X_DDOT, Y_DDOT, Z_DDOT. The position and velocity terms shall be obligatory, acceleration terms may be provided. To separate the items in each ephemeris data line, one space character must be used.

4.1.3 OEM Data: Covariance matrix lines

A single covariance matrix data section may optionally follow each ephemeris data block. It must be preceded and followed by the keywords COVARIANCE_START and COVARIANCE_STOP. If the reference frame of the covariance matrix is different from that of the states in the ephemeris, it must be provided with the keyword COV_REF_FRAME.

4.1.4 OEM Examples

In this section we show three examples in order to clarify the OEM format.

In Figure 4.1 there are two metadata blocks, each one preceded and followed by the keywords META_START and META_STOP. In this OEM no covariance matrix nor acceleration data is provided.

In Figure 4.2 there is only one metadata block. In this file the accelerations are provided. Finally, in Figure 4.3, the covariance matrices are used to estimate the error.

```
CCSDS_OEM_VERSION = 2.0
CREATION_DATE = 1996-11-04T17:22:31
ORIGINATOR = NASA/JPL

META_START
OBJECT_NAME      = MARS GLOBAL SURVEYOR
OBJECT_ID        = 1996-062A
CENTER_NAME      = MARS BARYCENTER
REF_FRAME        = EME2000
TIME_SYSTEM      = UTC
START_TIME       = 1996-12-18T12:00:00.331
USEABLE_START_TIME = 1996-12-18T12:10:00.331
USEABLE_STOP_TIME  = 1996-12-28T21:23:00.331
STOP_TIME        = 1996-12-28T21:28:00.331
INTERPOLATION     = HERMITE
INTERPOLATION_DEGREE = 7
META_STOP

COMMENT This file was produced by M.R. Somebody, MSO NAV/JPL, 1996NOV 04. It is
COMMENT to be used for DSN scheduling purposes only.

1996-12-18T12:00:00.331 2789.619 -280.045 -1746.755 4.73372 -2.49586 -1.04195
1996-12-18T12:01:00.331 2783.419 -308.143 -1877.071 5.18604 -2.42124 -1.99608
1996-12-18T12:02:00.331 2776.033 -336.859 -2008.682 5.63678 -2.33951 -1.94687

  < intervening data records omitted here >

1996-12-28T21:28:00.331 -3881.024 563.959 -682.773 -3.28827 -3.66735 1.63861

META_START
OBJECT_NAME      = MARS GLOBAL SURVEYOR
OBJECT_ID        = 1996-062A
CENTER_NAME      = MARS BARYCENTER
REF_FRAME        = EME2000
TIME_SYSTEM      = UTC
START_TIME       = 1996-12-28T21:29:07.267
USEABLE_START_TIME = 1996-12-28T22:08:02.5
USEABLE_STOP_TIME  = 1996-12-30T01:18:02.5
STOP_TIME        = 1996-12-30T01:28:02.267
INTERPOLATION     = HERMITE
INTERPOLATION_DEGREE = 7
META_STOP

COMMENT This block begins after trajectory correction maneuver TCM-3.

1996-12-28T21:29:07.267 -2432.166 -063.042 1742.754 7.33702 -3.495867 -1.041945
1996-12-28T21:59:02.267 -2445.234 -878.141 1873.073 1.86043 -3.421256 -0.996366
1996-12-28T22:00:02.267 -2458.079 -683.858 2007.684 6.36786 -3.339563 -0.946654

  < intervening data records omitted here >

1996-12-30T01:28:02.267 2164.375 1115.811 -688.131 -3.53328 -2.88452 0.88535
```

Figure 4.1 Version 1 OEM without acceleration nor covariance.

```

CCSDS_OEM_VERSION = 2.0

COMMENT  OEM WITH OPTIONAL ACCELERATIONS MUST BE OEM VERSION 2.0

CREATION_DATE = 1996-11-04T17:22:31
ORIGINATOR = NASA/JPL

META_START
OBJECT_NAME      = MARS GLOBAL SURVEYOR
OBJECT_ID        = 1996-062A
CENTER_NAME      = MARS BARYCENTER
REF_FRAME        = EME2000
TIME_SYSTEM      = UTC
START_TIME       = 1996-12-18T12:00:00.331
USEABLE_START_TIME = 1996-12-18T12:10:00.331
USEABLE_STOP_TIME  = 1996-12-28T21:23:00.331
STOP_TIME        = 1996-12-28T21:28:00.331
INTERPOLATION     = HERMITE
INTERPOLATION_DEGREE = 7
META_STOP

COMMENT  This file was produced by M.R. Somebody, MSO NAV/JPL, 2000 NOV 04. It is
COMMENT  to be used for DSN scheduling purposes only.

1996-12-18T12:00:00.331 2789.6 -280.0 -1746.8 4.73 -2.50 -1.04 0.008 0.001 -0.159
1996-12-18T12:01:00.331 2783.4 -308.1 -1877.1 5.19 -2.42 -2.00 0.008 0.001 0.001
1996-12-18T12:02:00.331 2776.0 -336.9 -2008.7 5.64 -2.34 -1.95 0.008 0.001 0.159

  < intervening data records omitted here >

1996-12-28T21:28:00.331 -3881.0 564.0 -682.8 -3.29 -3.67 1.64 -0.003 0.000 0.000

```

Figure 4.2 Version 2 OEM with optional accelerations.

```

CCSDS_OEM_VERSION = 2.0
CREATION_DATE = 1996-11-04T17:22:31
ORIGINATOR = NASA/JPL

META_START
OBJECT_NAME      = MARS GLOBAL SURVEYOR
OBJECT_ID        = 1996-062A
CENTER_NAME      = MARS BARYCENTER
REF_FRAME        = EME2000
TIME_SYSTEM      = UTC
START_TIME       = 1996-12-28T21:29:07.267
USEABLE_START_TIME = 1996-12-28T22:08:02.5
USEABLE_STOP_TIME  = 1996-12-30T01:18:02.5
STOP_TIME        = 1996-12-30T01:28:02.267
INTERPOLATION     = HERMITE
INTERPOLATION_DEGREE = 7
META_STOP

COMMENT  This block begins after trajectory correction maneuver TCM-3.

1996-12-28T21:29:07.267 -2432.166 -063.042 1742.754 7.33702 -3.495867 -1.041945
1996-12-28T21:59:02.267 -2445.234 -878.141 1873.073 1.86043 -3.421256 -0.996366
1996-12-28T22:00:02.267 -2458.079 -683.858 2007.684 6.36786 -3.339563 -0.946654

  < intervening data records omitted here >

1996-12-30T01:28:02.267 2164.375 1115.811 -688.131 -3.53328 -2.88452 0.88535

COVARIANCE_START
EPOCH = 1996-12-28T21:29:07.267
COV_REF_FRAME = EME2000
  3.3313494e-04
  4.6189273e-04  6.7824216e-04
-3.0700078e-04 -4.2212341e-04  3.2319319e-04
-3.3493650e-07 -4.6860842e-07  2.4849495e-07  4.2960228e-10
-2.2118325e-07 -2.8641868e-07  1.7980986e-07  2.6088992e-10  1.7675147e-10
-3.0413460e-07 -4.9894969e-07  3.5403109e-07  1.8692631e-10  1.0088625e-10  6.2244443e-10

EPOCH = 1996-12-29T21:00:00
COV_REF_FRAME = EME2000
  3.4424505e-04
  4.5078162e-04  6.8935327e-04
-3.0600067e-04 -4.1101230e-04  3.3420420e-04
-3.2382549e-07 -4.5750731e-07  2.3738384e-07  4.3071339e-10
-2.1007214e-07 -2.7530757e-07  1.6870875e-07  2.5077881e-10  1.8786258e-10
-3.0302350e-07 -4.8783858e-07  3.4302008e-07  1.7581520e-10  1.0077514e-10  6.2244443e-10
COVARIANCE_STOP

```

Figure 4.3 Version 2 OEM with optional covariance matrix.

4.2 Perturbations model verification and validation

In Section 3.2.3 we said that Orekit provides a wide scope for analysing the different perturbations that affect orbiting objects. To design a good perturbation model that accurately describes the satellites' orbits studied in this project, we divide the study of the different perturbations' models by analysing them separately. This is, studying the effect of different models for third-body perturbations, non-spherical body's gravity, atmospheric drag and solar radiation.

To propagate orbits with high accuracy is truly complicated as there are many techniques and we often select one method over another for the wrong reason. To corroborate the model designed for this project, we verify and validate the model. As Vallado says [22], "the largest misconception in evaluating methods of propagations is what represents truth. We verify to existing data or results (ensure it's coded properly), while we validate that the model accurately reflects the truth (consistent and reliable results)."

The satellite used in this analysis is Sentinel-1A [12], a European radar imaging satellite launched in 2014. It carries a C-band Synthetic Aperture Radar which provides images in all light and weather conditions. Basically, this satellite serves as a tracker of many aspects of our environment. It has an apogee altitude of 693 km and an inclination of 98.18°, being a Sun-synchronous satellite of 2170 kg [1].

Orekit provides several models to compute the perturbations described in Section 2.2. To design the optimal propagator we decided to test different models and select the ones that perform the best. This analysis is carried out as follows:

- First, we randomly select one model for each of the perturbations that we considered in this project.
- Then, when we want to study, for example, different models for the non-spherical body's gravity, we only change the model that models this perturbation, without modifying the rest of the models described below.

This allows us to accurately compare the influence of using one model or another. The fixed models that have been selected to remain the same whenever the perturbation they model is not the one being analysed are the following:

- **Non-spherical body's gravity:** We use a 40-40 harmonic degree/order model.
- **Atmospheric drag:** As we do not have the data to analyse the attitude of the satellite, we use the isotropic drag model implemented in Orekit. It considers that all coefficients are constant and do not depend of the direction of the satellite. To model the atmosphere (which is the main problem when analysing atmospheric drag) we consider the Harris-Priester model, which is reasonably precise and fast.
- **Third-Body perturbations:** In Section 2.2.3 we compared the magnitude of the Keplerian force and the force exerted by the main bodies in the solar system. Hence, we take into account just the Sun and the Moon for the standard model.
- **Solar-Radiation pressure:** We consider the isotropic radiation single coefficient model implemented in Orekit, which corresponds with Eq. (2.28).

The most efficient perturbation model is decided by comparing the propagation data with the data available from the OEMs. We choose the one that provides the higher accuracy/speed relation.

To analyse the error committed we randomly selected a 24-hour OEM window data and compared the simulations with the data available.

4.2.1 Optimisation process

Atmospheric drag, as well as solar-radiation pressure, depend on geometric parameters of the satellites under analysis. These parameters ($S \equiv$ Surface, $S_{SRP} \equiv$ Surface affected by solar-radiation pressure and $C_D \equiv$ Drag coefficient) are computed through an optimisation process.

Orekit allows users to input the attitude of the satellite under study to accurately analyse the orientation-dependent atmospheric drag and solar-radiation pressure. In this project, the lack of information forces us to use models that do not consider any orientation, assuming that the satellite is a spherical body with S^* , S_{SRP}^* and C_D^* geometry. These models, called isotropic models, can not accurately predict the satellite's orbit if we use the geometric features of the original satellite S , S_{SRP} and C_D (the non-spherical ones). Therefore, we have decided to calculate the spherical geometric parameters that minimise the average error made when using these models. This is:

$$\min \left(\left| \vec{P}(S, S_{SRP}, C_D, \vec{\phi}) - \vec{P}^*(S^*, S_{SRP}^*, C_D^*) \right| \right), \quad (4.1)$$

where \vec{P} is the position of the satellite with its real parameters (this is, the position given by the OEMs), $\vec{\phi}$ is the orientation of the satellite and \vec{P}^* is the position computed by the propagator assuming a spherical shape. Therefore, S^* , S_{SRP}^* and C_D^* represent the values that minimise the error committed assuming a spherical shape.

This optimisation process is performed for each group of satellites (Sentinel-1 and Sentinel-2) after the selection of the optimal propagator. However, the values obtained slightly vary depending on the segment chosen. To palliate this, we decided to average the values obtained between different segments.

We need the Sentinel-1A geometry to analyse different atmospheric drag and solar-radiation pressure models. These values ($S^* = 3 \text{ m}^2$, $S_{SRP}^* = 9.76 \text{ m}^2$ and $C_D^* = 1.75$) have been extracted from [18], where a similar process has been carried out to obtain these values. They serve as the initial values for the optimisation process as well.

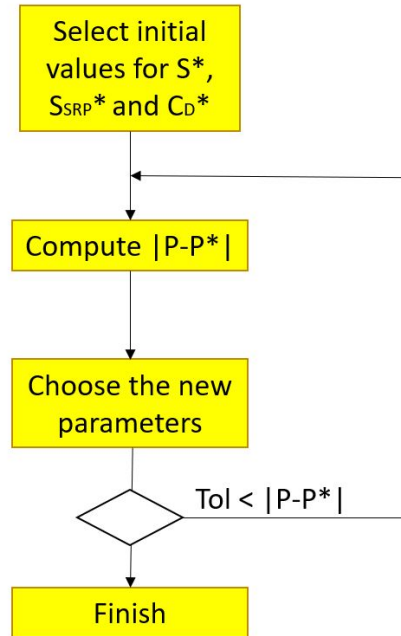


Figure 4.4 Process of optimisation.

4.2.2 Non-spherical body's gravity

We discussed in Section 2.2.1 the importance of accurately modelling the mass distribution of Earth. Increasing the order/degree of the harmonic model used should increase accuracy at the same time as it increases the computational time required to perform the computations. We decided to compare the computational time and the accuracy of 5-5, 10-10, 20-20, 40-40 and 80-80 degree/order harmonic models in order to determine which one is the most efficient in terms of precision and speed. In the following figures we present the error committed by each of the models during a 24-hour window in position and velocity. The computational time required by each harmonic model is presented in Table 4.4, as well as the position error and the velocity error at the end of the 24-hour period and the maximum position error and the maximum velocity error.

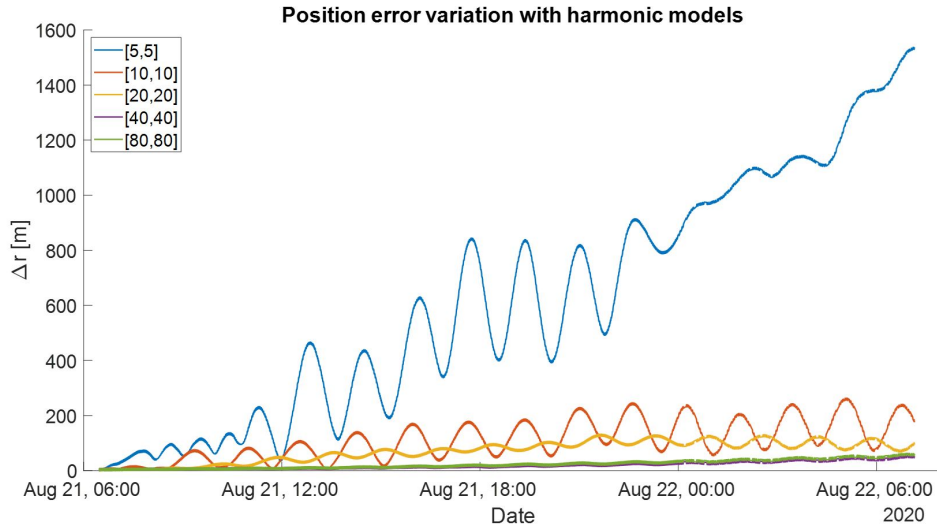


Figure 4.5 Position error variation with different Earth harmonic models in a 24-hour window.

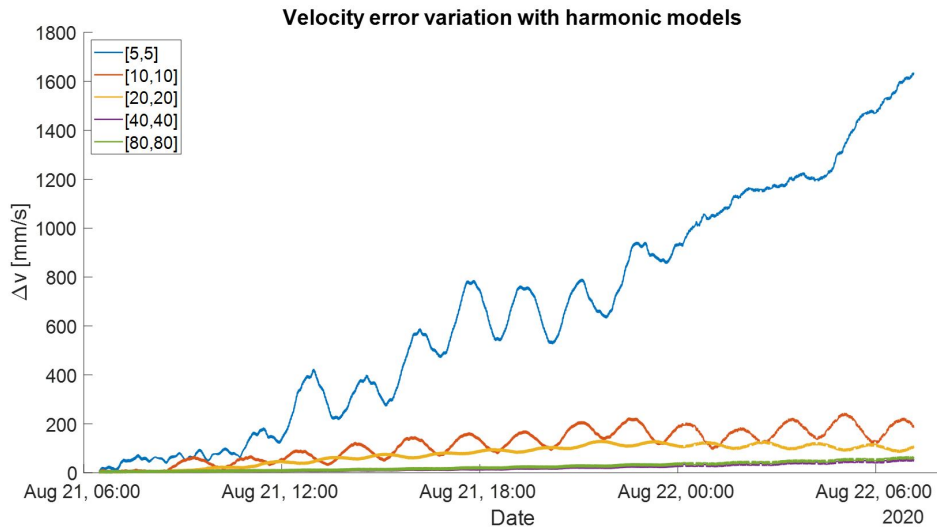


Figure 4.6 Velocity error variation with different Earth harmonic models in a 24-hour window.

Table 4.4 Comparison between different harmonic models in a 24-hour window.

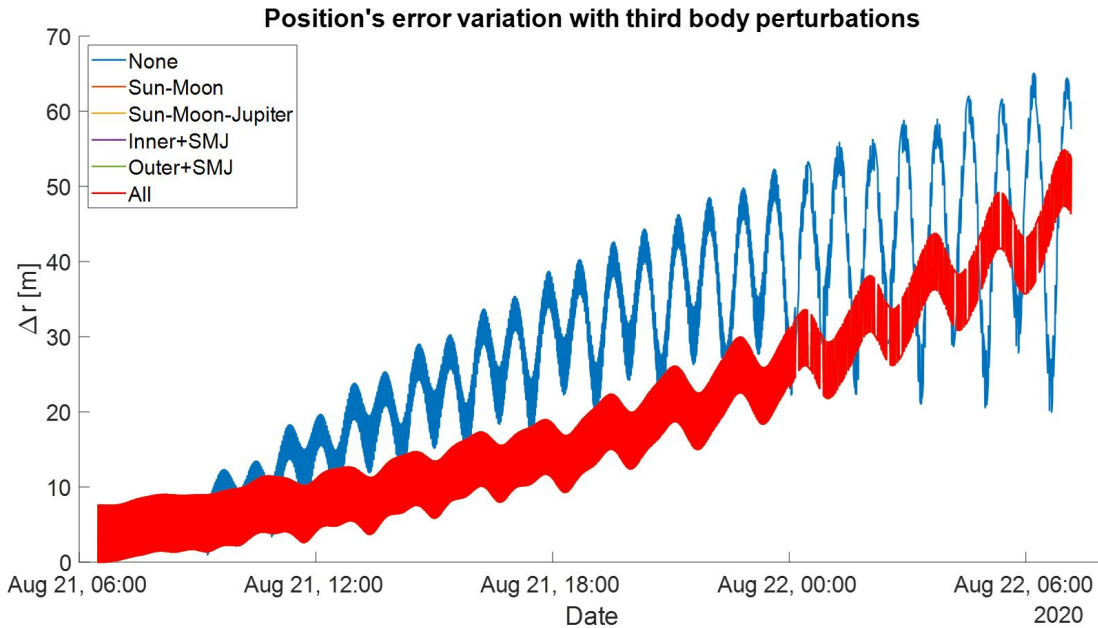
Degree/Order	Time [s]	Maximum position error [m]	Maximum velocity error [mm/s]	Final position error [m]	Final velocity error [mm/s]
5-5	13.63	1537.03	1635.80	1537.03	1635.80
10-10	13.65	263.52	242.85	175.47	184.36
20-20	16.22	132.49	132.18	94.86	100.97
40-40	22.24	54.87	56.24	53.84	56.03
80-80	38.01	62.52	64.90	61.23	64.68

Observing Figures 4.5 and 4.6 we clearly see that from the 5-5 model to the 40-40 model the errors in position and velocity decrease as we increase the model complexity. However, when we compare the 40-40 and the 80-80 models we see that we lose accuracy and we increase the computational time by 71%. We could expect that increasing the complexity of the model should increase the accuracy, which is true in theory. Nevertheless, using too much complexity in the harmonics model also increase the uncertainty of the model and the error accumulated in the 24-hour period selected due to the immense amount of calculations performed, making it less accurate and less efficient.

Therefore, as the 40-40 degree/order harmonic model is the optimal one in terms of computational time and accuracy, we use this model to propagate the orbits of the satellites.

4.2.3 Third-Body perturbations

In previous analyses (Section 2.2.3 and Table 2.2) we concluded that the most important third-body perturbations are the ones exerted by the Sun and the Moon when we study geocentric orbits. To be sure of this conclusion we study the variation of the error committed and the computational time required when we add more and more solar system objects to the propagator. The models taken into account are: none third-body perturbations, Luni-Solar perturbations, Sun-Moon-Jupiter (SMJ) perturbations, inner planets and SMJ perturbations, outer planets and SMJ perturbations and all-bodies perturbations. The results are presented in the following figures:

**Figure 4.7** Position error variation with different third body perturbation models.

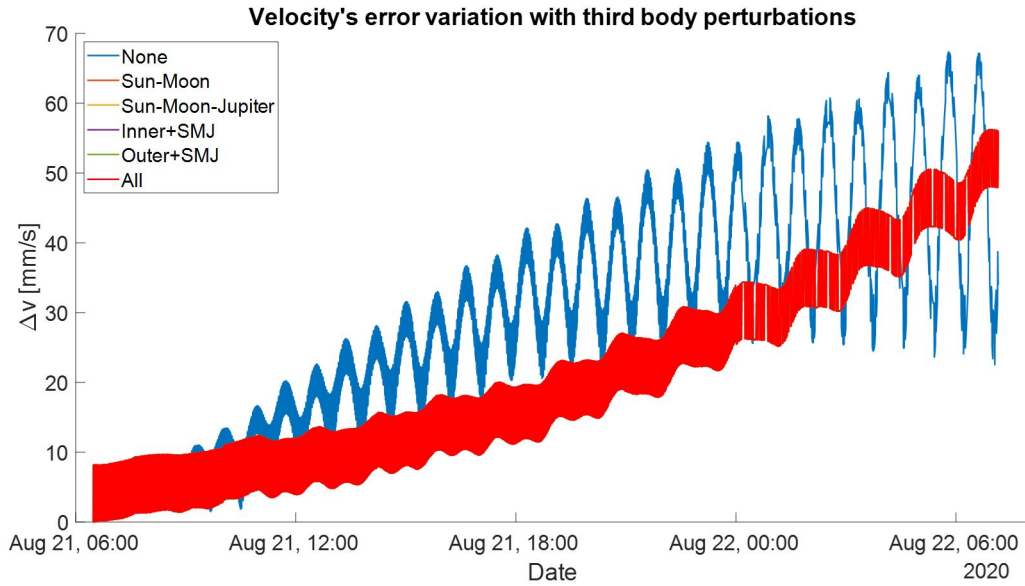


Figure 4.8 Velocity error variation with different third body perturbation models.

We can not see any difference in the figures between the Luni-Solar perturbation model and the rest of the models, so Table 4.5 is presented to compare them.

Table 4.5 Comparison between different third-body models in a 24-hour window.

Model	Time [s]	Maximum position error [m]	Maximum velocity error [mm/s]	Final position error [m]	Final velocity error [mm/s]
None	20.05	65.06	67.36	57.62	34.01
Luni-Solar	22.24	54.87	56.24	53.84	56.03
SMJ	23.19	54.87	56.24	53.84	56.03
Inner+SMJ	24.05	54.87	56.24	53.84	56.03
Outer+SMJ	25.92	54.87	56.24	53.84	56.03
All	29.19	54.87	56.24	53.84	56.03

The only difference between the Luni-Solar model and the rest of the models that consider third-body perturbations is the computational time, increasing as we consider more and more solar system objects. The models errors vary, but the variation is so insignificant that it does not affect the second decimal place.

Therefore, as the results are the same for the Luni-Solar perturbation model and the more complex models, the Luni-Solar perturbation is the model that we must use when analysing geocentric orbits as it provides accurate results while also guaranteeing reasonable computation time, as we predicted in Section 2.2.3.

4.2.4 Atmospheric drag

To model atmospheric drag is very difficult due to the atmospheric variations occurring everyday. To model the atmosphere accurately we can use tabular models (like Harris-Priester) that compute the density using tables or empirical models (like NRLMSISE-00) that use daily data to obtain the atmosphere properties. In Section 2.2.2 we described several numerical models that approximate the properties of the air at a given altitude and we compare in this section the two most-used models

nowadays: Harris-Priester and NRLMSISE-00. We do not compare these models with the recently developed JB2008 because Orekit does not provide any method to obtain the data needed in this model yet.

On the other hand, we use the isotropic drag model (which supposes that all coefficients are constant and do not depend of the direction) as we do not know the satellite's attitude.

We present the comparison between Harris-Priester atmospheric model and NRLMSISE-00 atmospheric model in the following figures, as well as Table 4.6 with the maximum errors and closing errors.

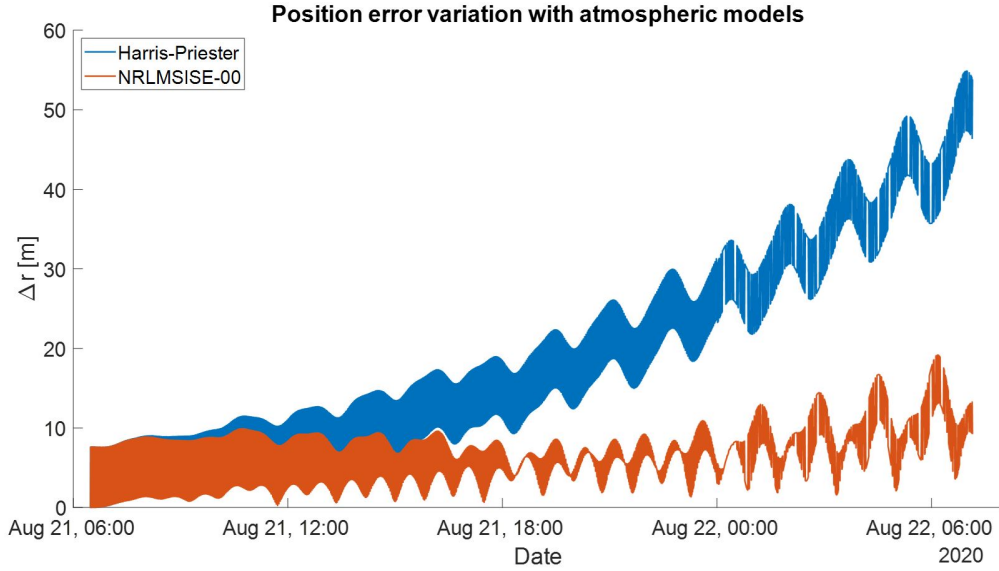


Figure 4.9 Position error variation with different atmospheric models in a 24-hour window.

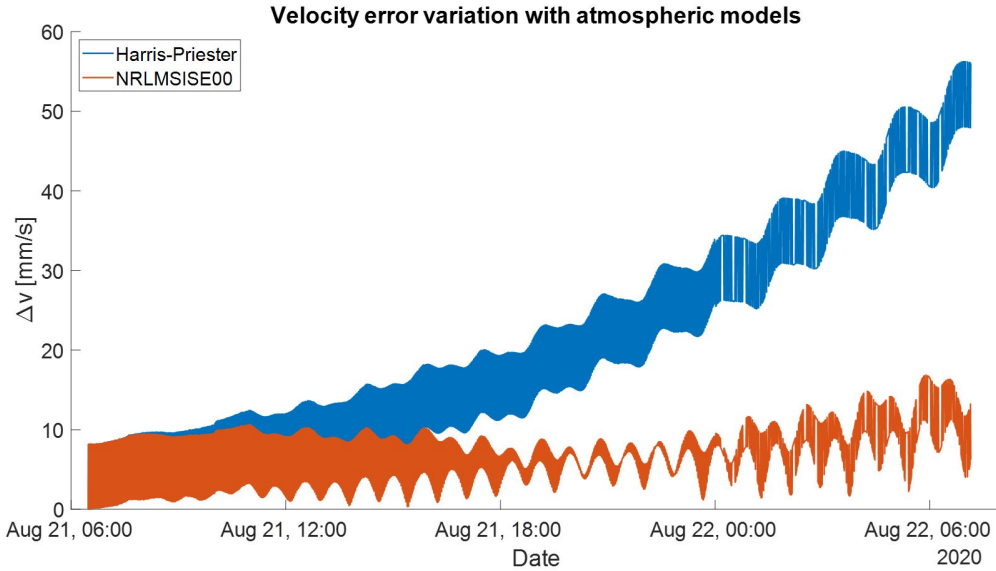


Figure 4.10 Velocity error variation with different atmospheric models in a 24-hour window.

Table 4.6 Comparison between different atmospheric models in a 24-hour window.

Atmospheric model	Time [s]	Maximum position error [m]	Maximum velocity error [mm/s]	Final position error [m]	Final velocity error [mm/s]
Harris-Priester	21.78	54.87	56.24	53.84	56.03
NRLMSISE-00	24.41	19.17	16.88	9.24	6.25

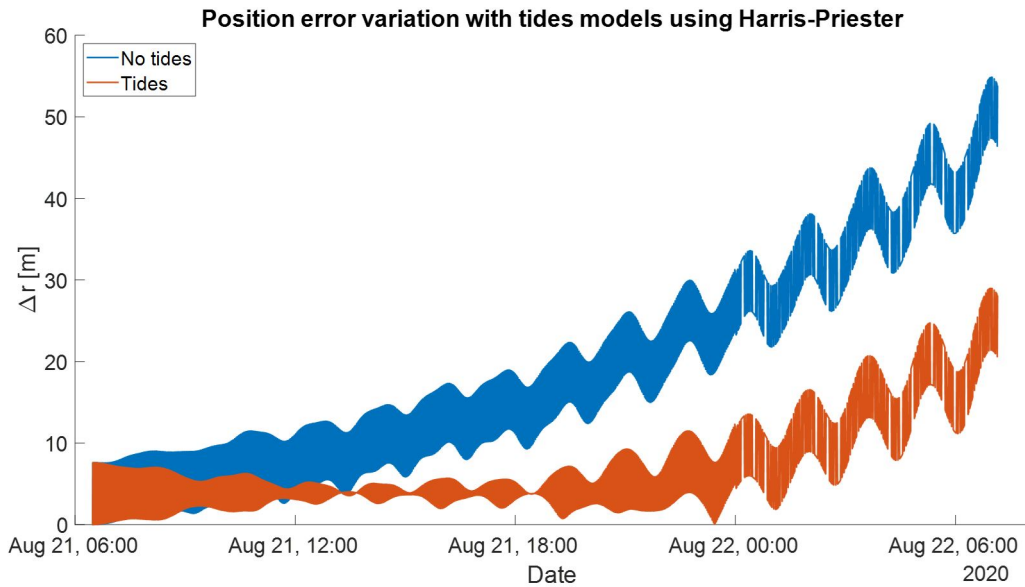
We could conclude that using the NRLMSISE-00 is, in general, a better choice. Nevertheless, in the study performed in Section 4.2.6 we see that adding tides make NRLMSISE-00 perform worse than Harris-Priester if the propagation time is less than 24 hours or higher than 39 hours. This result is discussed in detail in the section mentioned before.

4.2.5 Solar-Radiation pressure

As we mentioned before, the data available of the satellites under study does not include their attitude. This lack of information hinders the modeling of solar-radiation pressure (and atmospheric drag). Therefore, we use the isotropic radiation single coefficient model implemented in Orekit, which corresponds with the model described in Eq. (2.28). As no other model is used, the initial model proposed for the standard model is the one that we use to predict the position and velocity of the satellites under study.

4.2.6 Tides

We have already studied the effect of using different models to compute the four main perturbations. In Section 2.2.5 we described other perturbations that we could take into account and deduced that tides are the most important among the ones mentioned. These kind of perturbation are no negligible, as their effect in LEO can divert the satellites out of their original orbit dozens of metres. We compare the standard model (which uses Harris-Priester atmospheric model) when we use no tides and tides. The results are presented in the following figures and in Table 4.7.

**Figure 4.11** Position error variation with tides models in a 24-hour window using Harris-Priester.

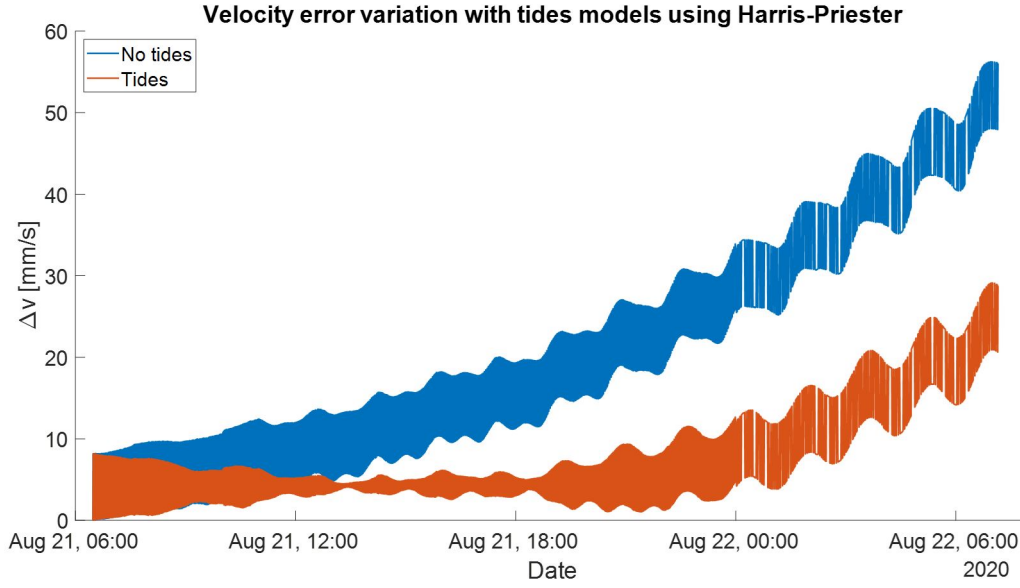


Figure 4.12 Velocity error variation with tides models in a 24-hour window using Harris-Priester.

Table 4.7 Comparison between different tides models in a 24-hour window.

Tides model	Time [s]	Maximum position error [m]	Maximum velocity error [mm/s]	Final position error [m]	Final velocity error [mm/s]
No tides	22.10	54.87	56.24	53.84	56.03
Tides	23.561	28.98	29.12	28.10	28.75

These results state that using tides is necessary to propagate accurately the orbit of the satellites under study. However, if we implement the NRLMSISE-00 atmospheric model when using tides instead of Harris-Priester the propagator gets worse. This result is presented in the following figures:

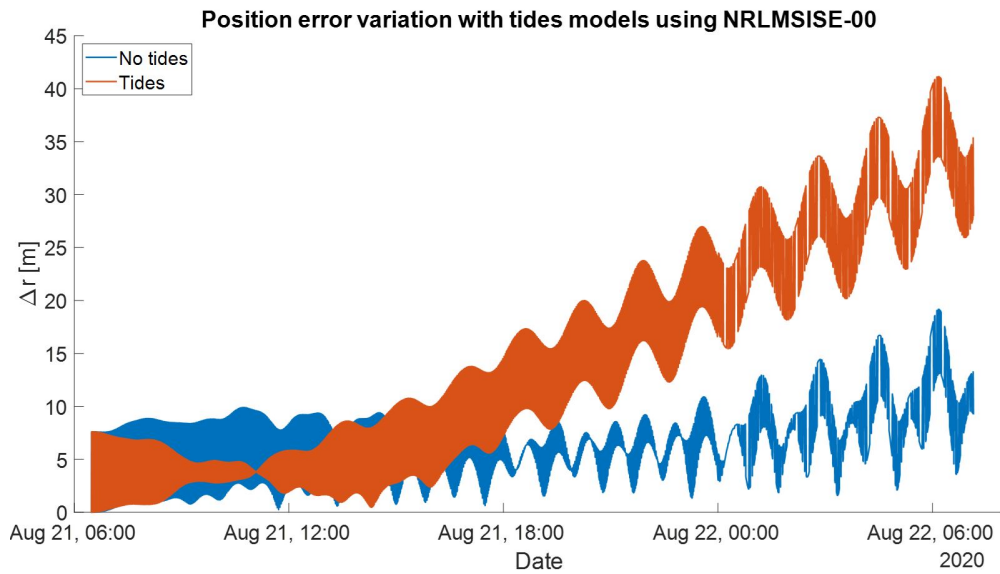


Figure 4.13 Position error variation with tides models in a 24-hour window using NRLMSISE-00.

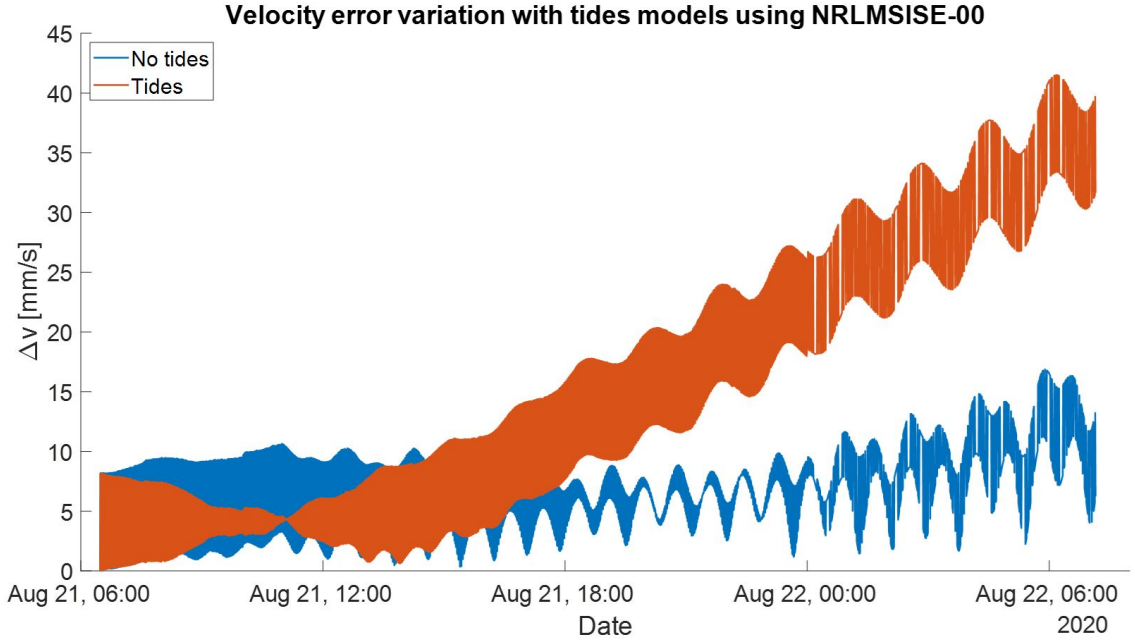


Figure 4.14 Velocity error variation with tides models in a 24-hour window using NRLMSISE-00.

This particular result is truly striking, as we could think that using the most accurate model in each perturbation should give us the most accurate propagator possible. Nevertheless, perturbation models are not linear, and adding the most accurate ones up does not necessarily perform better than using a combination that, in theory, is less precise.

Now the following question emerges: Which model should we use in this project? The one that uses Harris-Priester and tides or the ones with NRLMSISE-00 atmospheric model without tides? We answer this question by comparing both propagators during 60 hours. The result is presented in Figure 4.15:

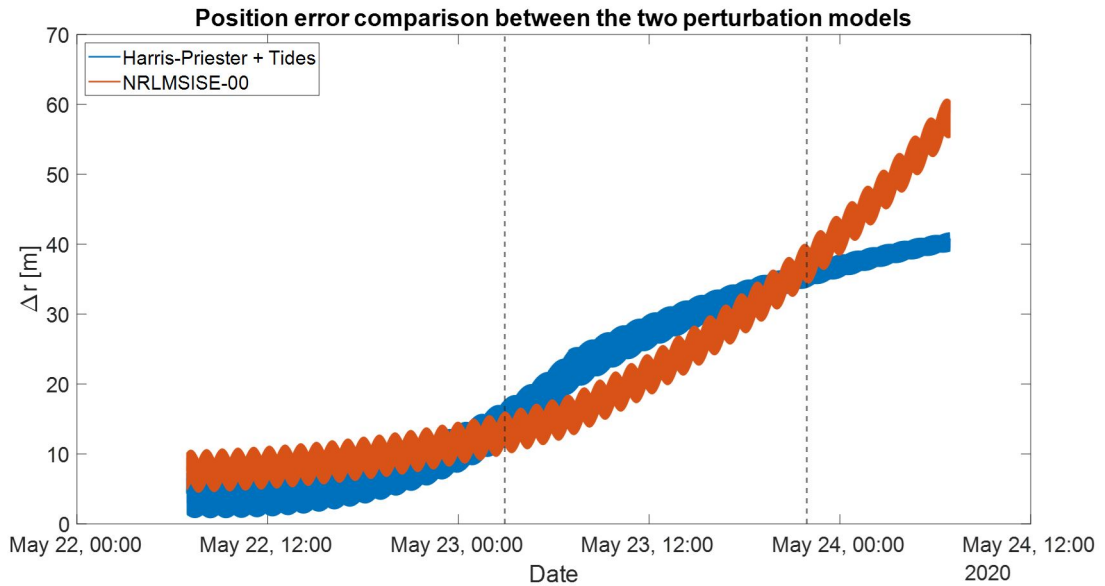


Figure 4.15 Comparison between the two models proposed.

This analysis shows that during the first 24 hours the best performing propagator is Harris-Priester with tides. Afterwards, the error of this model grows larger than the error committed with the NRLMSISE-00 atmospheric model without tides. Finally, when the propagation is longer than 39 hours, the model with tides and the Harris-Priester atmosphere outperforms the NRLMSISE-00 model. Therefore, the model used in this project is a hybrid between these two models, selecting one of them depending on the propagation duration.

4.2.7 Final propagation model

To summarise, the model that we use in this project to predict the position and velocity of the satellites Sentinel-1A/B and Sentinel-2A/B is the following:

- **Non-spherical body's gravity:** We implement a 40-40 harmonic degree/order model as improving the complexity of this model results in worse results.
- **Third-Body perturbations:** The Luni-Solar perturbations are the ones considered in this project.
- **Solar-Radiation pressure:** We use the isotropic radiation single coefficient model implemented in Orekit.
- **Atmospheric drag:** The lack of information related with the satellites' attitude force us to use the isotropic drag model, which considers that all coefficients are constant and do not depend of the direction of the satellite. To model the atmosphere we consider two scenarios: if the propagation's length is greater than 24 hours and less than 39 hours, the NRLMSISE-00 atmospheric model is used. Otherwise, the Harris-Priester atmospheric model is used.
- **Tides:** Similar to the atmospheric model, we consider two cases: if the propagation length is longer than 24 hours and shorter than 39 hours, tides are not used. Otherwise, tides are considered together with the rest of the perturbations.

4.3 Precise prediction of LEO satellites

As we mentioned in the introduction, the main objective of this project is to develop a propagator that captures the real behaviour of the four satellites under study (Sentinel-1A, Sentinel-1B, Sentinel-2A and Sentinel-2B) and that minimises the maximum and mean error during the propagation. In this section we present the results obtained when we propagate the orbit of these four object, comparing the results obtained with the data from the OEMs given by ESA. The OEMs provide data of the position and velocity of the satellites during specific time lapses, and the propagation is performed using just the initial value of these time lapses for each satellite. The error is obtained by comparing the results given by the propagator with the ones provided by ESA.

For each satellite we present two tables with the results obtained. The first one contains the initial date of the propagation, the duration of the propagation, the maximum position error, the maximum velocity error, the mean position error, the mean velocity error and an indicator for manoeuvre (Y/N). The second table summarises the results presented in the first one showing the maximum and mean value of each column of the first table, in order to facilitate the interpretation of the results.

4.3.1 Sentinel-1

First, the parameters of this satellite class are provided. They have been obtained by minimising the mean error obtained during several windows (Section 4.2.1) and by comparing them with the data provided by ESA [12]. Thus, $m = 2180 \text{ kg}$ (obtained from the ESA datasheet), $S^* = 1.76 \text{ m}^2$, $S_{SRP}^* = 9.75 \text{ m}^2$ and $C_D^* = 5.24$.

The results obtained for Sentinel-1A and Sentinel-1B are the following.

Sentinel-1A

Table 4.8 Sentinel-1A results.

Start	Duration [h]	Maximum position error [m]	Maximum velocity error [mm/s]	Mean position error [m]	Mean velocity error [mm/s]	Manoeuvre
06-Aug-2019 06:52:40	11.0125	8.8030	9.0560	4.1315	4.3313	N
06-Aug-2019 17:53:25	36.7044	16.3921	14.9128	4.7798	4.8405	Y
08-Aug-2019 06:35:50	11.0194	9.0384	9.5819	4.3234	4.6056	N
08-Aug-2019 17:37:00	24.6847	12.9223	11.0860	5.0216	5.0980	N
09-Aug-2019 18:18:05	36.7103	35.4462	33.8126	9.2625	9.6972	N
11-Aug-2019 07:00:42	11.0156	8.9177	8.1745	4.0334	4.2311	N
11-Aug-2019 18:01:38	36.7078	41.9285	40.9626	15.1721	16.0343	N
13-Aug-2019 06:44:06	11.0097	9.0247	9.4176	4.1857	4.4756	N
13-Aug-2019 17:44:41	24.6878	10.7980	10.2972	4.8385	5.0733	N
14-Aug-2019 18:25:57	12.0245	6.2222	6.7454	4.0509	4.3501	Y
15-Aug-2019 06:27:56	24.6831	15.4868	14.5224	5.7073	5.9824	N
16-Aug-2019 07:08:55	11.0071	7.6040	8.1595	3.8565	4.1386	N
23-Jan-2020 06:35:50	35.7042	29.8916	29.4446	9.4405	9.9611	N
24-Jan-2020 18:18:05	36.7103	25.0776	23.9756	11.2522	11.9117	N
26-Jan-2020 07:00:42	11.0064	7.5942	8.1698	3.8408	4.1381	N
26-Jan-2020 18:01:05	36.7169	19.2974	17.6297	5.9307	6.0038	N
28-Jan-2020 06:44:06	11.0097	9.5537	9.6883	4.2754	4.5459	N
28-Jan-2020 17:44:41	24.6872	14.5856	12.2159	5.6167	5.5280	N
29-Jan-2020 18:25:55	12.0336	9.3803	9.5636	4.5417	4.8084	Y
30-Jan-2020 06:27:56	24.6740	38.0289	39.1784	13.0154	13.8724	N
17-May-2020 06:27:56	24.6831	40.3020	40.3478	14.0102	14.9282	N
18-May-2020 07:08:55	11.0158	7.5984	8.0340	3.8559	4.1430	N
18-May-2020 18:09:52	36.7075	24.6588	22.5834	7.2358	7.4970	N
20-May-2020 06:52:19	11.0153	9.9578	9.8275	4.6735	4.8757	N
20-May-2020 17:53:14	36.7081	37.5865	36.9348	10.7140	11.2305	Y
22-May-2020 06:35:51	11.0192	7.5999	8.1559	3.8375	4.1393	N
22-May-2020 17:37:00	24.6847	9.9267	11.0220	5.2704	5.4248	N
23-May-2020 18:18:05	12.0236	9.2047	8.8111	3.9714	4.2262	N
24-May-2020 06:19:30	24.6867	24.8169	23.3316	7.3180	7.6953	N
25-May-2020 07:00:42	11.0070	9.6716	8.8510	4.1241	4.2995	N
19-Aug-2020 17:45:08	24.6856	9.4382	9.5279	4.1553	4.4203	Y
20-Aug-2020 18:26:16	12.0281	11.3312	11.2978	4.8570	5.1251	N
21-Aug-2020 06:27:57	24.6828	18.7409	16.4489	6.4415	6.7787	N
22-Aug-2020 07:08:55	11.0158	12.0683	11.9908	5.6986	6.0383	N
22-Aug-2020 18:09:52	36.7131	21.3634	19.0116	6.3202	6.6222	N
24-Aug-2020 06:52:39	11.0128	8.7869	8.5437	3.9126	4.1564	N
24-Aug-2020 17:53:25	36.7067	15.7319	15.5078	6.7336	7.0265	N
26-Aug-2020 06:35:49	11.0222	10.6982	11.4110	5.6474	6.0141	N
26-Aug-2020 17:37:09	24.6700	18.5093	19.7147	5.7064	6.0731	Y

Table 4.9 Sentinel-1A results summary.

Maximum maximum position error [m]	Maximum maximum velocity error [mm/s]	Maximum mean position error [m]	Maximum mean velocity error [mm/s]	Mean maximum position error [m]	Mean maximum velocity error [mm/s]	Mean mean position error [m]	Mean mean velocity error [mm/s]
41.9285	40.9626	15.1721	16.0343	16.5124	16.1012	6.1990	6.5216

Sentinel-1B

Table 4.10 Sentinel-1B results.

Start	Duration [h]	Maximum position error [m]	Maximum velocity error [mm/s]	Mean position error [m]	Mean velocity error [mm/s]	Manoeuvre
05-Aug-2019 07:00:15	11.0047	10.1840	9.4293	4.1305	4.2973	N
05-Aug-2019 18:00:32	36.7164	42.9887	42.6395	16.1093	17.2265	N
07-Aug-2019 06:43:31	11.0161	9.0445	9.4725	4.2395	4.5313	N
07-Aug-2019 17:44:29	24.6781	13.2200	13.0489	4.6769	4.9434	Y
08-Aug-2019 18:25:10	36.7200	44.0731	44.2221	8.9966	9.6172	N
10-Aug-2019 07:08:2'	11.0069	9.1113	8.9222	3.8514	4.1507	N
10-Aug-2019 18:08:47	36.7147	14.3125	13.3465	6.2360	6.4523	N
12-Aug-2019 06:51:40	11.0111	7.6323	8.2051	3.8582	4.1403	N
12-Aug-2019 17:52:20	36.7117	37.6041	36.7069	10.2387	10.7246	N
14-Aug-2019 06:35:02	11.0158	8.1922	8.1652	3.9391	4.2124	N
14-Aug-2019 17:35:59	24.6841	15.3105	15.9260	5.6542	6.0128	Y
15-Aug-2019 18:17:00	12.0325	10.3521	10.1465	4.0018	4.2438	N
16-Aug-2019 06:18:57	24.6700	14.5790	15.0189	7.0004	7.4034	N
10-Sep-2019 18:00:32	36.7169	13.7950	12.8418	5.7607	6.0778	N
12-Sep-2019 06:43:33	11.0097	8.6515	9.1754	4.0930	4.3762	N
12-Sep-2019 17:44:08	36.7100	21.2721	21.4754	6.5348	6.8393	N
14-Sep-2019 06:26:44	24.6939	12.8443	11.7692	4.8695	5.0869	N
15-Sep-2019 07:08:22	11.0069	9.7109	10.0479	3.9913	4.2689	N
15-Sep-2019 18:08:47	36.7147	13.5810	12.2790	4.8377	5.1043	N
17-Sep-2019 06:51:40	11.0111	8.1534	8.5719	3.8975	4.1819	N
17-Sep-2019 17:52:20	36.7144	18.5693	19.1026	5.6130	6.0186	Y
19-Sep-2019 06:35:12	11.0208	9.4765	10.1969	4.0082	4.3244	N
19-Sep-2019 17:36:27	24.6758	11.8907	11.2651	4.8294	5.1136	N
20-Sep-2019 18:17:00	12.0325	10.3543	10.7249	4.3060	4.5779	N
21-Sep-2019 06:18:57	24.6790	13.8897	13.9539	4.3399	4.5909	N
12-May-2020 18:08:47	36.7147	31.0206	29.9118	7.8186	8.2381	N
14-May-2020 06:51:40	11.0111	8.2816	8.2111	3.9468	4.2050	N
14-May-2020 17:52:20	36.7144	38.7888	38.3806	9.3499	9.8625	N
16-May-2020 06:35:12	11.0117	7.6060	8.1768	3.8514	4.1419	N
16-May-2020 17:35:54	24.6850	15.5359	13.1421	5.4520	5.6014	N
17-May-2020 18:17:00	12.0325	10.8830	11.0909	4.5875	4.8742	N
18-May-2020 06:18:57	24.6883	18.7758	17.8141	4.7646	5.0156	N
19-May-2020 07:00:15	11.0047	15.1475	14.7589	7.0955	7.6036	N
19-May-2020 18:00:32	36.7169	27.5155	26.3823	8.6692	9.1498	Y
21-May-2020 06:43:33	11.0097	14.7326	15.1522	5.1562	5.5327	N
21-May-2020 17:44:08	36.7192	34.8421	34.3436	8.9019	9.2729	N
23-May-2020 06:27:17	24.6756	28.7193	27.8280	8.7430	9.1746	N
24-May-2020 07:07:49	11.0161	8.5250	8.2107	3.9411	4.1681	N
24-May-2020 18:08:47	36.7136	44.5920	43.7662	12.2840	12.8908	N
26-May-2020 06:51:36	11.0142	10.0263	9.9656	4.5641	4.7606	N
26-May-2020 17:52:27	36.7161	38.0818	36.9285	9.4370	9.9087	N
28-May-2020 06:35:25	11.005	9.0498	9.2842	3.7419	3.9987	N
09-Jun-2020 17:36:27	24.6794	40.2233	39.7264	14.6238	15.5099	N
10-Jun-2020 18:17:13	12.0289	7.6020	8.2120	3.8651	4.1532	N
11-Jun-2020 06:18:57	24.6881	16.9582	15.7914	5.1911	5.4054	N
12-Jun-2020 07:00:14	11.0050	8.6523	8.1681	3.9951	4.2201	N
12-Jun-2020 18:00:32	36.7169	44.9292	45.0957	13.5317	14.5004	N
14-Jun-2020 06:43:33	11.0097	8.8412	9.0475	3.9801	4.2379	N

Start	Duration [h]	Maximum position error [m]	Maximum velocity error [mm/s]	Mean position error [m]	Mean velocity error [mm/s]	Manoeuvre
14-Jun-2020 17:44:08	24.6839	38.3744	0.0388	15.2865	0.0164	N
15-Jun-2020 18:25:10	12.0261	10.4312	0.0100	4.1572	0.0043	N
16-Jun-2020 06:26:44	24.6922	37.5319	37.9095	14.8236	15.8636	N
17-Jun-2020 07:08:16	11.0158	7.5999	8.1756	3.7779	4.0575	N
17-Jun-2020 18:09:13	36.7075	30.2171	29.4636	10.7603	11.3795	Y
19-Jun-2020 06:51:40	11.0111	7.6308	8.1972	3.8587	4.1347	N
19-Jun-2020 17:52:20	36.7144	32.7714	31.8010	7.1335	7.3856	N
21-Jun-2020 06:35:12	11.0208	8.0023	8.2092	3.8442	4.1326	N
21-Jun-2020 17:36:27	24.6758	12.7608	12.1071	5.6525	5.6248	N
22-Jun-2020 18:17:00	12.0294	7.7358	8.2103	3.8873	4.1650	N
23-Jun-2020 06:18:46	24.6897	36.0877	35.0053	10.5292	11.1045	N
24-Jun-2020 07:00:09	11.0060	7.6130	8.1518	3.8068	4.0901	N

Table 4.11 Sentinel-1B results summary.

Maximum maximum position error [m]	Maximum maximum velocity error [mm/s]	Maximum mean position error [m]	Maximum mean velocity error [mm/s]	Mean maximum position error [m]	Mean maximum velocity error [mm/s]	Mean mean position error [m]	Mean mean velocity error [mm/s]
44.9292	45.0957	16.1093	17.2265	18.5813	17.5554	6.4170	6.4484

The results obtained for the Sentinel-1 class show that the propagator performs well, having less than 45 metres of maximum position error in time lapses of 36 hours. Furthermore, the mean mean position error is less than 6.5 metres, which means that most of the time the propagator allows us to know the position of the satellite with an accuracy of 6.5 metres.

4.3.2 Sentinel-2

As we did for the Sentinel-1 class, the parameters of this satellite group are provided. The parameters obtained with the process analysed in Section 4.2.1 that describe these satellites are $m = 1148 \text{ kg}$ (obtained from the ESA datasheet, $S^* = 4.02 \text{ m}^2$, $S_{SRP}^* = 10.29 \text{ m}^2$ and $C_D^* = 0.74$).

The results obtained for Sentinel-2A and Sentinel-2B are the following.

Sentinel-2A

Table 4.12 Sentinel-2A results.

Start	Duration [h]	Maximum position error [m]	Maximum velocity error [mm/s]	Mean position error [m]	Mean velocity error [mm/s]	Manoeuvre
06-Feb-2020 11:21:51	11.2244	9.3952	9.6343	3.9174	4.1231	N
06-Feb-2020 22:35:19	23.4881	16.9754	17.6300	5.7098	5.9926	N
07-Feb-2020 22:04:36	60.9497	52.9363	56.0824	21.0365	22.2666	N
10-Feb-2020 11:01:35	11.2236	7.5507	7.9735	3.7919	4.0058	N
10-Feb-2020 22:15:00	37.4425	39.7013	41.9450	14.1348	14.8563	N
12-Feb-2020 11:41:33	23.4997	8.9898	8.2175	3.9376	4.0890	N
13-Feb-2020 11:11:32	11.2140	7.5577	7.9375	3.7860	3.9974	N
03-Sep-2020 11:21:54	11.2239	8.2158	8.3824	3.8256	4.0288	N
03-Sep-2020 22:35:20	12.2661	7.5497	7.9966	3.8055	4.0267	N
04-Sep-2020 10:51:18	48.6706	36.4581	37.5711	16.4665	17.2878	N
06-Sep-2020 11:31:32	23.5000	13.9493	14.2102	5.2463	5.4935	N
07-Sep-2020 11:01:32	48.6753	9.2992	9.1002	3.8823	4.0983	N
09-Sep-2020 11:42:03	34.7150	13.8962	12.2077	4.5961	4.7096	Y

Table 4.13 Sentinel-2A results summary.

Maximum maximum position error [m]	Maximum maximum velocity error [mm/s]	Maximum mean position error [m]	Maximum mean velocity error [mm/s]	Mean maximum position error [m]	Mean maximum velocity error [mm/s]	Mean mean position error [m]	Mean mean velocity error [mm/s]
52.9363	56.0824	21.0365	22.2666	19.1265	19.7089	7.9387	8.3485

Sentinel-2B**Table 4.14** Sentinel-2B results.

Start	Duration [h]	Maximum position error [m]	Maximum velocity error [mm/s]	Mean position error [m]	Mean velocity error [mm/s]	Manoeuvre
11-Sep-2019 11:11:29	11.2240	7.5509	7.9917	3.7913	4.0149	N
18-Sep-2019 11:01:24	48.6775	22.8871	23.2213	9.4275	9.8655	Y
20-Sep-2019 11:42:03	23.4906	9.4372	9.4395	4.1917	4.3673	N
21-Sep-2019 11:11:29	11.2245	7.9509	8.3704	3.7658	3.9669	N
08-Sep-2020 11:21:54	11.2239	7.5634	7.9694	3.7889	4.0022	N
08-Sep-2020 22:35:20	60.9356	13.8118	12.9298	4.4651	4.6412	N
11-Sep-2020 11:31:28	23.5014	9.2452	9.1939	4.0938	4.2994	N
12-Sep-2020 11:01:33	11.2239	7.5503	7.9625	3.9477	4.1684	N
12-Sep-2020 22:14:59	60.9417	15.3078	14.8242	6.2735	6.5397	N
15-Sep-2020 11:11:29	11.2333	7.9925	3.7579	3.7579	3.9673	N
15-Sep-2020 22:25:29	60.9400	54.3628	57.0431	16.2913	17.1195	Y
18-Sep-2020 11:21:53	11.2242	11.8230	12.2680	4.4097	4.6385	N
18-Sep-2020 22:35:20	11.2250	7.5525	7.9725	3.7950	4.0100	N
22-Sep-2020 22:15:32	37.4347	36.2555	36.9748	9.4037	9.9594	N
24-Sep-2020 11:41:37	34.7250	36.6082	37.3566	10.1613	10.7438	N

Table 4.15 Sentinel-2B results summary.

Maximum maximum position error [m]	Maximum maximum velocity error [mm/s]	Maximum mean position error [m]	Maximum mean velocity error [mm/s]	Mean maximum position error [m]	Mean maximum velocity error [mm/s]	Mean mean position error [m]	Mean mean velocity error [mm/s]
54.3628	57.0431	16.2913	17.1195	17.0599	17.1517	6.1043	6.4203

The results obtained for the Sentinel-2 class show that the propagator predict the orbit with less than 55 metres of maximum position error in time lapses of 61 hours. The mean maximum position error is less than 20 metres and the mean mean position error is less than 8 metres (slightly greater than for the Sentinel-1 class due to the length of the propagations). These results, along with the results obtained for Sentinel-1, assure the good behaviour of the propagator designed.

4.3.3 Results discussion

The OEMs have errors of a few meters, and they have to be interpolated with some loss of precision. This, along with the fact that the propagator designed is capable of measuring the position of any of the satellites studied with a maximum error of 54.5 metres and a mean error less than 8 metres in time lapses of 61 hours, allows us to affirm that the propagator designed perfectly captures the perturbations to which the satellites under study are subjected. Furthermore, the fact that the mean maximum position error committed during these analysis is less than 19.2 metres speaks of

the precision of this propagator, having in most cases the certainty of not being wrong by more than 20 metres.

In the case of the velocity error, we have roughly the same results as for the position error. The propagator never exceeds the error of 6 *cm/s* and we have a mean error of less than 8.5 *mm/s* in time lapses of 61 hours.

It should be noted that in the sections where manoeuvres are performed, these have been eliminated as no data on them are available. Therefore, the sections with manoeuvre indicator Y have been analysed by propagating from the beginning to the start of the manoeuvre and propagating after the end of the manoeuvre to the end of the section, which leaves two separate propagation sections.

5 Conclusions and future work

5.1 Conclusions

Throughout this project we have reviewed the importance of considering perturbations when trying to recreate the orbit of orbiting objects. These perturbations, which deviate satellites from their original orbits, are not trivial to study and require in most cases the use of numerical methods to obtain accurate results. The combination of the most accurate models for the different types of perturbations does not always result in the most accurate propagator, as discussed above.

This worsening of the propagator depending on the models we use is due to the non-linearity of the models used and the fact that in the world we live in, sometimes, 1+1 does not result in 2. In an ideal world, taking more and more precision would result in the best propagator. But unfortunately, models sometimes interfere with each other and lead to inaccuracies that we must avoid.

One thing to take away from this project is that we should always analyse how to combine the different models available to decide which set of perturbation models to use. Choosing the most accurate models and combining them without prior analysis can lead to inaccuracies, such as when increasing the degree and order of Earth harmonics or when combining the NRLMSISE-00 atmospheric model with tides.

To minimise the error made in assuming isotropic drag and isotropic solar pressure radiation due to the lack of information related to the orientation of the satellites, we obtained the geometric characteristics that best fit the satellite data provided. However, this minimisation process can never be better (in theory) than having the actual satellite attitude data.

It is very remarkable that the designed propagator is able to predict in most cases the orbit of the studied satellite with the same order of accuracy as the built-in error of the OEMs. This may lead us to think that the propagator is not able to obtain a higher accuracy in the prediction of the orbits of the satellites studied because it is limited by the error of the OEMs themselves. If this is the case, it is virtually impossible for the propagator to obtain better results, so it is necessary to increase the accuracy in the measurements of the real data.

5.2 Future work

As we have made clear on numerous occasions throughout the development of this project, we lack information on the attitude of the satellites. This fact, which detracts from the accuracy of the modelling of atmospheric drag and solar-radiation pressure, together with the possible limiting factor due to the error in the OEMs discussed above, leads us to recommend improvements focused on these two aspects to try to further improve the accuracy of the propagator.

To determine the attitude of the satellites is truly complex [16], but there are several methods that allow to control the attitude of these objects [27]. Controlling the satellite's attitude is, in

fact, knowing the orientation the satellite has at any desired time. This information could make a difference in determining the future position of the satellites under study, so it is worth checking its influence.

On the other hand, it goes without saying that the more accurate the measurements we make of the position and velocity of satellites, the less initial error the propagators we use will have. A measurement error of a few metres is a very high accuracy considering the dimensions of the Earth, but as technology advances and we have access to smaller measurement errors, our propagators will become more and more accurate.

List of Figures

1.1	Geocentric satellites	2
1.2	Sentinel-1 [12]	3
1.3	Sentinel-2 [13]	4
2.1	Gravitational force between two isolated masses	8
2.2	Mass-centre reference frame	9
2.3	Keplerian orbital elements	10
2.4	Zonal Harmonics. The shading indicates regions of additional mass and the numbers link regions between the views [22]	13
2.5	Sectorial Harmonics. They take into account the extra mass distribution in longitudinal regions [22]	13
2.6	Tesseral Harmonics, which are dependent on latitude and longitude [22]	13
2.7	Object orbiting Earth affected by the Moon [25]	16
2.8	Precession and nutation of Earth's axis [22]	19
3.1	Frame transformation tree	23
3.2	CIO-based transformations	24
3.3	Equinox-based transformations	24
3.4	Topocentric frame	25
3.5	Object view of topocentric frame	26
3.6	Variation of the semi-major axis of a GEO due to Luni-Solar perturbation	31
3.7	Variation of the eccentricity of a GEO due to Luni-Solar perturbation	32
3.8	Variation of the inclination angle of a GEO due to Luni-Solar perturbation	32
3.9	Shorter analysis of the variation of the semi-major axis of a GEO due to Luni-Solar perturbation	33
3.10	Shorter analysis of the variation of the eccentricity of a GEO due to Luni-Solar perturbation	33
3.11	Shorter analysis of the variation of the inclination angle of a GEO due to Luni-Solar perturbation	34
3.12	Variation of the semi-major axis of a LEO due to Luni-Solar perturbation	34
3.13	Variation of the eccentricity of a LEO due to Luni-Solar perturbation	35
3.14	Variation of the inclination of a LEO due to Luni-Solar perturbation	35
3.15	Variation of the argument of the perigee of a LEO due to Luni-Solar perturbation	36
3.16	Variation of the RAAN of a LEO due to Luni-Solar perturbation	36
3.17	Variation of the semi-major axis of a LEO due to Luni-Solar perturbation for different inclinations	37
3.18	Variation of the eccentricity of a LEO due to Luni-Solar perturbation for different inclinations	37
3.19	Variation of the argument of the perigee of a LEO due to Luni-Solar perturbation for different inclinations	38
3.20	Variation of the RAAN of a LEO due to Luni-Solar perturbation for different inclinations	38

3.21	Variation of the semi-major axis of a GEO due to J_2 perturbation	39
3.22	Variation of the eccentricity of a GEO due to J_2 perturbation	39
3.23	Variation of the inclination of a GEO due to J_2 perturbation	40
3.24	Shorter analysis of the variation of the semi-major axis of a GEO due to J_2 perturbation	40
3.25	Shorter analysis of the variation of the eccentricity of a GEO due to J_2 perturbation	41
3.26	Shorter analysis of the variation of the inclination angle of a GEO due to J_2 perturbation	41
3.27	Variation of the semi-major axis of a LEO due to J_2 perturbation	42
3.28	Variation of the eccentricity of a LEO due to J_2 perturbation	42
3.29	Variation of the inclination of a LEO due to J_2 perturbation	43
3.30	Variation of the argument of the perigee of a LEO due to J_2 perturbation	43
3.31	Variation of the RAAN of a LEO due to J_2 perturbation	44
3.32	Long periodic/short periodic beat period from zonal harmonics [22]	44
3.33	Variation of the semi-major axis of a LEO due to J_2 perturbation for different inclinations	45
3.34	Variation of the argument of the perigee of a LEO due to J_2 perturbation for different inclinations	45
3.35	Variation of the RAAN of a LEO due to J_2 perturbation for different inclinations	46
3.36	Variation of the semi-major axis of a LEO due to atmospheric drag	46
3.37	Variation of the eccentricity of a LEO due to atmospheric drag	47
3.38	Variation of the inclination of a LEO due to atmospheric drag	47
3.39	Variation of the argument of the perigee of a LEO due to atmospheric drag	48
3.40	Variation of the RAAN of a LEO due to atmospheric drag	48
3.41	Influence of altitude in the variation of the semi-major axis of a LEO due to atmospheric drag	49
3.42	Influence of altitude in the variation of the eccentricity of a LEO due to atmospheric drag	49
3.43	Influence of altitude in the variation of the inclination of a LEO due to atmospheric drag	50
3.44	Influence of altitude in the variation of the argument of the perigee of a LEO due to atmospheric drag	50
3.45	Influence of altitude in the variation of the RAAN of a LEO due to atmospheric drag	51
3.46	Variation of the semi-major axis of a GEO due to solar radiation pressure	51
3.47	Variation of the eccentricity of a GEO due to solar radiation pressure	52
3.48	Variation of the inclination of a GEO due to solar radiation pressure	52
3.49	Variation of the semi-major axis of a LEO due to solar radiation pressure	53
3.50	Variation of the eccentricity of a LEO due to solar radiation pressure	53
3.51	Variation of the inclination of a LEO due to solar radiation pressure	54
3.52	Variation of the argument of the perigee of a LEO due to solar radiation pressure	54
3.53	Variation of the RAAN of a LEO due to solar radiation pressure	55
4.1	Version 1 OEM without acceleration nor covariance	60
4.2	Version 2 OEM with optional accelerations	61
4.3	Version 2 OEM with optional covariance matrix	61
4.4	Process of optimisation	63
4.5	Position error variation with different Earth harmonic models in a 24-hour window	64
4.6	Velocity error variation with different Earth harmonic models in a 24-hour window	64
4.7	Position error variation with different third body perturbation models	65
4.8	Velocity error variation with different third body perturbation models	66
4.9	Position error variation with different atmospheric models in a 24-hour window	67
4.10	Velocity error variation with different atmospheric models in a 24-hour window	67
4.11	Position error variation with tides models in a 24-hour window using Harris-Priester	68
4.12	Velocity error variation with tides models in a 24-hour window using Harris-Priester	69
4.13	Position error variation with tides models in a 24-hour window using NRLMSISE-00	69
4.14	Velocity error variation with tides models in a 24-hour window using NRLMSISE-00	70
4.15	Comparison between the two models proposed	70

List of Tables

2.1	Forms of perturbations wielded on each orbital element. P stands for periodic and S for secular [25]	11
2.2	Comparison between the forces exerted by the Moon and the main solar system objects and the force Earth produces on LEO and GEO satellites	17
4.1	OEM Layout	58
4.2	OEM Header	58
4.3	OEM Metadata	59
4.4	Comparison between different harmonic models in a 24-hour window	65
4.5	Comparison between different third-body models in a 24-hour window	66
4.6	Comparison between different atmospheric models in a 24-hour window	68
4.7	Comparison between different tides models in a 24-hour window	69
4.8	Sentinel-1A results	72
4.9	Sentinel-1A results summary	72
4.10	Sentinel-1B results	73
4.11	Sentinel-1B results summary	74
4.12	Sentinel-2A results	74
4.13	Sentinel-2A results summary	75
4.14	Sentinel-2B results	75
4.15	Sentinel-2B results summary	75

Bibliography

- [1] European Space Agency, *Sentinel-1a data sheet*: https://esamultimedia.esa.int/docs/SI-Data_Sheet.pdf.
- [2] James M Bardeen and Jacobus A Petterson, *The lense-thirring effect and accretion disks around kerr black holes*, The Astrophysical Journal **195** (1975), L65.
- [3] Blue Book, *Time code formats*, (2002).
- [4] PINK BOOK, *Orbit data messages*, (2003).
- [5] Riccardo Borghi, *On newton's shell theorem*, European Journal of Physics **35** (2014), no. 2, 028003.
- [6] Bruce Bowman, W Kent Tobiska, Frank Marcos, Cheryl Huang, Chin Lin, and William Burke, *A new empirical thermospheric density model jb2008 using new solar and geomagnetic indices*, AIAA/AAS astrodynamics specialist conference and exhibit, 2008, p. 6438.
- [7] P Cefola, JF San-Juan, S Setty, R Proulx, et al., *Review of the draper semi-analytical satellite theory (dsst)*, Proc. 18th Australian Int. Aerosp. Congr.: HUMS-11th Defence Sci. Technol. Int. Conf. Health Usage Monit.: ISSFD-27th Int. Symp. Space Flight Dyn., 2019.
- [8] Celestrak, *Norad two-line element set format*: <https://www.celestrak.com/NORAD/documentation/tle-fmt.php>.
- [9] Vladimir A Chobotov, *Orbital mechanics*, Aiaa, 2002.
- [10] DH Dickson and IW Kelly, *The 'barnum effect' in personality assessment: A review of the literature*, Psychological Reports **57** (1985), no. 2, 367–382.
- [11] MC Eckstein and F Hechler, *A reliable derivation of the perturbations due to any zonal and tesseral harmonics of the geopotential for nearly-circular satellite orbits (computation of nearly circular satellite orbit perturbation due to geopotential harmonics)*, (1970).
- [12] ESA, *Sentinel-1*: <https://sentinel.esa.int/web/sentinel/missions/sentinel-1>.
- [13] European Space Agency ESA, *Sentinel-2*: <https://sentinel.esa.int/web/sentinel/missions/sentinel-1>.
- [14] CS Group, *Orekit*: <https://www.orekit.org/>.
- [15] Felix R Hoots and Ronald L Roehrich, *Models for propagation of norad element sets*, Tech. report, Aerospace Defense Command Peterson AFB CO Office of Astrodynamics, 1980.

- [16] VJ Modi, *Attitude dynamics of satellites with flexible appendages-a brief review*, Journal of Spacecraft and Rockets **11** (1974), no. 11, 743–751.
- [17] Oliver Montenbruck, Eberhard Gill, and Fh Lutze, *Satellite orbits: models, methods, and applications*, Appl. Mech. Rev. **55** (2002), no. 2, B27–B28.
- [18] Jose M Montilla, Julio C Sanchez, Rafael Vazquez, Jorge Galan-Vioque, Javier Rey Benayas, and Jan Siminski, *Manoeuvre detection in low earth orbit with radar data*, arXiv preprint arXiv:2203.03590 (2022).
- [19] NASA, *Spacewarn bulletin*: <https://nssdc.gsfc.nasa.gov/spacewarn/>.
- [20] Gérard Petit and Brian Luzum, *Iers conventions (2010)*, Tech. report, Bureau International des Poids et mesures sevres (france), 2010.
- [21] JM Picone, AE Hedin, D Pj Drob, and AC Aikin, *Nrlmsise-00 empirical model of the atmosphere: Statistical comparisons and scientific issues*, Journal of Geophysical Research: Space Physics **107** (2002), no. A12, SIA–15.
- [22] David A Vallado, *Fundamentals of astrodynamics and applications*, vol. 12, Springer Science & Business Media, 2001.
- [23] David A Vallado and Paul J Cefola, *Two-line element sets-practice and use*, 63rd International Astronautical Congress, Naples, Italy, 2012, pp. 1–14.
- [24] Rafael Vazquez, *Mecánica orbital y vehículos espaciales tema 1*.
- [25] Rafael Vázquez, *Mecánica orbital y vehículos espaciales tema 4*.
- [26] GA Watson, *Computing helmert transformations*, Journal of computational and applied mathematics 197 (2006), no. 2, 387–394.
- [27] Bing Xiao, Mingyi Huo, Xuebo Yang, and Youmin Zhang, *Fault-tolerant attitude stabilization for satellites without rate sensor*, IEEE Transactions on Industrial Electronics **62** (2015), no. 11, 7191–7202.